

DEFORMATION MECHANISMS IN ADVANCED STRUCTURAL CERAMICS DUE TO
INDENTATION AND SCRATCH PROCESSES

By

DIPANKAR GHOSH

A DISSERTATION PRESENTED TO THE GRADUATE SCHOOL
OF THE UNIVERSITY OF FLORIDA IN PARTIAL FULFILLMENT
OF THE REQUIREMENTS FOR THE DEGREE OF
DOCTOR OF PHILOSOPHY

UNIVERSITY OF FLORIDA

2009

© 2009 Dipankar Ghosh

DEDICATION

I dedicate my dissertation to my loving parents and other family members whose constant guidance, encouragement and inspiration, unselfish help and immeasurable sacrifices have contributed tremendously to build my academic carrier and reach a stage where I am standing today. I find myself wordless to express my deepest gratitude for my parents who taught me the importance of higher education and hard work. I will always appreciate and remember their timely guidance in every way throughout the life to accomplish my academic achievements. They not only supported any decision I took but also always have been a part of that. There won't be any further appropriate time to mention my loving wife who has been with me during this wonderful journey of doctoral work and has always forwarded her helping hands. Also, I dedicate this dissertation to all others whose kind blessings and unconditional love have been with me always.

ACKNOWLEDGMENTS

I am indebted to many people who have contributed through their support, inspiration, knowledge, encouragement and friendship throughout my PhD to bring this dissertation in a completion. Needlessly, I would like to first thank my PhD advisor Prof. Ghatu Subhash who not only gave me an opportunity to come to United States to pursue higher education but also provided continuous support during the past five years. It is really hard for me to overstate my gratitude to Prof. Subhash without whose inspirational and expert guidance, constant encouragements and endless unselfish help, I never could have finished my doctoral research. He is one of those few professors I met who not only motivate graduate students for performing excellent research but also guide them in the right direction. Prof. Subhash has always been supportive and gave me complete freedom to pursue my research in several directions. His experimental expertise and sound theoretical knowledge of research, and dedication for work are always inspirational for graduate students. I will always be grateful for his insightful discussions and suggestions which not only enriched my breadth of knowledge but also be helpful in pursuing my future endeavors. During the past five years, he has been truly an advisor as well as a good friend to me.

I truly acknowledge Dr. Tirumalai S. Sudarshan and Dr. Ramachandran Radhakrishnan, Materials Modification Inc. (MMI), Fairfax, VA, for providing me the opportunity to work with the sintering system, plasma pressure compaction, at MMI in Summer 2005 to produce the advanced structural ceramics and composites which have been investigated in this dissertation. I truly enjoyed the period I stayed at MMI and working with Dr. Sudarshan and Dr. Radhakrishnan enriched my knowledge on advanced ceramic processing.

I acknowledge the help of Prof. Yoke Khin Yap, Department of Physics, Michigan Technological University, MI, for the research work on spectroscopic investigation of phase transformation in boron carbide ceramics. He not only gave me the opportunity to work in his group and laboratory but also provided useful guidance to complete the work. I would also like to thank Mr. Chee Huei Lee, graduate student of Prof. Yap, for his assistance in performing the spectroscopic studies. I would also like give my sincere thanks to Mrs. Ruth I. Kramer, Mr. Stephen F. Forsell, Mr. Edward A. Laitila and Mr. Owen P. Mills (technical staff members in Materials Science and Engineering Department at Michigan Technological University, MI) for their enormous help in learning several characterization equipments. I am truly thankful to Prof. Nina Orlovskaya, Department of Mechanical, Materials and Aerospace Engineering, University of Central Florida, FL, for giving me the access to use Raman spectrometer in her laboratory. I am also grateful for her guidance and fruitful discussions in completing the research on residual stress measurement as well as for the help in preparing a manuscript.

I sincerely acknowledge Dr. Gerald Bourne, one of my PhD committee members, for his valuable assistance, guidance and time in performing the transmission electron microscopic investigation in ZrB_2 ceramics without which this dissertation would not have been completed. He was also helpful in preparing multiple manuscripts during the research. I also take this opportunity to thank my other PhD committee members Professors Gregory Sawyer, Nagaraj Arakere and Fereshteh Ebrahimi for their helpful advice and suggestions in general.

I would like to acknowledge my fellow graduate students and friends Timothy Walter, Mickel Klecka, Shiladitya Pal, Jiwoon Kwon and several others for their time, suggestions and fruitful discussions. Finally, I sincerely thank my parents and other family members for their love, support and encouragements. I am also grateful to my wife Piyasa who always has been helpful to me.

This work was supported by U.S. National Science Foundation under grant no. CMS-0324461 with Ken Chong as the program manager. The use of equipment facilities at Major Analytical Instrumentation Center, University of Florida, is also gratefully acknowledged.

TABLE OF CONTENTS

	<u>page</u>
ACKNOWLEDGMENTS.....	4
LIST OF TABLES.....	9
LIST OF FIGURES.....	10
ABSTRACT	14
CHAPTER	
1 ADVANCED STRUCTURAL CERAMICS AND COMPSOITES.....	16
1.1 Introduction	16
1.2 Materials	17
1.2.1 Boron Carbide (B_4C).....	17
1.2.2 Zirconium diboride – silicon carbide composite (ZrB_2-SiC)	18
2 PROCESSING OF ADVANCED CERAMICS	21
2. 1 Introduction	21
2.2 Literature on Processing of B_4C Ceramics.....	21
2.3 Literature on Processing of ZrB_2-SiC Composite.....	22
2.4 Plasma Pressure Compaction Technique.....	24
2.4.1 Processing of Fine-Grained B_4C Ceramics	26
2.4.2 Processing of $ZrB_2-5wt\%SiC$ Composite.....	27
2.5 Conclusions	29
3 DYNAMIC INDENTATION RESPONSE OF B_4C CERAMICS	38
3.1 Introduction	38
3.2 Static and Dynamic Indentations	38
3.2.1 Static Indentation Fracture	38
3.2.2 Dynamic Indentation Fracture	40
3.2.3 Dynamic Indentation Tester.....	42
3.2.4 Experimental	42
3.2.5 Results of Indentation Experiments and Discussion.....	43
3.3 Spectroscopic Investigation of Localized Phase Transformation.....	47
3.3.1 Localized Phase Transformation	47
3.3.2 Fundamentals of Spectroscopic Techniques.....	49
3.3.2.1 Molecular vibration	49
3.3.2.2 Raman and infrared spectroscopy	50
3.3.2.3 Photoluminescence.....	52
3.3.3 Experimental	54
3.3.4 Results of Raman Spectroscopy	54

3.3.5 Results of Photoluminescence Spectroscopy.....	57
3.3.6 Results of Infrared Spectroscopy	58
3.4 Conclusions	60
4 SCRATCH-INDUCED DEFORMATION IN ZrB ₂ -SiC COMPOSITE.....	78
4.1 Introduction	78
4.2 Scratch Studies.....	80
4.2.1 Experimental	80
4.2.1.1 Constant low-load and low-velocity scratches.....	80
4.2.1.2 Variable high-load and high-velocity scratches	81
4.2.2 Results	81
4.2.2.1 Microstructural features of constant load low-velocity scratches....	81
4.2.2.2 Microstructural features of variable load high-velocity scratches ...	84
4.2.3 Influence of Elastic Stress Field on the Scratch-induced Deformation ...	87
4.2.4 Discussion	92
4.3 Residual Stress Measurement within SiC Grains in ZrB ₂ -SiC Composite.....	97
4.3.1 Micro-Raman Spectroscopy	97
4.3.2 Experimental	99
4.3.3 Results of Micro-Raman Spectroscopy	100
4.3.4 Evolution of Residual Stress Field.....	103
4.3.4.1 Residual stress in SiC grains of as-processed composite.....	103
4.3.4.2 Residual stress in SiC grains located within the scratch grooves	104
4.3.5 Relationship between Mechanical Residual Stress and Raman Spectroscopy	106
4.3.6 Determination of Residual Stress	110
4.4 Conclusions	116
5 ROOM-TEMPERATURE DISLOCATION ACTIVITY IN UHTCs.....	141
5.1 Introduction	141
5.2 Experimental.....	142
5.3 Results and Discussion.....	143
5.4 Conclusions	151
6 SUMMARY AND FUTURE WORK	160
6.1 Conclusions	160
6.2 Future Work.....	164
6.2.1 Determination of Transition Point of Phase Transformation in B ₄ C	164
6.2.2 Scratch Response of Oxidized Surfaces of ZrB ₂ -SiC Composite	164
APPENDIX: DYNAMIC INDENTATION RESPONSE OF B ₄ C CERAMICS	168
LIST OF REFERENCES	170
BIOGRAPHICAL SKETCH.....	187

LIST OF TABLES

<u>Table</u>		<u>page</u>
2-1	Processing conditions in P ² C [®] method for sintering of B ₄ C compacts.....	37
3-1	Comparison of average dynamic and static hardness and fracture toughness values	77
4-1	Material properties.....	140

LIST OF FIGURES

<u>Figure</u>	<u>page</u>
2-1 Schematic of a P ² C [®] equipment.	30
2-2 Consolidated boron carbide disk and test samples for indentation.....	31
2-3 SEM micrographs of sintered B ₄ C samples at various processing temperatures and time.....	32
2-4 Optical micrographs of the etched sintered B ₄ C samples sintered at 1750°C for A) 2, B) 5 and C) 30 min. The average grain sizes are indicated on the optical micrographs. Darker regions in the micrographs represent mostly grain pull-outs during polishing.	33
2-5 A ZrB ₂ -5wt%SiC composite sintered using P ² C [®] technique.	34
2-6 A) SEM micrograph of the fragmented surface of ZrB ₂ -SiC composite and B) a higher magnification SEM image revealing absence of any porosity within ZrB ₂ matrix as well as at the ZrB ₂ -SiC interface areas.	35
2-7 XRD pattern collected from the sintered ZrB ₂ -SiC composite.....	36
3-1 Schematic of experimental setup for dynamic indentation hardness measurements.....	61
3-2 Comparison of static and dynamic hardness values for three grain sizes of B ₄ C.	62
3-3 Optical micrographs of A) static and B) dynamic indents for 2.7 μm grain size B ₄ C at 300 gm. Note longer cracks and more severe damage in dynamic indent.....	63
3-4 Comparison of static and dynamic indentation fracture toughness for three different grain sizes of boron carbide.....	64
3-5 Subsurface damaged region beneath A) static indentation and B) dynamic indentation at a load of 19.6 N for 1.6 μm grain size boron carbide.	65
3-6 Different normal of mode of vibrations.....	66
3-7 A simple schematic illustrating Rayleigh, Stokes and anti-Stokes Raman scattering phenomena.	67
3-8 A schematic of the infrared absorption spectroscopy.	68

3-9	Changes in the net dipole moment of a molecule during asymmetric stretching.	69
3-10	A schematic illustration of photoluminescence phenomenon.	70
3-11	A) visible Raman spectra and C) uv Raman spectra from the un-indented surface and damaged regions beneath the static and dynamic indentations. B) Magnified view of two of the spectra in A.	71
3-12	Crystal structure of boron carbide (B_4C).	72
3-13	Origin of D-peak and G-peak.	73
3-14	Photoluminescence from the un-indented surfaces and damaged regions beneath the static and dynamic indentations.	74
3-15	FTIR spectra from the un-indented surfaces and damaged regions beneath the static and dynamic indentations.	75
3-16	Schematic of A) a rhombohedral unit cell of B_4C with eight $B_{11}C$ icosahedrons at the corners. B) Amorphization of each unit cell will form two carbon and one boron atoms and a $B_{11}C$ icosahedron. C) One $B_{11}C$ icosahedron and one boron atom will reorganize into one amorphous boron (α -B) cluster, and a carbon atom that form carbon clusters with adjacent carbon.	76
4-1	A schematic of instrumented high-velocity scratch tester.	118
4-2.	Residual scratch profiles on the polished surface of ZrB_2 -SiC composite at various load levels.	119
4-3	A) Penetration depth profile and B) the corresponding trace of residual scratch groove at 50 mN. Increase in scratch depth corresponds to the damaged regions as indicated by the white dashed circles in Fig. 4-3 B). Magnified SEM micrographs of the damaged regions along the scratch path revealed mostly voids, grain pull out, ZrB_2 grain-boundary fracture and some microcracking.	120
4-4	A) Penetration depth profile and B) the corresponding trace of residual scratch groove at 250 mN. Damaged regions along the scratch path are shown by the white dashed circles.	121
4-5	Scratch depth profiles during the nanoscratch experiments at different loads..	122

4-6	A) Micrograph of scratch induced deformation features at a load of 250 mN. B) A magnified view of the region (X) revealing the slip line patterns and microcracks along the scratch groove as well as cracks emanating from a SiC particle. C) Another region along the scratch path revealing several sets of slip lines oriented randomly with respect to the scratch direction.	123
4-7	Fracture patterns within the scratch groove at a load of 250 mN: A) grain-boundary fracture, microcracking, and scratch debris and B) interfacial cracking between ZrB ₂ and SiC phases as well as microcracks perpendicular to the direction of the scratch path.....	125
4-8	Scratch-induced damage at 250 mN, revealing transgranular microcracking in ZrB ₂ -SiC composite.	126
4-9	A) A high velocity scratch groove, B) high magnification images of extensive transgranular microcracks orthogonal to the scratch direction and C) normal force vs. scratch length profile.....	127
4-10	Slip-line formation within ZrB ₂ phase during high-velocity scratch process.	128
4-11	A) Normalized maximum principal stress distribution, B) schematic of the scratch process, C) normalized maximum shear stress distribution in the vicinity of indenter tip and D) plot of maximum principal stress contours and orientation in the wake of the indenter.....	129
4-12	Variation of A) normalized maximum principal stress ($\bar{\sigma}_1$) at $\bar{y}=0$ and B) normalized maximum shear stress ($\bar{\tau}_{\max}$) at $\bar{y}=0$ and C) $\bar{y}=0.5$ for various values of 'k'. The black triangle indicates the indenter position.	130
4-13	Micrograph of the exit-end region of a scratch at 250 mN revealing numerous slip lines. The white dotted lines indicate the boundary of residual scratch exit-end.....	131
4-14	Raman spectra collected from the ZrB ₂ matrix phase (see the inset also) and the SiC particulate phase present in ZrB ₂ -SiC composite.....	132
4-15	Raman spectra collected from the SiC grains present within and away from the scratch grooves.	133
4-16	A) LO- and TO-Raman peak positions of SiC grains within the scratch grooves at 50, 100, 150 and 250 mN loads. LO- and TO-peak positions at 0 mN correspond to the Raman spectra collected from SiC grains outside the scratch groove. B) Changes in peak positions to stress-free LO- and TO-positions.	134
4-17	Schematic of the scratch process and different crack systems that evolve during the scratch process are shown.....	136

4-18	Distribution of normalized residual stress components; A) σ_x^R , B) σ_y^R and C) σ_z^R on the x-y plane (B/P = 0.005). The black triangle indicates the position of the indenter whereas the black arrow indicates the scratch direction.....	137
4-19	Evolution of residual stress within SiC grains as a function of scratch load.....	138
4-20	SEM micrograph of a scratch groove at 250 mN revealing the uncracked SiC grain surrounded by the heavily microcracked ZrB ₂ matrix.....	139
5-1	Optical micrographs revealing slip-lines formed in the vicinity of indented regions of A) ZrB ₂ and B) HfB ₂ ceramics.	153
5-2	FIB-cut TEM specimen within a constant load (250 mN) scratch groove.	154
5-3	A) A bright field TEM micrograph revealing dense dislocation activity on prismatic planes and B) multiple sets of intersecting slip-lines formed on the surface due to scratch load, resembling patterns observed in A).	155
5-4	A) Bright-field TEM micrograph at $[\bar{1}2\bar{1}0]$ zone axis and B) the corresponding selected area electron diffraction pattern. C) Bright-field TEM image of dislocations in two-beam condition with (0001) g vector.	156
5-5	Electrical conductivity (filled symbols) and electrical resistivity (open symbols) of metals and ceramics.....	158
5-6	Crystal structure of transition metal diborides.....	159
6-1	Cross-sectional areas of the ZrB ₂ -5wt%SiC specimens oxidized for A) 1 B) 5 and C) 15 hours.....	166
6-2	Evolution of structures in a ZrB ₂ -SiC composite during oxidation at 1500°C. ...	167
A-1	Variation of <i>c</i> vs. <i>P</i> in B ₄ C ceramics for dynamic indentations.....	168
A-2	Variation of <i>l</i> vs. <i>P</i> in B ₄ C ceramics for dynamic indentations.....	169

Abstract of Dissertation Presented to the Graduate School
of the University of Florida in Partial Fulfillment of the
Requirements for the Degree of Doctor of Philosophy

DYNAMIC INDENTATION AND SCRATCH RESPONSE OF
ADVANCED STRUCTURAL CERAMICS

By

Dipankar Ghosh

December 2009

Chair: Ghatu Subhash
Major: Mechanical Engineering

Plasma pressure compaction technique was used to develop boron carbide (B_4C) and zirconium diboride-silicon carbide (ZrB_2-SiC) composite. B_4C ceramics are extensively used as body armor in military and civilian applications, and ZrB_2-SiC composite has been recognized as a potential candidate for high-temperature aerospace applications. In this dissertation, processing parameters, quasistatic and high-strain rate mechanical response, and fundamental deformation mechanisms of these materials have been investigated.

In the case of B_4C , the rate sensitivity of indentation hardness was determined using a dynamic indentation hardness tester that can deliver loads in 100 μs . By comparing dynamic hardness with the static hardness, it was found that B_4C exhibits a lower hardness at high-strain rate, contrary to known behavior in many structural ceramics. However, these results are consistent with the ballistic testing of B_4C armors as reported in recent literature. This behavior was further investigated using a series of spectroscopic techniques such as visible and UV micro-Raman, photoluminescence and infrared. These studies not only confirmed that structural transformation occurred during indentation experiments similar to that in ballistic testing of B_4C but also

suggested a greater degree of structural changes under dynamic loading compared to static loading.

Due to the potential application as external heat shields in supersonic vehicles, scratch studies were conducted on the $\text{ZrB}_2\text{-SiC}$ composite. These studies revealed metal-like slip-line patterns which are indeed an unusual in brittle solids at room-temperature. Utilizing classical stress field solutions under combined normal and tangential loads, a rationale was developed for understanding the formation of scratch-induced deformation features. Also, an analytical framework was developed, combining the concept of 'blister field' and the 'secular equation' relating Raman peaks to strain, to measure scratch-induced residual stress employing micro-Raman spectroscopy.

Transmission electron microscopic investigations confirmed the existence of dislocations within the ZrB_2 phase. It has been argued here that readily detectable slip-line patterns are reflection of metallicity in chemical bonding present in ZrB_2 ceramics which has also been suggested in recent literature from chemical bonding and electronic structure investigations.

CHAPTER 1 ADVANCED STRUCTURAL CERAMICS AND COMPOSITES

1.1 Introduction

Advanced ceramics and their composites with light weight, high strength and superior thermo-mechanical properties are central to the development of structural components for advanced military and aerospace applications. Among these, armor ceramics for personal and vehicle protection against impact threats,¹ and ultrahigh temperature ceramics (UHTCs) for leading edge components in hypersonic and reusable launch vehicles have received considerable attention in recent years.² In these applications, demand for materials with controlled and defect free microstructure is paramount. Therefore, the need for non-conventional processing techniques and advanced characterization techniques has increased rapidly. A major disadvantage of the traditional powder processing/sintering methods is that they do not lend themselves to rapid processing due to long processing times and elevated temperature requirements.³⁻⁵ Towards this end, a new processing method called “plasma pressure compaction”,⁶⁻⁹ also called “spark plasma sintering” (SPS), has been used to process two materials: (1) fine-grained boron carbide (B_4C) ceramics (used for body armor), and (2) a zirconium diboride - silicon carbide (ZrB_2-SiC) composite (a potential UHTC ceramic for applications in aerospace and military applications).²

In this dissertation, mechanical response of fine-grained B_4C ceramics has been investigated employing static and dynamic indentations where as the ZrB_2-SiC composite has been subjected to scratch experiments. Several issues such as processing of advanced ceramics, localized phase transformation in B_4C ceramics, deformation-induced residual stress measurements as well as evolution of

microplasticity in ZrB₂-SiC composite have been explored throughout this dissertation. These two structural ceramics have different deformation mechanisms and hence, they have been discussed in separate sections and/or chapters.

1.2 Materials

1.2.1 Boron Carbide (B₄C)

Boron carbide (B₄C) ceramic is an excellent candidate material for structural applications at room and high temperatures because of its high melting temperature (2450°C), high elastic modulus (450 GPa), high hardness (Vickers hardness > 25 GPa, next only to diamond and cubic boron nitride), high flexural strength (350-500 MPa), low density (2.52 g/cm³) and excellent wear resistance.¹⁰⁻¹⁶ B₄C is used as grinding medium for hard materials, lightweight ceramic armor, wear resistant sandblasting nozzle material, and as neutron absorber in nuclear reactors.^{10,17}

Due to its low density (2.52 g/cm³), high strength and high hardness, B₄C was expected to exhibit superior performance as armor ceramic for protection against projectile impact threats. However, under high velocity and high pressure conditions, B₄C has been shown to undergo significant strength degradation.¹⁸ Using high resolution transmission electron microscopy (TEM) on the ballistic fragments of B₄C, Chen *et al.*,¹⁸ revealed that B₄C undergoes localized collapse of the crystal lattice due to solid-state phase transformation from crystalline phase to amorphous phase during the impact. The amorphous phase, being weaker than the crystalline phase, is argued to be responsible for the observed loss of impact resistance in B₄C armor against high velocity projectile threats.

The above fundamental studies are indeed of great value but the costs and time associated with such ballistic experiments and preparation of large B₄C tiles (of several

tens of centimeters in dimensions) for impact experiments are expensive. In such situations, new experimental techniques that can induce similar deformation mechanisms in small specimen sizes (of 3-4 mm in size) can be of high economic value. Impact experiments not only involve high pressure but also high strain rates of loading which increases with projectile velocity.¹⁹⁻²¹ While the traditional indentation experiments with sharp point indenters can generate a large pressure at a moderate load within the materials, they are unable to capture high-strain rate effect comparable to impact experiments.²²⁻²⁶ Towards this end, a dynamic indentation method^{27,28} can be a better test technique to characterize the deformation mechanisms in armor ceramics. This technique not only delivers load in a controlled manner, similar to static indentation test method, but also produces strain rate of the order of $10^3/s$ which are essential to mimic ballistic impact tests in laboratory conditions. Thus, this dynamic indentation method (will be described later in detail) can be effectively used to augment the ballistic impact tests to uncover similar phenomena because of its ability to provide high pressure and high velocity loading into a small-localized region.

1.2.2 Zirconium diboride – silicon carbide composite (ZrB₂-SiC)

Development of novel light weight and high strength materials which can withstand elevated temperatures (above 2000°C), and provide good thermal insulation properties are crucial to meet future demands of many civilian, defense and aerospace applications.²⁹⁻³¹ Components (e.g., nozzles, propulsion components, leading edge materials for space vehicles and thermal protection systems) for future high performance aircrafts, hypersonic vehicles, kinetic energy interceptors and reusable space planes, etc. operate in severe reactive environments with temperatures well above the melting points of traditional materials. Few materials can withstand such high

temperatures and yet provide adequate mechanical strength.³² Ultra-high temperature materials (UHTMs) have been identified as the potential candidates for these applications.^{2,33,34} UHTMs are a class of materials that are chemically and physically stable at temperatures above 2000°C and in reactive atmospheres (e.g., monatomic oxygen). A sub-class of these materials is ultra-high temperature ceramics (UHTCs) which are borides, nitrides and carbides of transitional metals (e.g., Ta, Hf, Zr).² These ceramic materials (e.g., ZrB₂, ZrC, HfB₂, HfN, HfC) have high melting point above 3200°C. Other materials that may also fall in this UHTMs category are silicon carbide (SiC), graphite and rhenium (Re).²⁹ Among these, Graphite and other carbon-based materials degrade rapidly at temperatures above 800°C due to oxidation. Rhenium has high strength and high melting point but is extremely dense (21 gm/cm³) and oxidizes easily.^{35,36}

In this family of UHTCs, zirconium diboride-silicon carbide (ZrB₂-SiC) composites^{2,37-40} have drawn a special attention owing to their unique properties such as high melting point (> 3000°C), superior oxidation resistance above 1500°C, excellent thermal shock resistance, low density (6.09 gm/cm³) and good mechanical and chemical stability at elevated temperatures. Most of the recent investigations have been mainly focused on processing and oxidation behavior of ZrB₂-SiC composites.³⁷⁻⁴⁸ Mechanical characterization of ZrB₂ has been limited to the determination of static hardness^{2,49,50} fracture toughness,^{2,47,49,50} Young's modulus,^{2,50,51} creep response,⁵² room and high temperature flexural strength,^{2,46,47,53} and high temperature arc jet testing.⁵⁴ While in service (e.g., during takeoff, landing, or reentry in to atmosphere), the structural components in aerospace vehicles are prone to impact by meteorites and

atmospheric debris particles at very high velocities. Under such abrasion-dominated wear scenarios (abrasive wear), sharp particles impacting on the exposed surfaces can result in inelastic deformation and material removal. Therefore, evolution of damage and fundamental inelastic deformation mechanisms should be fully understood to evaluate the suitability of $\text{ZrB}_2\text{-SiC}$ composite for the above mentioned applications. Although these composites are intended to be used at high temperatures, investigation of mechanical responses at room temperature constitutes the first step towards a better understanding of their inelastic behavior in service.

The rest of the dissertation is organized as follows. In Chapter 2, the processing method to consolidate B_4C and $\text{ZrB}_2\text{-SiC}$ is discussed. The mechanical response of B_4C ceramics under static and dynamic indentations as well as spectroscopic investigations of structural phase transformation are discussed in Chapter 3. Then, the scratch induced deformation features in $\text{ZrB}_2\text{-SiC}$ composite and residual stress measurements within the particulate phase (SiC), using micro-Raman spectroscopy, are discussed in Chapter 4. The transmission electron microscopic studies of the deformed regions of the $\text{ZrB}_2\text{-SiC}$ composite are discussed in Chapter 5. Finally, in Chapter 6 conclusions and future research directions are outlined.

CHAPTER 2 PROCESSING OF ADVANCED CERAMICS

2. 1 Introduction

In this dissertation, two advanced structural ceramics, one for armor applications and other for high-temperature aerospace applications, have been developed. Due to their high melting temperature and strong covalent character of chemical bonding, processing of these ceramics is challenging. Use of traditional sintering methods requires high sintering temperature, moderate-high pressure, and often long consolidation time to produce sintered compacts with high density. In the following, literature on the processing of these ceramics, using conventional sintering techniques, is discussed first. Then, principle of a new and unconventional sintering technique called plasma pressure compaction ($P^2C^{\text{®}}$) is discussed followed by separate discussions on processing of B_4C ceramics and ZrB_2 -SiC composite employing $P^2C^{\text{®}}$ method.

2.2 Literature on Processing of B_4C Ceramics

Processing of pure boron carbide, using traditional sintering techniques, is challenging due to the difficulty associated with sintering of the starting powder. This is attributed to the high covalent bonding and low self-diffusion.¹⁰ As a result, high temperatures and high external pressures are required to produce dense B_4C ceramics. Traditionally, boron carbide has been consolidated using several sintering techniques such as (i) hot-pressing (HP) with and without sintering additives,^{10,55,56} (ii) hot isostatic pressing (HIP),^{10,57} (iii) pressureless sintering (PS) in the presence of sintering additives,^{10,11,13-15,58,59} (iv) pressureless sintering in a gaseous atmosphere of hydrogen and helium,⁶⁰ and (v) microwave sintering.⁶¹ Among the above powder processing

techniques, hot-pressing and pressureless sintering are the most commonly employed methods to produce boron carbide ceramics with 95 - 99 % of theoretical density and with grain sizes in the range between 1.5 - 60 μm . However, in hot-pressing and pressureless sintering methods, the sintering temperatures used were relatively high ($> 2000^\circ\text{C}$) and the sintering times were on the order of hours. In these sintering techniques, sintering additives are often used which aid the densification of difficult-to-sinter ceramic powders. However, the addition of sintering additives was found to reduce fracture strength moderately due to formation of weak glassy phases at the grain-boundary regions.⁵⁹ Also, these sintered ceramics with sintering additives are not suitable for nuclear applications¹⁰ where high purity boron carbide is required for neutron absorption. Although, dense boron carbide ceramic can be produced at lower temperatures using hot isostatic pressing, this method is not suitable for bulk processing.^{10,57} Boron carbide powder heat-treated in a gaseous mixture of hydrogen and helium and then sintered in the presence of pure helium also requires sintering temperature above 2200°C .⁶⁰ Microwave sintering has also been used to consolidate boron carbide (95 % density) in a short duration of time (12 min) but it also requires high temperatures above 2000°C .⁶¹ This limitation is overcome by using $\text{P}^2\text{C}^\text{®}$ technique as described in section 2.3.

2.3 Literature on Processing of $\text{ZrB}_2\text{-SiC}$ Composite

Ultra high-temperature ceramics such as ZrB_2 is also a difficult-to-sinter material due to the highly covalent nature of chemical bonding.² ZrB_2 and its composites have been produced by several conventional consolidation techniques such as (i) pressureless sintering (PS), (ii) hot-pressing (HP) and (iii) reactive densification process

such as reactive HP. In these techniques, high sintering temperature ($\geq 2000^{\circ}\text{C}$) and long consolidation periods are required to obtain dense ZrB_2 ceramics. In PS method, using fine starting powder particles, dense ZrB_2 ceramics ($\sim 95\%$) was achieved above 2000°C sintering temperature in the presence of large amount of sintering additives.^{62,63} In HP technique, high sintering temperature ($>2000^{\circ}\text{C}$) and pressure (>25 MPa) along with long consolidation times were required to produce dense ($>95\%$ of theoretical density) ZrB_2 ceramics.⁶⁴⁻⁶⁶ Some recent studies have produced 99% dense ZrB_2 ceramics at 1900°C (consolidation time of 45 min and pressure of 32 MPa).⁶⁷ However, fine milled ZrB_2 powder particles (500 nm) were used to reduce the sintering temperature. In reactive HP technique, synthesis and densification processes are combined utilizing *in situ* reaction and sintering processes to produce dense ceramics.² Although, this method has the advantage of producing extremely fine reactants due to *in situ* reaction, long consolidation times often result in significant grain coarsening at lower temperatures. Therefore, higher sintering temperatures are still required to produce dense ZrB_2 ceramics. Using this reactive HP method, dense ZrB_2 (99%) was produced at a sintering temperature of 2100°C .⁶⁸ Some of the recent studies have shown the advantage of using sintering additives to reduce the sintering temperature.² However, owing to the intended high-temperature applications, use of sintering additives is detrimental as the presence of glassy phase in the sintered compact can reduce the strength at high-temperature considerably.

In recent years, researchers have shown that only pure ZrB_2 is not suitable for high temperature applications as it is prone to oxidation.² Towards this end, ZrB_2 -SiC composites have received considerable attention due to their improved oxidation

resistance.^{2,37-40} Also, addition of SiC has been shown to improve the densification behavior and mechanical properties of ZrB₂ considerably.^{2,47,50,53} Processing conditions to produce dense ZrB₂-SiC composites mainly depend on the amount of SiC phase and the starting powder particle size. Using HP technique, ZrB₂-SiC composites (from 10-30vol% SiC content) have been sintered in the temperature range of 1800-1950°C (with pressure and consolidation time ranging from 20-50 MPa and 20-60 mins, respectively) to produce dense compacts.^{38,47,50,53,69} Chamberlain et al.,⁴² utilized reactive HP to produce dense ZrB₂-30vol%SiC composite at 1700°C where a pressure of 40 MPa was applied over a period of one hour. However, as mentioned before, due to the *in situ* reaction the reactants were extremely fine (below 100 nm) and thus, reduced the sintering temperature considerably. Zhang et al.,⁷⁰ produced ~98% dense ZrB₂-SiC composite using reactive HP at 1900°C at a pressure of 30 MPa and over a consolidation period of one hour. In the current work, P²C[®] technique has been utilized to produce a ZrB₂-SiC composite at significantly lower temperature and processing time which will be discussed in the following section.

2.4 Plasma Pressure Compaction Technique

In recent years, plasma pressure compaction (P²C[®]) has evolved as a promising powder consolidation method for sintering of metallic, ceramic and intermetallic particles.⁶⁻⁹ Unlike the traditional sintering techniques where consolidation times are on the order of several hours, in P²C[®] method various materials, metals, alloys and ceramics, have been successfully sintered to full density in less than 10 minutes. Sintering via this technique involves plasma activation and localized resistive heating (i.e. Joule heating) of a powder compact through the application of a low voltage direct

current (DC).⁶⁻⁹ Bonding of the particles is accomplished in two stages: first an in-situ elimination of surface oxide and contaminants due to application of the pulsed DC voltage (~ 5 V), and then consolidation of the purified powder through “Joule” heating by application of continuous DC voltage.

In this technique, powders are first compressed in a die (graphite, C-C, steel, or Mo-alloys) by external pressure to establish a current path and then pulsed DC voltage is applied for surface activation. As the effective current path is not established at the beginning, current does not flow freely through the powder compact. Thus, a charge, build-up at the interparticle gaps, causes polarity differences between the particles. As the charges accumulate, voltage difference becomes sufficiently large so that a spark is generated which triggers an ionization process i.e. interparticle plasma. The ions move toward the negatively charged particles where as electrons move toward the positive charged particles. These ionic and electron bombardments (impact of plasma) lead to the removal of oxide layer, impurities, moisture and adsorbed gas present on powder particle surfaces. This process, thus, results in cleaned particle surfaces for subsequent densification. Upon application of a DC voltage, current concentrates at the interparticle contact areas (which establish current path) and enormous heat is generated at these areas through “Joule” heating. This results in softening of those contact areas and result in plastic deformation as the external pressure is increased. Thus rapid densification, over a consolidation period of 5-10 mins, is facilitated through micro-welding and plastic yielding mechanisms. Surface purification and rapid consolidation result in a dense microstructure with minimum grain growth and contamination. A schematic of the P²C[®] equipment is shown in Fig. 2-1.

2.4.1 Processing of Fine-Grained B₄C Ceramics

Commercially available B₄C powder (Grade HS, H.C. Starck, Germany), with particles of sizes 100 - 500 nm, was used as the starting material.⁷¹ The powder was consolidated using P²C[®] method under high vacuum (200-300 mTorr) without the use of any sintering aids. In the current work, the powder compact was consolidated at a constant low voltage (~5 V) direct current and a maximum current density of 4400 amp/cm². Simultaneously, an external pressure (88 MPa) was applied to assist powder consolidation. The sintered compacts were produced in the form of a cylindrical disk of 51 mm diameter and 6.4 mm thickness, see Fig. 2-2. These disks were sintered either at a temperature of 1650°C or 1750°C and the consolidation time was varied between 2 to 30 min. Table 2-1 shows the processing conditions for all the disks. Densities of the sintered disks were measured using Archimedes method. Microstructural analysis was performed on both fractured and polished surfaces. Polished specimens were prepared by using standard metallographic principles. The polished surfaces were etched electrolytically using 1% KOH solution at a current density of 0.03 amp/cm² for 30 seconds.⁷¹ From the electrolytically etched specimens, average grain size was determined (by the line intercept method) as per ASTM standard E 112-96. Table 2-1 provides the density measurements and average grain sizes of the B₄C ceramics. Sintered B₄C compacts produced at 1650°C attained only 92-93 % of theoretical density and thus were not considered for further investigation.

Upon increasing the sintering temperature to 1750°C a significant improvement in density was observed. Compacts consolidated for 2 min and 5 min at 1750°C attained densities around 96% and 99% of the theoretical value, respectively. When

consolidation time was increased to 30 min at this temperature, no further increase in density was noticed. The improvement in density (or decrease in porosity level) with increase in temperature is clearly evident from the SEM micrographs of the fractured surfaces shown in Fig. 2-3. Microstructures of the polished and electrolytically etched specimens from the three B₄C disks produced at 1750°C are given in Fig. 2-4. Optical micrographs revealed nearly equiaxed and fine-grained microstructures with average grain sizes around 1.6 μm, 2 μm and 2.7 μm for the samples sintered for 2 min, 5 min and 30 min, respectively. Darker regions in the micrographs represent mostly grain pull-outs during polishing. From the density and average grain size measurements it is clear that the processing parameters (temperature, pressure and consolidation time) adopted in the current work were appropriate for the production of dense fine-grained boron carbide ceramics.

2.4.2 Processing of ZrB₂-5wt%SiC Composite

In the current work, commercially available ZrB₂ powder (Grade HS, H.C. Starck, Germany), with particles of sizes between 3-7 μm, and polycarbosilane (-(SiHMe-CH₂)_n-) powder were used as starting materials.⁷² Polycarbosilane (PCS) has a silicon-carbon (Si-C) backbone and is used as a preceramic precursor for SiC.⁶⁹ Initially, the powders were mixed in a shear mixture and the blend was calcined above 1000°C in an atmosphere of flowing argon where the PCS decomposed to cubic-SiC (β-SiC) and amorphous carbon. Then ZrB₂ and heat-treated PCS mixture were further mixed, and consolidated using the P²C[®] technique at a temperature of 1750°C and at a pressure of 43 MPa over a short consolidation period of only 5 min.⁷² Density of the sintered ZrB₂-SiC composite was measured using Archimedes method. X-ray diffraction (XRD)

analysis was carried out on small specimens to investigate the phase content within the consolidated compact. Some fragmented pieces were examined using scanning electron microscope (SEM) to reveal the average grain size in the composite. Figure 2-5 shows a ZrB₂-5wt% SiC composite slab of 75mm×52mm×8mm was produced using (P²C[®]) technique and Fig. 2-6 reveals low and high magnification SEM micrographs of fractured surfaces of the composite.

XRD pattern collected from the sintered composite, shown in Fig. 2-7, revealed the presence of only two crystalline phases; hexagonal (*H*) ZrB₂ and cubic (3C) SiC. Density measurements indicated a composite density 96% of theoretical value (5.84 g/cm³). The theoretical density of the composite was calculated using the rule of mixture. SEM micrographs of the fragmented surface, shown in Fig 2-6, revealed a well-consolidated composite and thus supported the high value of measured density. No porosity was detected within the ZrB₂ matrix as well as at the ZrB₂-SiC interface areas. However, some agglomerated regions (containing 3C-SiC and amorphous carbon) were observed in the sintered compact which probably resulted the measured 4% porosity. SEM micrographs revealed that the SiC phase (dark phase) was uniformly distributed within the ZrB₂ matrix (gray phase). Nevertheless, microstructural observations indicated that P²C[®] method was successful in producing a uniform and well-consolidated ZrB₂-SiC composite. From the SEM micrographs of the fractured surfaces, average grain size of the ZrB₂ phase was estimated to be around 5 μm whereas the SiC particles were around 1 μm in size.

2.5 Conclusions

Boron carbide powder sintered using the P²C[®] technique resulted in near theoretically dense and fine-grained boron carbide ceramic disks at significantly lower processing time and temperatures than in conventional sintering methods. A polycrystalline ZrB₂-5wt.%SiC composite, with a consolidated density above 96% of theoretical density, was produced using the P²C[®] technique at a temperature of 1750 °C and at a pressure of 43 MPa over a short consolidation period of only 5 min.

As outlined in Chapter 1, in the following chapters, mechanical responses of P²C[®] processed B₄C ceramics and ZrB₂-5wt%SiC composite are discussed in detail. Since, the issues being investigated different, they are discussed in separate chapters. In the following Chapter 3, static and dynamic indentation response as well as phase transformation studies in B₄C are discussed.

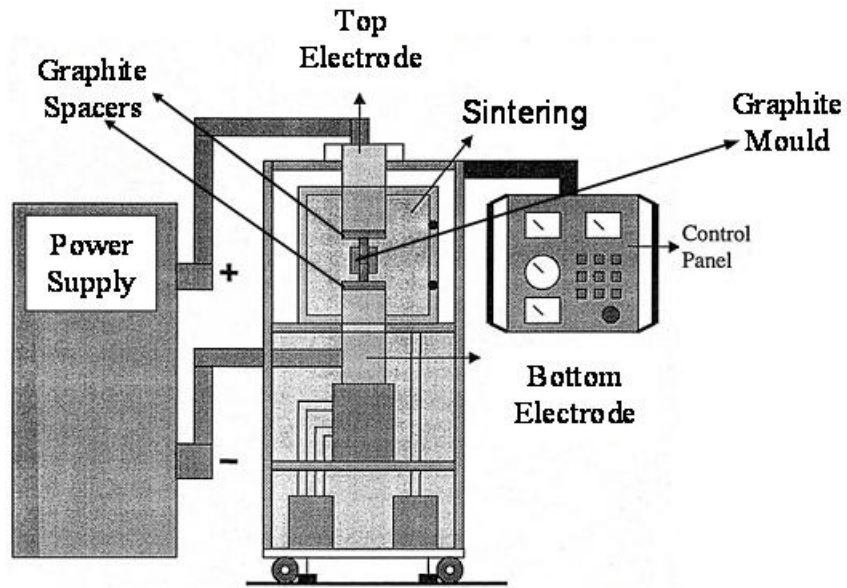


Figure 2-1. Schematic of a P²C[®] equipment.

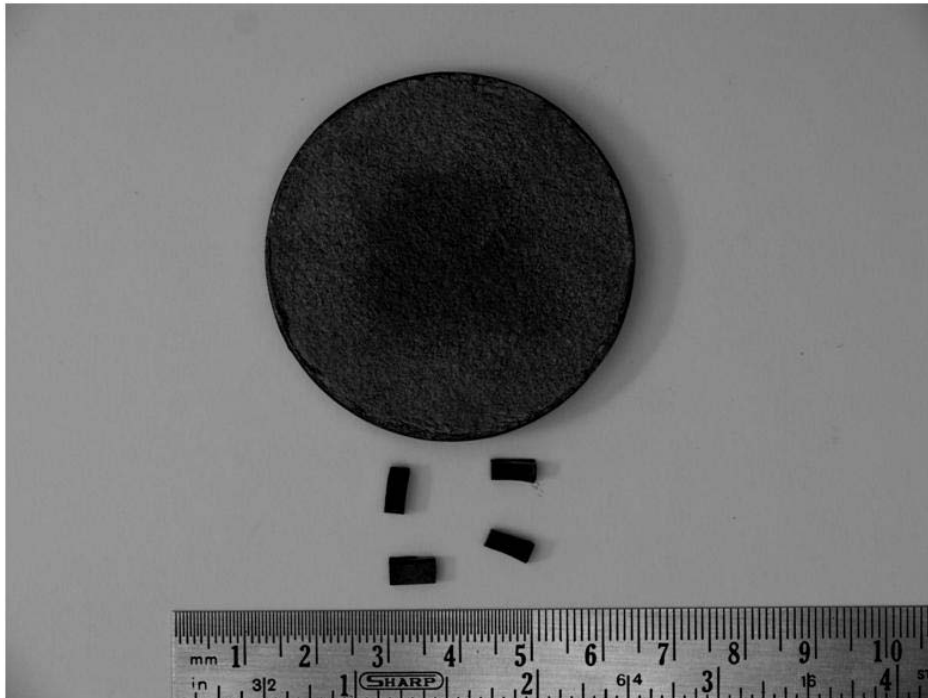


Figure 2-2. Consolidated boron carbide disk and test samples for indentation.

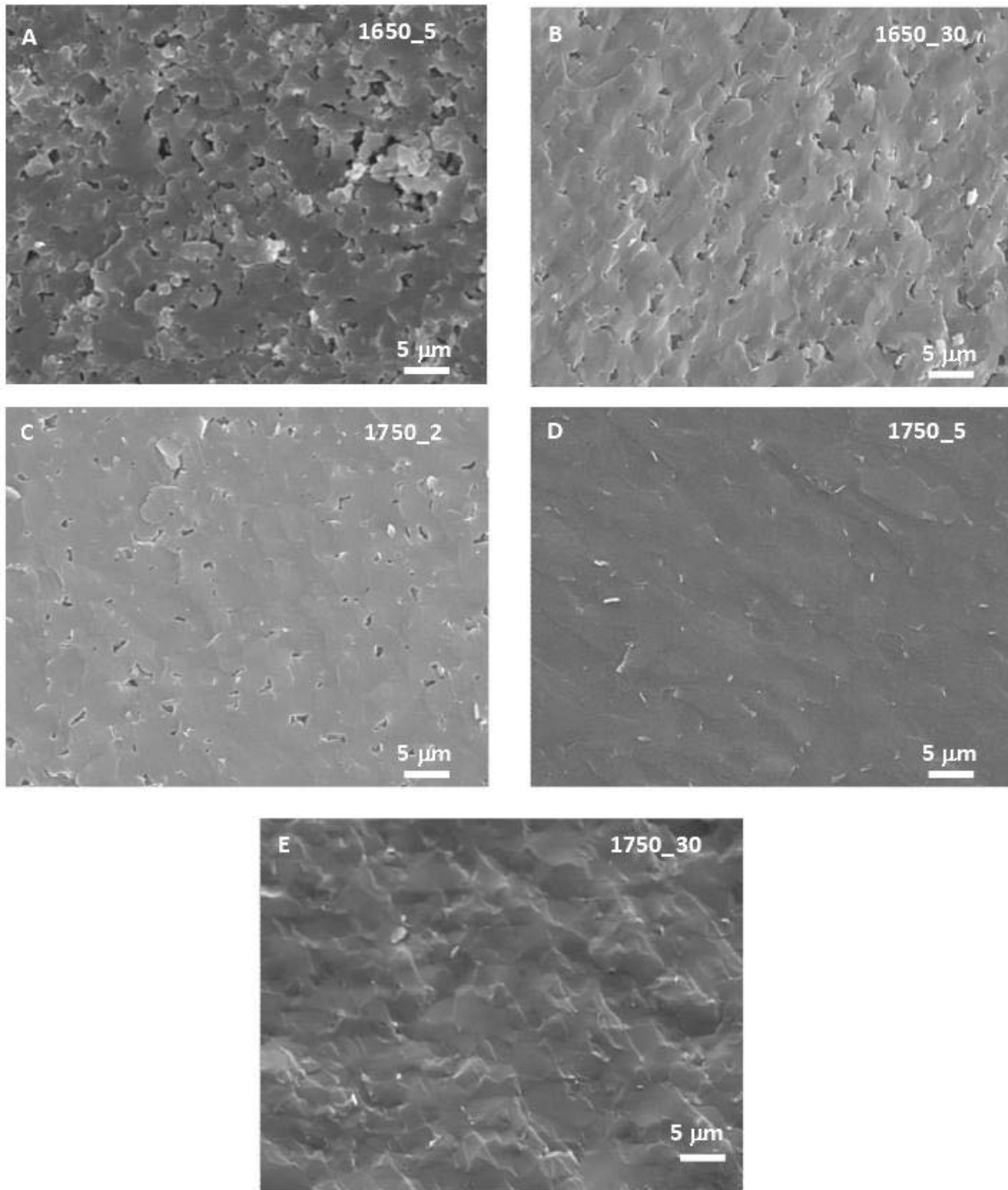


Figure 2-3. SEM micrographs of sintered B_4C samples at various processing temperatures and time.

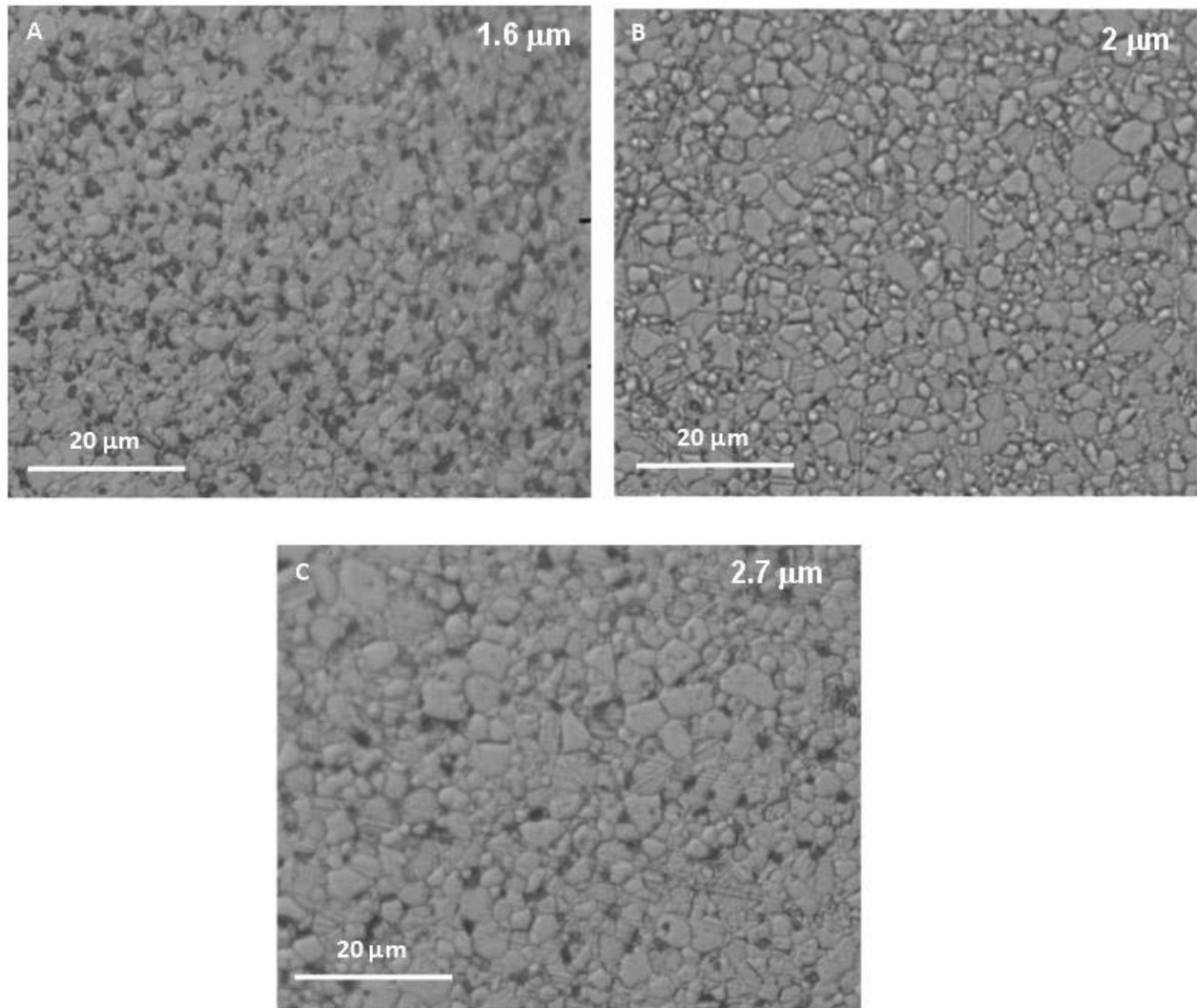


Figure 2-4. Optical micrographs of the etched sintered B_4C samples sintered at $1750^{\circ}C$ for A) 2, B) 5 and C) 30 min. The average grain sizes are indicated on the optical micrographs. Darker regions in the micrographs represent mostly grain pull-outs during polishing.

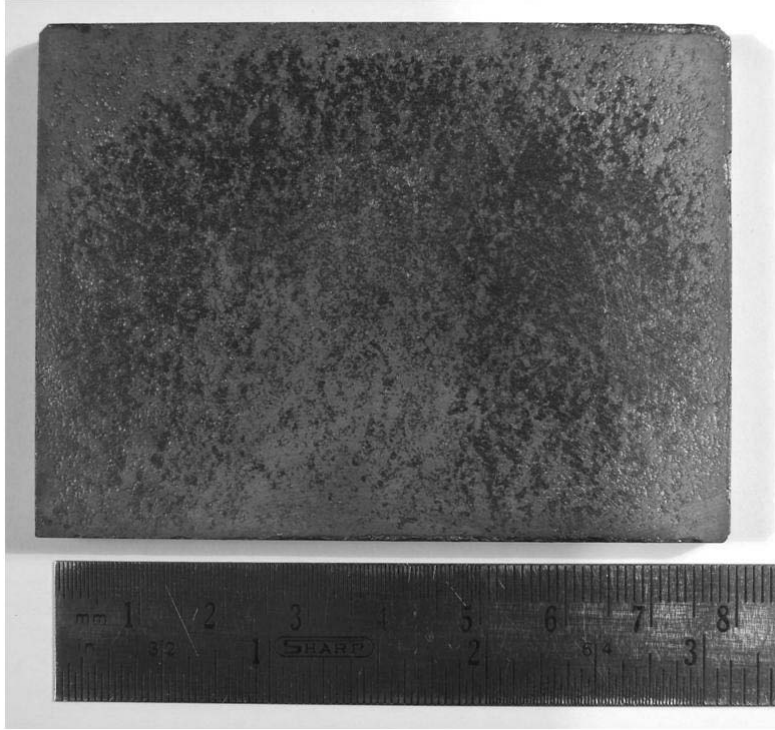


Figure 2-5. A ZrB_2 -5wt%SiC composite sintered using $\text{P}^2\text{C}^\circledR$ technique.

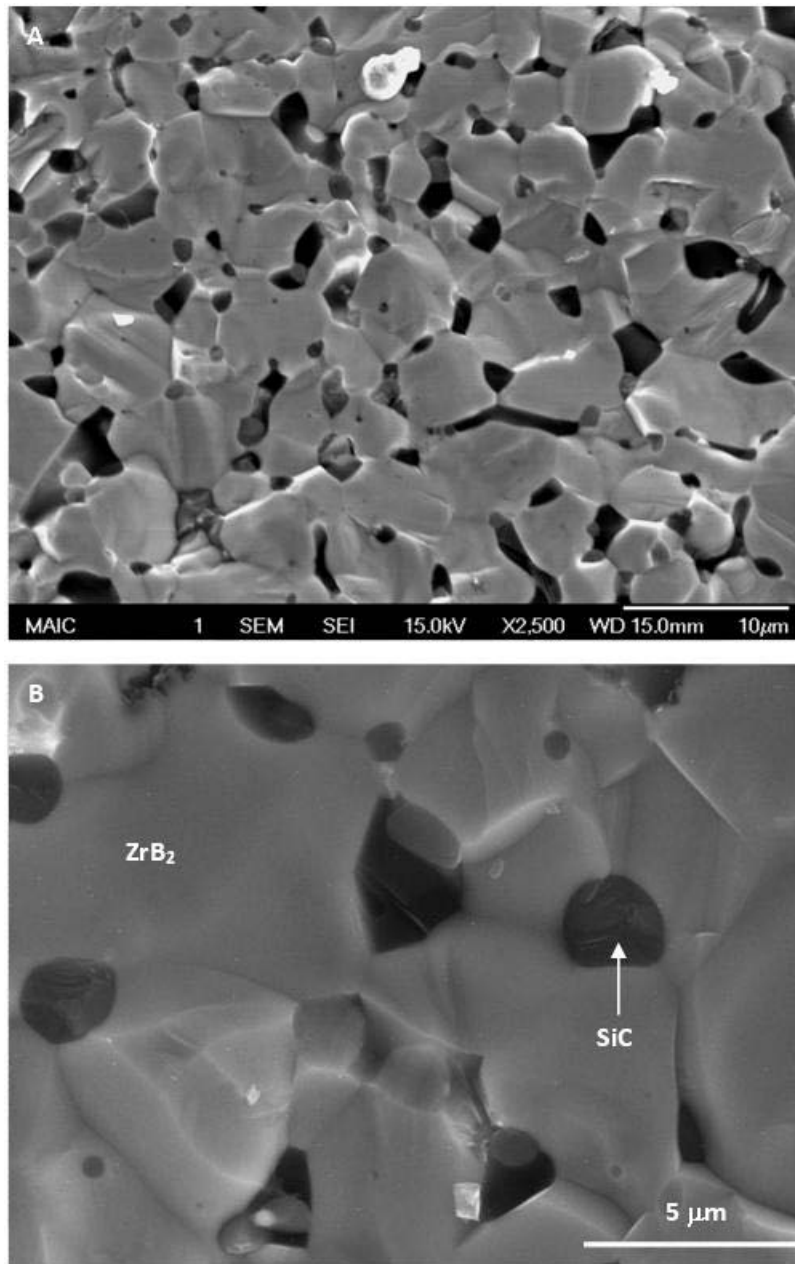


Figure 2-6. A) SEM micrograph of the fragmented surface of ZrB₂-SiC composite and B) a higher magnification SEM image revealing absence of any porosity within ZrB₂ matrix as well as at the ZrB₂-SiC interface areas.

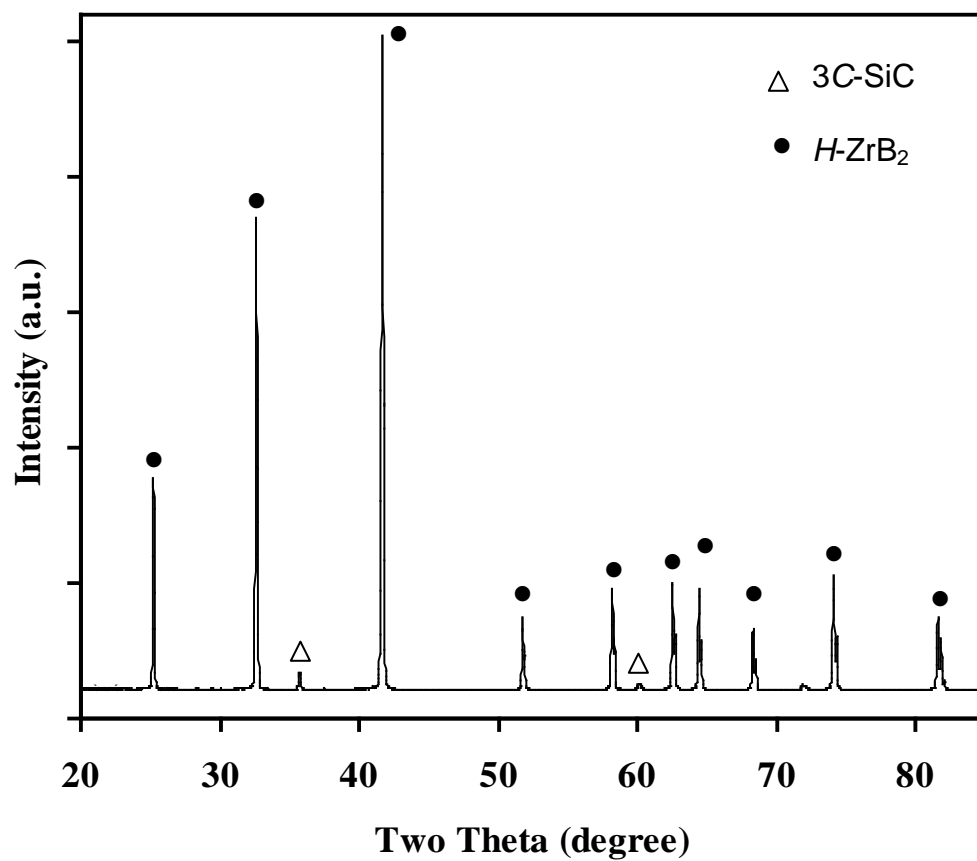


Figure 2-7. XRD pattern collected from the sintered ZrB₂-SiC composite.

Table 2-1. Processing conditions in P²C[®] method for sintering of B₄C compacts

Sample ID	Temperature (°C)	Time (mins)	Pressure (MPa)	Density (% theoretical) (g/cc)	Grain size (µm)
1650_5	1650	5	88	2.33 ± 0.002 (92.46 %)	Not measured
1650_30	1650	30	88	2.35 ± 0.003 (93.25 %)	Not measured
1750_2	1750	2	88	2.42 ± 0.002 (96 %)	1.6
1750_5	1750	5	88	2.50 ± 0.004 (99.2 %)	2.0
1750_30	1750	30	88	2.50 ± 0.004 (99.2 %)	2.7

CHAPTER 3 DYNAMIC INDENTATION RESPONSE OF B₄C CERAMICS

3.1 Introduction

In this work, strain rate sensitivity of boron carbide ceramics has been studied using dynamic and static indentation experiments. These experiments were conducted on the intact as well as on the split specimens (prepared using bonded-interface technique). Hardness measurements were performed on intact specimens where as the split specimens were utilized to probe, using a series of spectroscopic techniques, the subsurface damage regions of both types of indentations for structural phase transformation in B₄C. Rest of the Chapter is divided into two sections. In the first part (section 3.2), results from the static and dynamic indentation studies are discussed followed by an in-depth discussion, in section 3.3, on spectroscopic investigation of structural phase transformation in B₄C.

3.2 Static and Dynamic Indentations

3.2.1 Static Indentation Fracture

Since the advent of fundamental pioneering concepts in fracture by Inglis,⁷³ Griffith,⁷⁴ Irwin,⁷⁵ and Orowan,⁷⁶ the field of fracture mechanics has evolved into a mature subject and is regularly practiced in design of structures subjected to a wide range of loads. Advances in materials research and their applications in emerging fields continue to identify new fracture phenomena that challenge researchers to develop new analytical, computational and characterization tools, and provide further insight in to their failure behavior. In recent years, several mechanical characterization techniques such as instrumented nanoindentation, dynamic indentation and micro- and nano-scratch experiments have been successfully employed on brittle materials to unravel fundamental

mechanisms associated with fracture and material removal at nano- and micro-levels during high-speed grinding, dynamic wear and ballistic impact phenomena.

Among many characterization techniques available, indentation fracture mechanics approach has been one of the most popularly used methods to evaluate the fracture resistance of brittle materials.^{19,22-26,77-79} The field of static indentation fracture mechanics has made significant contributions to our understanding of fracture behavior of brittle solids and material removal mechanisms during abrasion and wear. Investigations have ranged from indentation fracture mechanics of monolithic brittle solids to indentation of hard particles embedded in ductile materials (e.g., carbides in tool steels).⁸⁰ In addition to their ability to extract fundamental fracture characteristics of brittle solids, indentation tests have often provided motivation for development and/or validation of sophisticated numerical models. However, this approach has been mostly applied to static loads and its use for dynamic deformation of materials has been limited.

Numerous applications involve rapidly applied loads where dynamic or high strain rate effects become relevant. For example, in high-speed grinding of ceramics, the grinding grit is in contact with the work piece for only few tens of microseconds. During impact of a projectile on a confined ceramic target the interaction time between the two contact surfaces is on the order of few microseconds. Similarly, the rate effects may be important in applications such as dynamic wear between two rapidly moving surfaces, meteorite impact on space structures, runway debris impact on airplane structures, atmospheric particles impact on the protective tiles of a reentry vehicle, etc. In all these events, the interaction between the two contact surfaces can be considered as Hertzian,⁸¹ however, the static indentation mechanics principles cannot be fully applied to analyze the dynamic inelastic deformation behavior that is germane to such dynamic events because

the contact time is on the order of few tens of microseconds. Materials under dynamic loads can experience strain rate well in excess of $10^3/s$ and, at such high strain rates, the deformation behavior in brittle materials, in general, is characterized by increased fracture strength^{27,82-90} and fracture toughness.^{28,91-100}

3.2.2 Dynamic Indentation Fracture

Understanding of projectile-target interaction is central to the development of superior armor/anti-armor materials. For design of efficient composite armor systems such as metal/ceramic or polymer/ceramic armor, the interfacial characteristics as well as the deformation and fracture characteristics of individual components must be well understood. Fundamental investigations that have provided key insights into the interactions between a metal projectile and a ceramic target have been conducted by several researchers.^{1,20,21,101-114} A survey of candidate ceramic armor materials and the relevant experimental data have been compiled by Holmquist *et al.*¹¹⁵ Through proper target design, Hauver *et al.*,^{116,117} were able to increase the resistance to penetration of a ceramic target by extended lateral flow at the surface of the ceramic and thus recover intact ceramic target after the impact. This was achieved by confining the ceramic within steel case, by providing space for erosion products, and providing a shock attenuator and a steel plate at the entrance to the target. Under these conditions, microstructural analysis of the impacted ceramic targets has revealed similarities of fracture patterns to the ring cracks induced by static indentation of a hard sphere on a ceramic which clearly demonstrated the validity of “contact mechanics” approach to investigate the damage due to projectile impact on ceramics. Therefore, modeling efforts to describe impact damage in ceramics have centered around Hertzian contact theory coupled with brittle fracture models in compression.^{81,118,119}

Although the similarities between induced-damage in a confined ceramic target due to projectile impact and that induced due to a static spherical indentation are well recognized, the rate effects that are germane to dynamic impact phenomena are not fully captured in static indentation investigations. In addition, modeling efforts that seek to estimate pressure induced in the target due to impact are limited by the existing elastic-perfectly plastic models which fail to describe the stresses accurately in the comminuted region of the impact. Thus, the current contact mechanics approach to describe the physical phenomena ahead of a projectile suffers from some inherent limitations.

To overcome these limitations, several experimental, analytical and numerical approaches have been adopted in the recent literature. Towards these developments, Subhash and co-workers^{27,28,120-122} have developed a dynamic indentation test method to investigate the rate-dependent indentation properties of ceramics and metals. Here the word 'dynamic' refers to the time of loading which is only around hundred microseconds. This technique is based on the momentum trapping principle developed by Nemat-Nasser et al.,¹²³ for dynamic compression testing and is modified to impart a single indentation in to the specimen during dynamic indentation. The technique has been successfully utilized to determine the dynamic Vickers indentation hardness of metallic materials,^{27,122} bulk metallic glasses^{124,125} and several ceramics.^{27,28} The above studies on metals are very generic in the sense that the dynamic hardness has been found to be three times the dynamic yield strength of a metallic material. This result is similar to the static hardness-yield strength relationship proposed by Tabor.¹²⁶ Recently, such test method has been successfully used to detect negative rate sensitivity of hardness in amorphous alloys.^{125,127} Also, in bulk metallic glasses, dynamic indentation revealed significant difference in shear band propagation phenomena compared to static indentation.¹²⁵

3.2.3 Dynamic Indentation Tester

Subhash and co-workers^{27,28} have adopted a dynamic indentation method to investigate rate-dependent indentation properties of metallic and brittle materials. In this technique, elastic stress wave propagation in a slender rod is utilized to deliver the desired load in 150 μ s duration compared to static indentation where load is applied over 10-15 seconds. This technique is parallel to the static indentation technique and therefore, a direct comparison between static and dynamic indentations can be made.

The dynamic hardness tester consists of a slender rod with a Vickers indenter mounted at one end and a momentum trap (MT) assembly at the other end as shown schematically in Fig. 3-1. A high frequency load cell Kistler mounted on a rigid base measures the load. The specimen is sandwiched between the diamond indenter and a load cell. A short striker bar is launched from a gas gun towards the MT-end of the incident bar, thus generating a compressive stress pulse followed by a tensile pulse (due to MT) of known duration and amplitude in the incident bar. The MT assembly ensures that only a single compressive pulse reaches the indenter thus causing the indentation and then the tensile pulse retracts the indenter. Furthermore, all the successive wave reflections will be tensile while traveling towards the indenter end thus causing the bar/indenter assembly to retract further away from the specimen. Therefore, single dynamic indentation on the specimen is ensured. The dynamic hardness is calculated based on indentation diagonal size and load similar like the static hardness.

3.2.4 Experimental

Static and dynamic indentation studies were conducted on three different grain sizes of B₄C ceramic produced by P²C® technique as discussed in Chapter 2. Approximately 15 static indentations were performed at each load of 2.94 N (300 gm), 4.9 N (500 gm) and

9.8 N (1000 gm) for 15 seconds on each grain size B₄C specimen. Unlike the static indentation tests at fixed loads, the dynamic indentations were conducted utilizing the dynamic indentation tester at loads between 2.94 N to 14.7 N by increasing the velocity of the striker bar in the dynamic indentation tester. Around 25-30 tests per specimen type were conducted at load ranges similar to those under static indentation.

3.2.5 Results of Indentation Experiments and Discussion

A plot of static and dynamic hardnesses vs. indentation load for the three grain sizes is presented in Fig. 3-2. A wide scatter in the static hardness values was observed for all the grain sizes. The average static hardness values for 2 μm and 2.7 μm grain size specimens appeared in the same range (27.45±2 GPa and 27.45 ±2.5 GPa) for the loads considered in this investigation. On the other hand, the 1.6 μm grain size sample, having the smallest grain size, showed relatively lower average static hardness value of 25.41±1.0 GPa. On the other hand, the dynamic hardness (HV_d) was lower than the static hardness for all the grain sizes in this load range. Unlike the static hardness values, the dynamic hardness values exhibited a greater scatter for all the grain sizes as can be seen from Fig. 3-2. The 1.6 μm grain size boron carbide showed a significant decrease in dynamic hardness compared to other two grain sizes. This decrease is probably due to the lower density (see Table 2-1) or higher level of porosity in these specimens. For the other two grain sizes, the trends between static and dynamic hardness values were difficult to conclude because of large scatter in the values and lack of sufficient number of data points.⁷¹

Cracks extending from the corners of the static and dynamic Vickers indentations were used for fracture toughness (K_{Ic}) measurements. Numerous empirical fracture

toughness relations are available in the literature depending on the nature of crack systems.¹²⁸ For half-penny cracks, the relationship between the half crack length c and load P is expected to be of type $c = AP^{2/3}$ where as for Palmqvist cracks, the difference between the half-crack length c and the half-diagonal, a , i.e., $l = c - a$, is expected to be linear with respect to load, i.e., $l = BP$. In the current work, the above quantities were plotted and fitted to an equation of type $y = bx^n$ to determine the nature of the crack system. The c vs. P plots yielded n values in the range of 0.62-0.69 and therefore, matched the equation $y = bx^n$ closely. On the other hand, the plots of l vs. P did not result in a linear relationship between l and P as the n values were found to be in the range of 0.68-0.92. These plots have been presented in Appendix A. Therefore, it was concluded that in the current work static and dynamic indentations resulted in half-penny crack system beneath the indentations. Accordingly, Evans and Charles fracture toughness equation,¹²⁸ $K_C = 0.0824P/c^{1.5}$, based on half-penny crack system has been used.

A comparison of optical micrographs of the top surface of the indented regions of 2.7 μm grain size specimen at an indentation load of 2.94 N is shown in Fig. 3-3. It can be seen that the dynamic indentations resulted in more severe damage compared to the static indentations. Measurements of crack lengths revealed that, in general, the half-median crack length (c) increased linearly with indentation load under both low and high strain rate loads. The average crack lengths were slightly longer under dynamic loads compared to static loads for all the grain sizes. Using the Evans and Charles equation, static and dynamic fracture toughness (K_C^s and K_C^d , respectively) values were calculated and plotted in Fig. 3-4. A wide scatter in the fracture toughness values was observed under both conditions. In general, fracture toughness was lower under dynamic loads compared to static loads.⁷¹

It is well-known that hardness increases with a decrease in grain size (the Hall-Petch relationship).^{129,130} Similarly, a decrease in residual porosity also improves the mechanical properties. But in the current work the 1.6 μm grain size boron carbide, having the smallest grain size, revealed the lowest static hardness which does not follow the well-known Hall-Petch relationship. No significant variation in hardness was observed between 2 μm and 2.7 μm grain size boron carbide specimens. The possible reason for such behavior may be the presence of higher level of residual porosity in small grain size boron carbide than that in the other two boron carbide specimens which have more than 99% theoretical density (see Table 2-1). This increase in porosity may offset the effect of smaller grain size on hardness. Since the larger grain size specimens did not show any variation in static hardness and they contain negligible porosity, it can be surmised that hardness is less influenced by the grain size variation (in the current grain size range) than porosity level at low strain rate loading. Under dynamic loading, hardness was observed to change significantly with grain size variation (Fig. 3-2 and Table 3-1). But as mentioned earlier, due to statistically insufficient amount of data, it is difficult to make any definitive conclusion except that the dynamic hardness for 1.6 μm grain size was significantly lower than static hardness. Again, the increased level of porosity might have offset the effect of smaller grain size which resulted in the observed drop in dynamic hardness in 1.6 μm grain size specimens. Therefore, it can be inferred that hardness of boron carbide is not only influenced by grain size and porosity level but also by strain rate. A significant lowering of dynamic hardness compared to static hardness in 1.6 μm grain size boron carbide indicates that residual porosity could be more detrimental to hardness under dynamic loading than under static loading. Similar conclusion can be made from the

fracture toughness measurements (Fig. 3-4 and Table 3-1) where a large drop in fracture toughness was observed for 1.6 μm grain size compared to other grain sizes under dynamic loading.⁷¹

Clearly, boron carbide revealed lower hardness (Fig. 3-2) and lower fracture toughness (Fig. 3.4) under dynamic indentation than those under static indentation. But this trend in the loss of mechanical properties of boron carbide at high strain rates contradicts the established trend for many other engineering materials where an increase in hardness, yield strength, fracture toughness and fracture strength have been observed under higher strain rate loading. To investigate the underlying cause for this anomalous behavior in boron carbide, further studies employing several spectroscopic techniques were conducted in the indented regions beneath the surface which is discussed in section 3-3.

For these purposes, subsurface damaged regions of indentations were probed using several spectroscopic techniques. To study the subsurface regions of indentations, rectangular specimens were cut into two halves along the length, and these cut surfaces were polished using standard metallographic polishing techniques. They were then bonded with high-strength adhesive and kept clamped for few hours. The top surface containing the bonded interface was polished flat for static and dynamic indentations along the interface. The indentation was performed with one of the diagonals of the indenter aligned parallel to the interface. For these subsurface damage studies, indentations were intentionally performed at slightly higher loads (up to 21 N) so as to cause sufficiently large damage zone beneath the indentation. After indentation, the bonded surfaces were separated and scanning electron microscopy (SEM) was performed to observe the subsurface damage.⁷¹

Scanning electron micrographs of the half indents (shown in Fig. 3-5) revealed that the subsurface damages for both types of indentations at similar load levels are significantly different. Under dynamic indentation the extent of damage in the lateral direction was significantly larger than static indentation and several cracks were observed to emanate from the boundary of the damage region as indicated in Fig. 3-5 (B). Such cracks are not evident under static indentations. These subsurface studies further confirm that boron carbide is more prone to damage under dynamic loading compared to static loading at similar load levels. Moreover, it is clearly seen that the damage zones appear to be half penny shaped beneath the indentation as previously assumed for calculation of indentation fracture toughness.⁷¹ In the following section, results of spectroscopic studies for structural phase transformation as well as effect of strain rate are discussed in detail.

3.3 Spectroscopic Investigation of Localized Phase Transformation

3.3.1 Localized Phase Transformation

The issue of localized amorphization in boron carbide ceramic has already been mentioned which was confirmed from transmission electron microscopy work.¹⁸ It has been suggested that such regions originated due to localized collapse of the crystal lattice as a result of the solid-state phase transformation from crystalline phase to amorphous phase.^{18,71,131,132} To reveal the exact mechanism behind such localized solid-state phase transformation, it is essential to understand the structure of amorphous B₄C. However, the exact structure and the composition of these amorphous regions present within impacted B₄C ceramics are still unclear.

Ge et al.,¹³¹ from their Raman spectroscopic analysis on the nanoindented regions of polycrystalline B₄C, have suggested the presence of sp^2 hybridized carbon (C) within α -B₄C. From similar nanoindentation work conducted on single crystal B₄C, Yan et al.,¹³²

suggested the presence of sp^2 C aromatic rings within a - B_4C . They also suggested, from the temperature coefficient measurements of Raman bands, that boron (B) atoms can form B-clusters or can substitute C atom from the aromatic rings. However, no direct evidence of B-cluster formation was provided. Using Gibbs free-energy calculations, Fanchini et al.,¹³³ interpreted that amorphization in B_4C may trigger from the collapse of $B_{12}(CCC)$ polytype instead of $B_{11}C(CBC)$, and a - B_4C may contain some segregated mixture of amorphous carbon (a -C) and boron icosahedrons (B_{12}). But any experimental evidence of the formation of a -C and B_{12} within amorphous bands is still lacking. Also, B_4C is widely accepted to have $B_{11}C(CBC)$ structures instead of $B_{12}(CCC)$.^{134,135} Therefore, the exact formation mechanism of B and C clusters within a - B_4C is still not well understood.

Spectroscopic techniques such as Raman spectroscopy, photoluminescence (PL) and Fourier transformed infrared (FTIR) spectroscopy are widely used to provide information and identification of chemical structures and physical forms.^{136,137} These methods are sensitive to the molecular vibrations and the electronic transitions. Since, every material has its unique vibrational and electronic transition characteristics (owing to chemical bonding features), spectroscopic techniques are widely used to identify the unknown structures. Although, Raman spectroscopy has provided some useful information on the phase transformation in B_4C and the structure of a - B_4C ,^{71,131,132} only use of this technique may not be sufficient to unearth all the structural information. Therefore, the aim of the current work is to provide more insight in to the structure of amorphous regions formed within B_4C ceramics. Here, spectroscopic evidence for the formation of a -C, created by static and dynamic indentations, has been provided along with the observed evidence of a -B cluster formation by dynamic indentation. This interpretation was rationalized based on a series of micro-spectroscopic techniques including Raman

spectroscopy (both uv and visible), photoluminescence, and Fourier transformed infrared spectroscopy. Before proceeding further with the experimental results and their interpretation, in the following, some of the fundamentals of vibrational and electronic spectroscopy are discussed briefly.

3.3.2 Fundamentals of Spectroscopic Techniques

3.3.2.1 Molecular vibration

Raman scattering and infrared absorption are based on the fundamental normal vibrational modes of chemical bonds of molecules, in any form (i.e., solid, liquid or gas).¹³⁶ There are only certain types of atomic displacements (i.e., nuclear motion) during molecular vibrations which are allowed with well-defined frequencies. These are known as the normal modes of vibrations and some of the types of motions which contribute to the formation of a normal mode are given below, also see Fig. 3-6,¹³⁶

stretching motion between two bonded atoms (symmetric and asymmetric)

bending motion between three atoms connected by two bonds

out-of-plane deformation modes that change an otherwise planar structure into a non-planar one

From a simple statement of Hooke's law, frequency (ν) of a simple fundamental normal mode of vibration of a molecular can be expressed as

$$\nu = \frac{1}{2\pi c} \sqrt{\frac{k}{\mu}}$$

where c is the velocity of light, k is the force constant and (μ) is the reduced mass expressed as $\mu = \frac{m_1 m_2}{m_1 + m_2}$ (m_1 and m_2 are the masses of the atoms constituting the

chemical bond).

3.3.2.2 Raman and infrared spectroscopy

Although both Raman and FTIR phenomena are fundamentally related to the vibrations of materials, the former is associated with the inelastic scattering event whereas the latter is related to the absorption of light.^{136,137} During interaction of light with a matter, the photons present within the light can either be absorbed or scattered, or the interaction can be negligible. In vibrational spectroscopy, the changes in the energies of the incident photons, caused by the nuclear motion, are detected. If the scattering process involves only a distortion of the electron cloud, then the changes in the frequency of the scattered electrons are negligible. This is considered as elastic scattering and called Rayleigh scattering. In contrast, if the scattering process induces nuclear motion, then energy will either be transferred from photon to molecule or vice-versa. This is called Raman scattering which is considered as inelastic scattering because here the energies (or frequencies) of the incident and scattered photons are different.

In any material, there are several electronic states present where each of the electronic states consists of a number of vibrational states. At room temperature, most of the molecules, in general, are present in the lowest energy vibrational level. In Raman spectroscopy, a material is irradiated with a light of single frequency and the resulting radiation due to the scattering process is detected. Figure 3-7 shows a simplified schematic of the Raman scattering phenomenon. As the material is irradiated with a source of radiation, electrons of the molecules, present in the ground electronic state, interact with the photons of the light source. During this event, Rayleigh process, see Fig. 3-7, will dominate since most of the photons scatter this way. However, a fraction of the molecules, initially present at some low energy vibrational energy level (e.g., ν_0) will not return to the same level, rather, will come back to a higher energy vibrational level (e.g.,

ν_2). As a result, the scattered photons will have lower energies compared to incident photons. This is called Stokes Raman scattering. In contrast, due to thermal energy at room temperature, some molecules initially may be present at higher energy vibrational level (e.g., ν_2) which will return to the lower energy level (e.g., ν_0) by releasing the extra energy. Therefore, the scattered photons will have higher energy compared to the incident photons. This is called anti-Stokes Raman scattering. However, at room temperature, number of the molecules present at an excited vibrational state instead of really low energy ones will be extremely small. Therefore, compared to Stokes scattering, anti-Stokes scattering is weak and becomes further weaker as the frequency of vibration increases owing to the decreased population of the excited vibrational states.¹³⁶

In contrast to Raman scattering, in infrared spectroscopy, a material is subjected to an infrared light source, consisting of a range of frequencies, and the absorbed frequencies from the light source are detected.^{136,137} Here at any frequency, within the infrared range, the absorption of light corresponds to a promotion of a molecule to an excited vibrational state. For example, Fig. 3-8 illustrates a simplified schematic of the absorption mechanism encountered in the infrared spectroscopy.

In any molecule, there are several types of normal modes of vibrations present, however, not all the vibrations are Raman or infrared active. As a result, there are several materials which are either Raman or infrared inactive or both.^{136,137} Therefore, there are some selection rules which govern the ability of a normal mode to be detected by Raman or infrared spectroscopy. In any molecule, there could be some net dipole moment present as a result of polarized bonds or interaction with an electromagnetic radiation can create dipole moments by inducing polarization of the bonds. For example, Fig. 3-9 illustrates some simple schematics of chemical bonds where there is no net dipole moment present

at equilibrium position. However, when exposed to electromagnetic radiation, net dipole moments are induced depending on the type of bond stretching. During the symmetric stretching, the net dipole moment still remains zero, however, the asymmetric stretching induces a net dipole moment within the molecule. A vibration to be Raman active, polarizability of the molecule must change with vibrational motion. Similarly, a vibration to be IR active, there should be a net change in the dipole moment of the molecule during vibrations of bonds.

3.3.2.3 Photoluminescence

Similar to vibrational characteristics, materials can also be identified by their electronic structure i.e., the so-called energy gap or band gap. All the electrons from their constituent atoms in a material are not bound with the same energy and thus, several electronic states are available for the electrons leading to a band structure.¹³⁸ Now, at room-temperature, some of the electronic states are occupied (called bonding electronic states or molecular orbitals) where as rest of them (anti-bonding electronic states or molecular orbitals) remains empty. Energy gap between the highest occupied electronic state (or valence band) and the lowest unoccupied electronic state (conduction band) is called band gap which can be utilized for characterization of materials except metals and some other materials (e.g, graphite) which do not have any band gap due to overlap of valence and conduction bands.

In a simplified description, let us assume that the ground electronic level as the valence band where as the next higher electronic energy level as the conduction band, see Fig. 3-10. When a material is optically excited, photon(s) having higher energy than the band gap energy can be absorbed which will raise electron(s) from the valence band to the conduction band across the forbidden energy gap. Electrons will initially relax some of the

excess energy by nonradiative decay process and will come to rest at the lowest energy in the conduction band. Eventually, electrons will fall back down to the valence band and the energy difference (or band gap energy) will be emitted from the material as luminescent photons, see Fig. 3-10. Therefore, energy of the emitted photons is a direct measure of the band gap energy and this process of photon excitation followed by photon emission is called photoluminescence.

From the above discussion, it is clear that these spectroscopic techniques are not only useful for characterization of known materials but also they can identify new and unknown phase(s). Apart from the advantage of high spatial resolution, these methods essentially detect the vibrational and the electronic characteristics of any phase in any form, and therefore, are not only restricted to crystalline structure of materials but also applicable to amorphous forms. It has been well realized that the phase transformation in B_4C is a result of localized collapse of crystal structure to a disordered state.¹⁸ Also, it has been shown that the small collapsed regions do not have any crystallinity and therefore, they are referred as amorphous B_4C . However, previous Raman spectroscopic work^{71,131,132} has detected newer peaks which are not associated with crystalline B_4C . Therefore, it has been suggested that the a - B_4C is not necessarily a disordered state of B_4C , rather, it's a mixture of newer phase(s) resulted from structural destruction. Therefore, in the current work, apart from visible Raman spectroscopy, uv Raman, PL and FTIR spectroscopic techniques were also utilized which are ideal for detection of newer phases based on the chemical bonding and electronic structure characteristics. It was expected that these studies will shed more light on the disordered state of B_4C compared to only visible Raman spectroscopy.

3.3.3 Experimental

In the current work, damaged regions beneath the static and dynamic indentations on a polycrystalline B_4C , as discussed in section 3.2, were probed using (i) visible Raman (He-Ne laser, 632.8 nm, 1.96 eV), (ii) uv Raman (He-Cd laser, 325 nm, 3.80 eV), (iii) photoluminescence (He-Cd laser, 325 nm, 3.80 eV) and (iv) FTIR spectroscopy in a reflection mode under a microscope with a focusing diameter of $\sim 10 \mu m$, close to the diffraction limit of infrared wavelengths.

3.3.4 Results of Raman Spectroscopy

Figures 3-11 (A) and 3-11 (B) show the visible Raman spectra collected from the un-indented polished surface and damaged regions, created by static and dynamic indentations, of polycrystalline B_4C . Raman spectrum from the un-indented polished surface in the neighborhood of the indents is consistent with that reported in the literature for single crystal and polycrystalline boron carbide ceramics.^{132,134,135} The various peaks in the spectrum can be related to the crystal structure of boron carbide as follows. Boron carbide has a complex rhombohedral crystal structure containing eight icosahedrons and one linear chain of three atoms, see Fig. 3-12. Each icosahedron ($B_{11}C$) consists of 11 Boron (B) atoms and one Carbon (C) atom residing in one of the polar sites.^{71,132,134,135} The linear chain consists of CBC atoms. The icosahedrons are located at the corners of the unit cell and one of the longest diagonals along the $\langle 111 \rangle$ direction contains the linear chain. Origin of the two broad peaks in the lower frequency range (at 275 cm^{-1} and 325 cm^{-1}) is not well understood in the field although they often appear in B_4C ceramics.¹³⁴ The appearance of the next two narrow peaks (at 478 cm^{-1} and 532 cm^{-1}) have been assigned to the rotation of the CBC chain about an axis perpendicular to the $[111]$ direction and the librational mode of $B_{11}C$ icosahedron, respectively. Broad peaks in the high frequency

range (between 600-1200 cm^{-1}) are associated with the B_{11}C icosahedrons. Apart from these characteristic peaks, a small peak near 1580 cm^{-1} was observed in the Raman spectrum of the undamaged surface. This peak is attributed to the so-called G-peak (graphite peak),^{139,140} will be described in the following paragraph, due to the presence of free carbon in the boron carbide specimens.

Similar spectra were detected from the areas damaged by static indentation as shown in the middle curve in Fig. 3-11 (A) with a new disorder-induced (D) peak ($\sim 1335 \text{ cm}^{-1}$) as shown in the magnified view of these spectra in Fig. 3-11 (B). The G and D peaks represent zone center phonons of E_{2g} symmetry and K-point phonons of A_{1g} symmetry of graphitic C, respectively.^{139,140} While the G-peak is associated with in-plane bond-stretching motion of pairs of sp^2 -bonded C atoms present either in olefinic chains or in aromatic rings, the D-peak corresponds to the breathing mode only from the aromatic rings, see Fig. 3-13.

Significant changes are detected from the indented areas formed by dynamic indentation (top curve of Fig 3-11 (A)). Intense G and D peaks were detected at $\sim 1590 \text{ cm}^{-1}$ and at $\sim 1335 \text{ cm}^{-1}$, respectively, as shown in the top spectrum in Fig. 3-11 (A). The evolution of both D and G peaks in Raman spectra are due to the creation of free C-rich phase and thus is well accepted as the indication of localized amorphization in B_4C .^{71,131,132} The evolution of D-peak in the Raman spectra for both type of indentations clearly suggests the formation of sp^2 hybridized aromatic C rings within the indented areas. Also, the stronger G and D peaks induced by dynamic indentation suggests a higher level of structural damage or amorphization of the polycrystalline B_4C as compared to static indentation.² This interpretation is also associated with the lower Raman shift of the characteristic breathing modes of the icosahedral B_{11}C structures^{132,134,135} of crystalline

B₄C at ~1082 cm⁻¹ (for dynamic indentation) and at ~1089 cm⁻¹ (for static indentation) due to the strain induced by the amorphization.

More structural information can be obtained from the uv Raman spectra in Fig. 3-11 (C). Similar features like visible Raman spectra were observed in the uv Raman spectra. It is interesting to note that the two low frequency peaks of visible Raman spectra in the range from 250-350 cm⁻¹ did not appear in the uv Raman spectra. Our results suggest for the need of further investigation of B₄C using uv Raman spectroscopy. In addition, the relative intensity of the G-peak (I_G) is higher than the intensity of the D peak (I_D) for both type of indentations. An opposite trend was observed in the visible Raman spectra as shown in Fig. 3-11. The I_D/I_G ratio is ~0.6 for uv Raman and is ~1.1 for visible Raman. The I_D/I_G values and deviation of I_D/I_G observed here (i.e., dispersion) are similar to that detected from hydrogenated and non-hydrogenated a-C films with sp^2 -bonded C clusters.^{141,142} Also, D-peak disappears under uv excitation for disordered and nanocrystalline graphite but not for a-C.¹⁴² Apart from these, the diamond-like carbon films with pre-dominated sp^3 -bonded C usually have low I_D/I_G values (< 0.3) and low I_D/I_G dispersion (< 0.3). This also suggests that a low sp^3 hybridized C content in the a-C formed within the indented regions. Therefore, Raman spectroscopy confirmed the formation of sp^2 -bonded aromatic carbon clusters by static and dynamic indentations due to amorphization of B₄C.

Similar to visible Raman spectroscopy, the results of uv Raman spectroscopy also indicate that dynamic loading results in a greater level of C cluster formation. In addition, dispersion of G-peak to higher frequency was observed in the visible (Fig. 3-11 (A)) and uv Raman spectra (Fig. 3-11 (C)) collected from the dynamically indented region compared to the static indented region. It was concluded that the greater level of C-cluster formation

under dynamic indentation compared to static indentation causes the observed G-peak dispersion.^{142,143}

3.3.5 Results of Photoluminescence Spectroscopy

PL experiments were performed to further analyze the structures within the a-B₄C. Figure 3-14 presents the PL spectra of B₄C obtained from the un-indented surface and the indented regions of static and dynamic indentations. A weak PL band at 2.4 eV was detected from the un-indented surface (bottom curve and inset). This PL band is stronger for indented regions created by static indentation (middle curve) and strongest for areas damaged by dynamic indentation (top curve). A shoulder peak at ~2.05 eV was observed for the un-indented surface (shown clearly in the inset) and indented regions. Apart from these peaks, a new peak at ~3.05 eV was noted in the PL spectra from both type of indented regions. Similar to the 2.4 eV peak, this peak was also observed to be stronger under dynamic indentation compared to static indentation. PL band at ~2.05 eV is associated with the optical band gap of B₄C.¹⁴⁴ But the other two PL signals (at ~2.4 eV and ~3.05 eV) are well above the optical band gap of B₄C and therefore, are not associated with the crystalline B₄C structures. These PL bands are explained as the following. Amorphous carbon (a-C) and hydrogenated a-C (a-C:H) films have been observed to exhibit a broad PL band from ~1.8 eV to 3.7 eV.¹⁴⁵ These a-C films contain *sp*² - bonded carbon clusters embedded in the a-C matrix. Their band gaps depend on the size and distribution of the *sp*² clusters. Since Raman spectroscopy suggested that the indented areas formed by static and dynamic indentations contain a-C structures, we rationalize that the PL spectra detected here are attributed to radiative recombination mechanism of photo-excited electrons and holes in localized tail states within *sp*² clusters.¹⁴⁵ Similar to the Raman spectra, a stronger PL peak for dynamic indentation

compared to static indentation again indicates the presence of more aromatic sp^2 C-clusters within dynamically indented regions.

3.3.6 Results of Infrared Spectroscopy

Discussion so far has suggested the formation of sp^2 hybridized aromatic C clusters in the indented areas formed by static and dynamic indentations. However, these results did not provide any information about the existence of B-rich phase within the indented regions. Therefore, to further clarify the a - B_4C structure, FTIR spectra were collected from the un-indented surface and damaged regions of static and dynamic indentations. Spectra collected from all un-indented and indented areas are merely similar (except one to be discussed later), see Fig. 3-15. These spectra exhibited FTIR peaks characteristic of crystalline B_4C . The FTIR peak at $\sim 1100\text{ cm}^{-1}$ corresponds to the B-C stretching vibration.¹⁴⁶ As discussed before, B_4C crystal contains linear CBC chain along one of the body diagonals of the rhombohedral unit cell, see Fig. 3-12.^{71,132,134,135} The end C atoms of the chain have sp^3 -like hybridization whereas B exists presumably with an sp^2 -like hybridization.¹³⁵ The stretching of these CBC chains¹⁴⁴ is responsible for the peak around 1590 cm^{-1} . It could be observed from Fig. 3-15 that the intensities of these peaks gradually decrease in succession from the un-indented surface to static indentation to dynamic indentation. This trend clearly indicates structural distortion in B_4C during indentation as also suggested by Raman spectroscopy. Lower intensity of FTIR peaks from static indentation to dynamic indentation suggests a greater amorphization or structural disorder. The only difference occurred in the FTIR spectra corresponding to the dynamically indented region which exhibited a new IR absorption band between $\sim 760\text{-}830\text{ cm}^{-1}$ (shown clearly in the inset). This peak covers the known IR signals for free icosahedral B_{12} molecules.^{147,148} Due to the broad spectra distribution, we think that it is more appropriate

to assign this IR band to amorphous B-clusters, in consistent with a reported data.¹⁴⁸

Therefore, FTIR clearly suggests the formation of *a*-B clusters within the *a*-B₄C created by dynamic indentation. However, no such evidence was observed in the FTIR spectrum collected from the damaged region of static indentation.

The localized solid-state amorphization in B₄C is a shear driven phenomena.^{18,131} In ballistic impact experiments of B₄C, amorphization was observed only above certain impact velocities.¹⁸ On the other hand, similar phenomena was observed for nanoindentation,¹³¹ static indentation and dynamic indentation.⁷¹ In indentation experiments, the sharp edges of the indenter develop large shear stresses compared to impact experiments, and thus such stress state promotes amorphization. In addition to high shear stresses, the high strain rate during dynamic indentation further facilitates the amorphization compared to low strain rate static indentation as revealed by the above spectroscopic results. High strain rate-induced amorphization has also been predicted from MD simulations for metallic nanowires.¹⁴⁹

Finally, we present a schematic of the formation of *a*-C and *a*-B clusters. Amorphization of each B₄C unit cell (see Fig. 3-16 (A)), with eight B₁₁C icosahedrons at the corners, will cause the collapse of this structure into two carbon atoms, one boron atom, and a B₁₁C icosahedron per unit cell (Fig. 3-16 (B)). The possible mechanism could have been accompanied by the collapse of the B₁₁C icosahedron, which is energetically more stable to release the carbon atom and replace with a boron atom. This process will reorganize into one amorphous B₁₂ cluster, and one carbon atom that will form carbon clusters with adjacent carbon atoms (Fig. 3-16 (C)).

3.4 Conclusions

Fine-grained boron carbide ceramics were subjected to static and dynamic indentations to study the influence of strain rate on hardness and fracture toughness. The boron carbide ceramics showed a consistent decrease in hardness and fracture toughness as well as a greater extent of damage under dynamic indentations than under static indentations. Presence of residual porosity was observed to lower dynamic hardness significantly compared to static hardness. Similar to indentation studies on intact specimens, subsurface studies employing split specimens also revealed greater extent of damage under dynamic indentation compared to static indentation. Spectroscopic studies revealed greater structural disorder or phase transformation under dynamic loading compared to static loading. In depth analysis of from Raman and PL spectroscopy results revealed that a-C clusters were formed within the indented regions. Also, FTIR analysis reveals the existence of a-B clusters within the dynamically indented region.

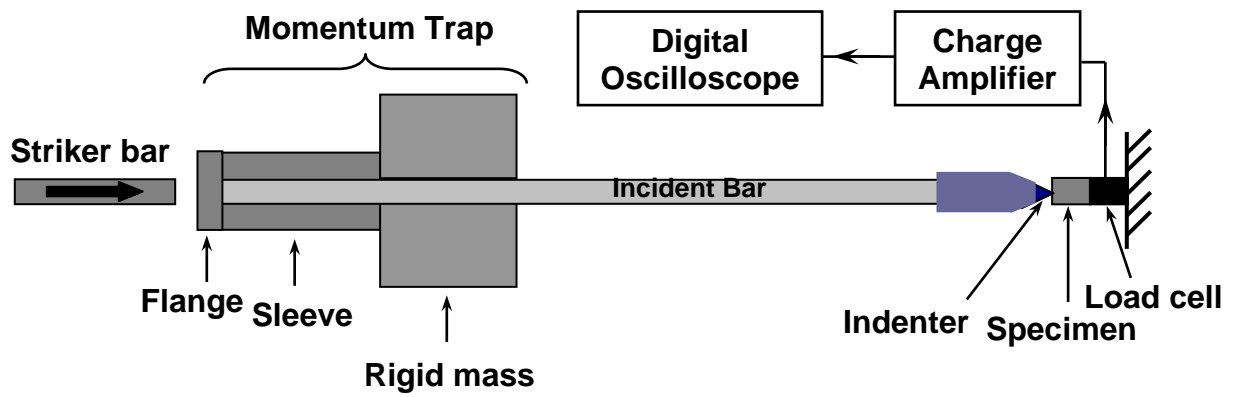


Figure 3-1. Schematic of experimental setup for dynamic indentation hardness measurements.

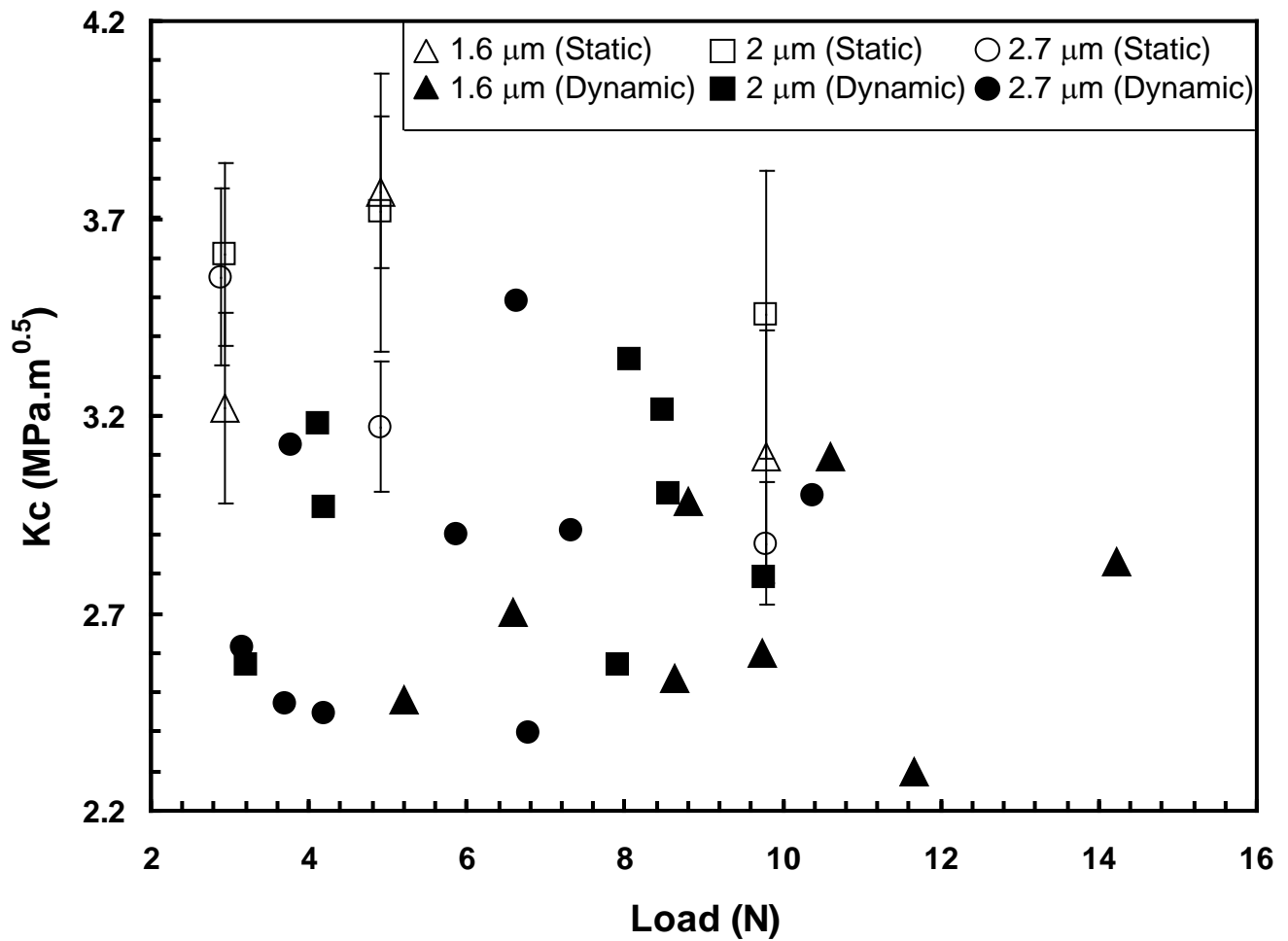


Figure 3-2. Comparison of static and dynamic hardness values for three grain sizes of B₄C.

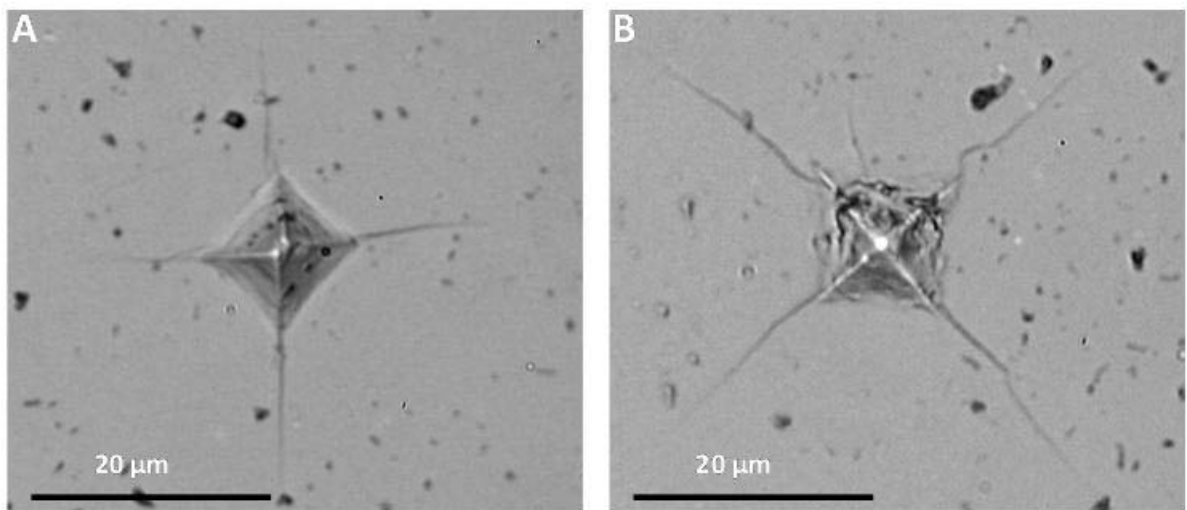


Figure 3-3. Optical micrographs of A) static and B) dynamic indents for 2.7 μm grain size B_4C at 300 gm. Note longer cracks and more severe damage in dynamic indent.

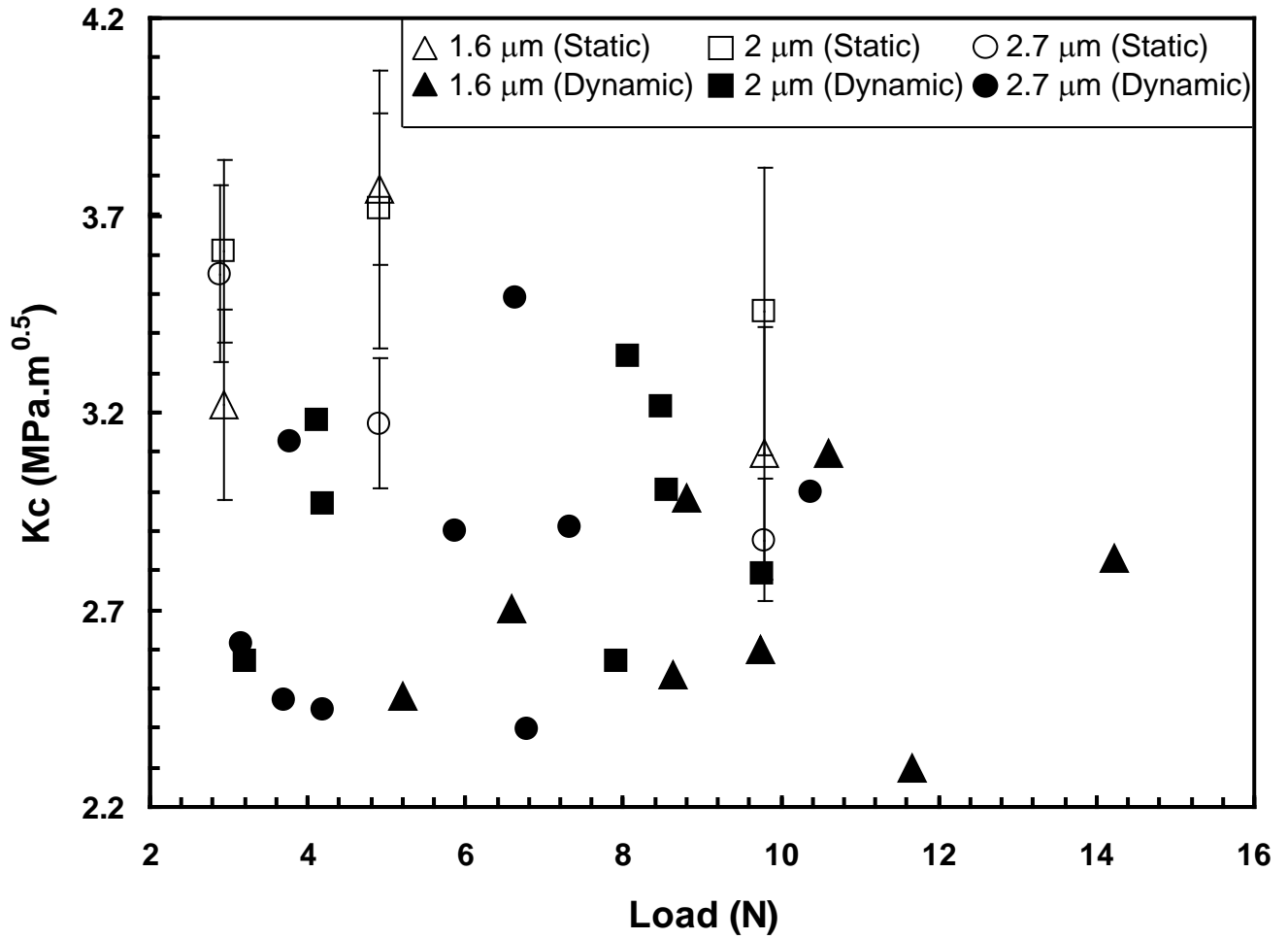


Figure 3-4. Comparison of static and dynamic indentation fracture toughness for three different grain sizes of boron carbide.

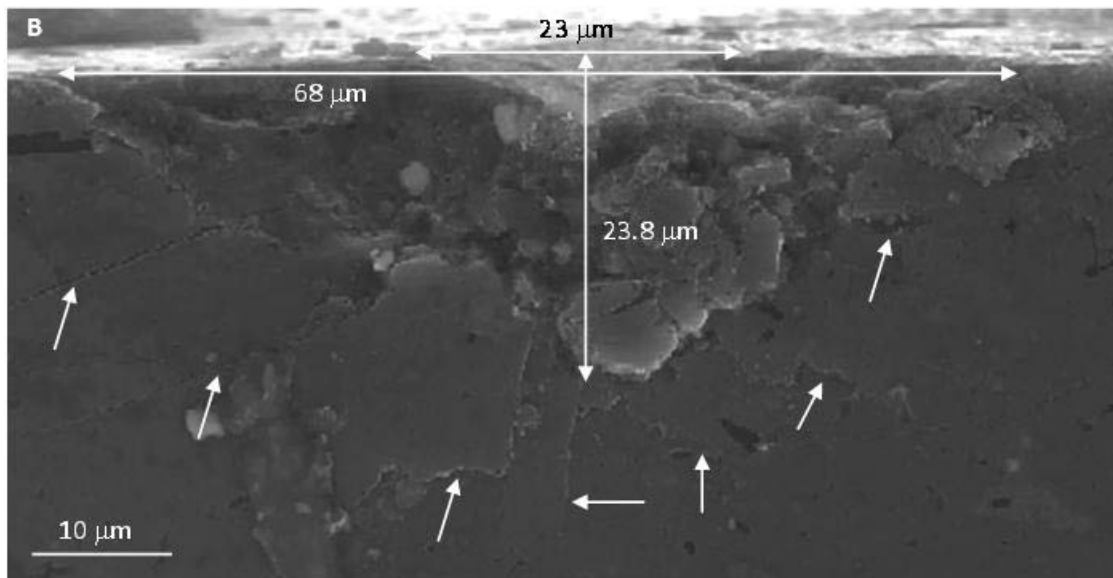
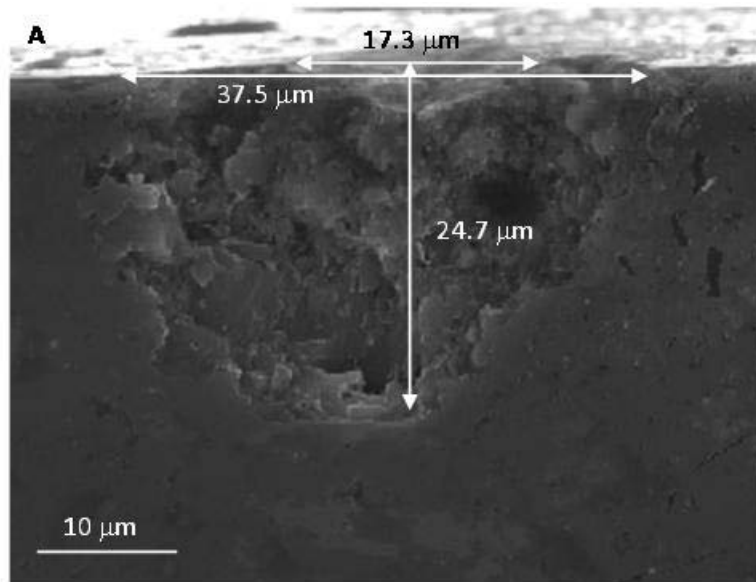


Figure 3-5. Subsurface damaged region beneath A) static indentation and B) dynamic indentation at a load of 19.6 N for 1.6 μm grain size boron carbide.

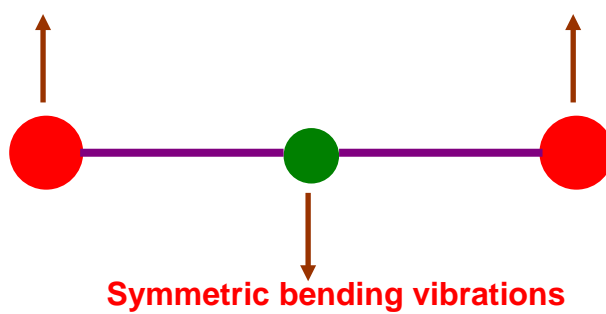
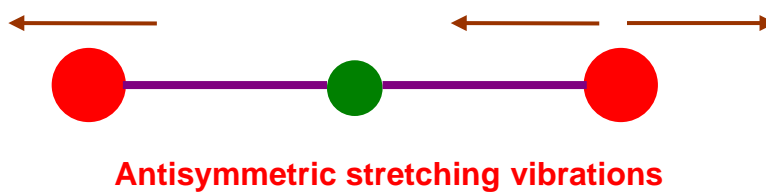
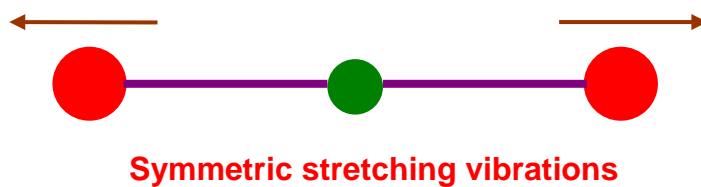


Figure 3-6. Different normal of mode of vibrations.

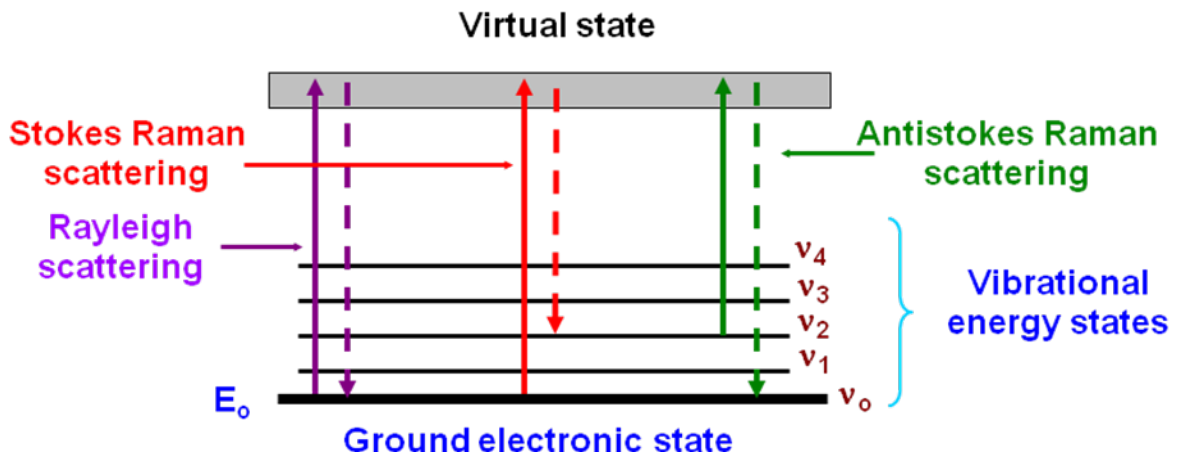


Figure 3-7. A simple schematic illustrating Rayleigh, Stokes and anti-Stokes Raman scattering phenomena.

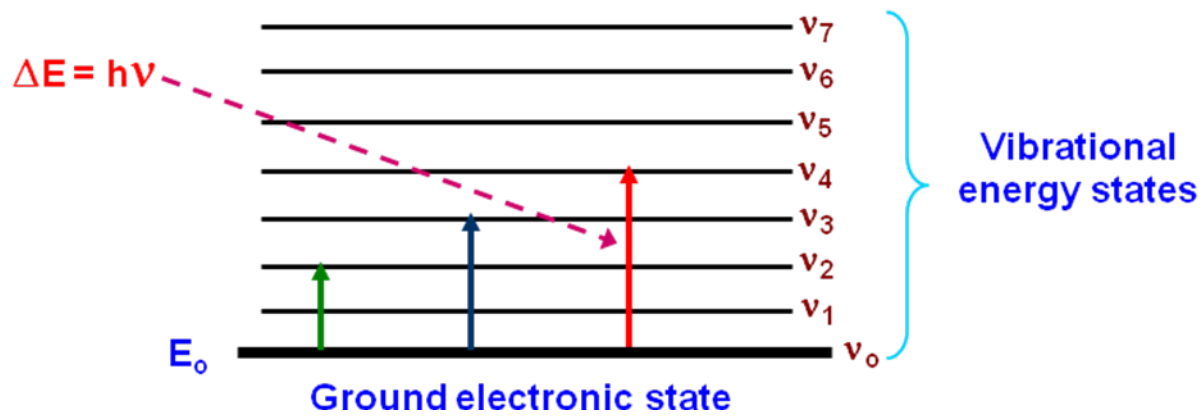


Figure 3-8. A schematic of the infrared absorption spectroscopy.

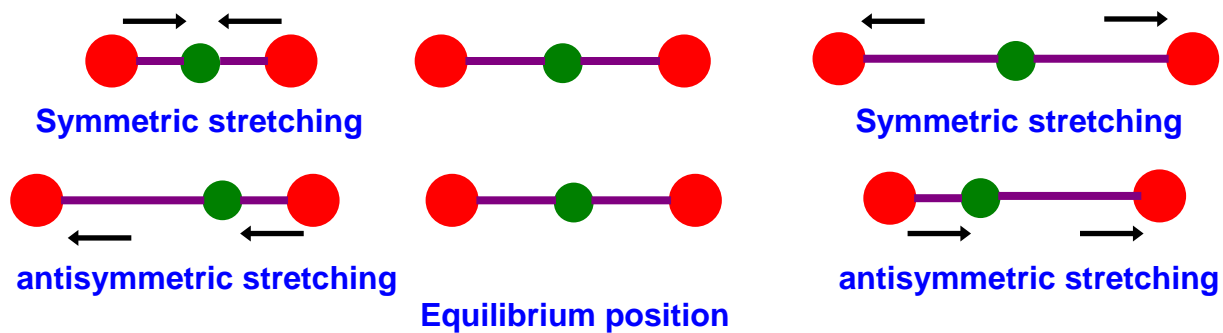


Figure 3-9. Changes in the net dipole moment of a molecule during asymmetric stretching.

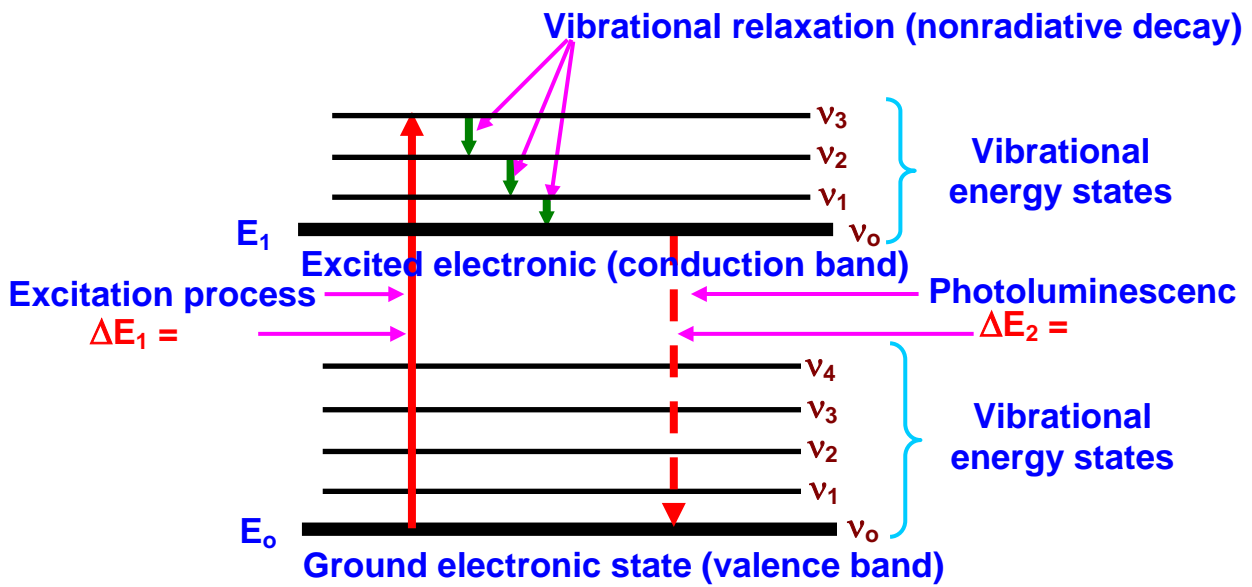


Figure 3-10. A schematic illustration of photoluminescence phenomenon.

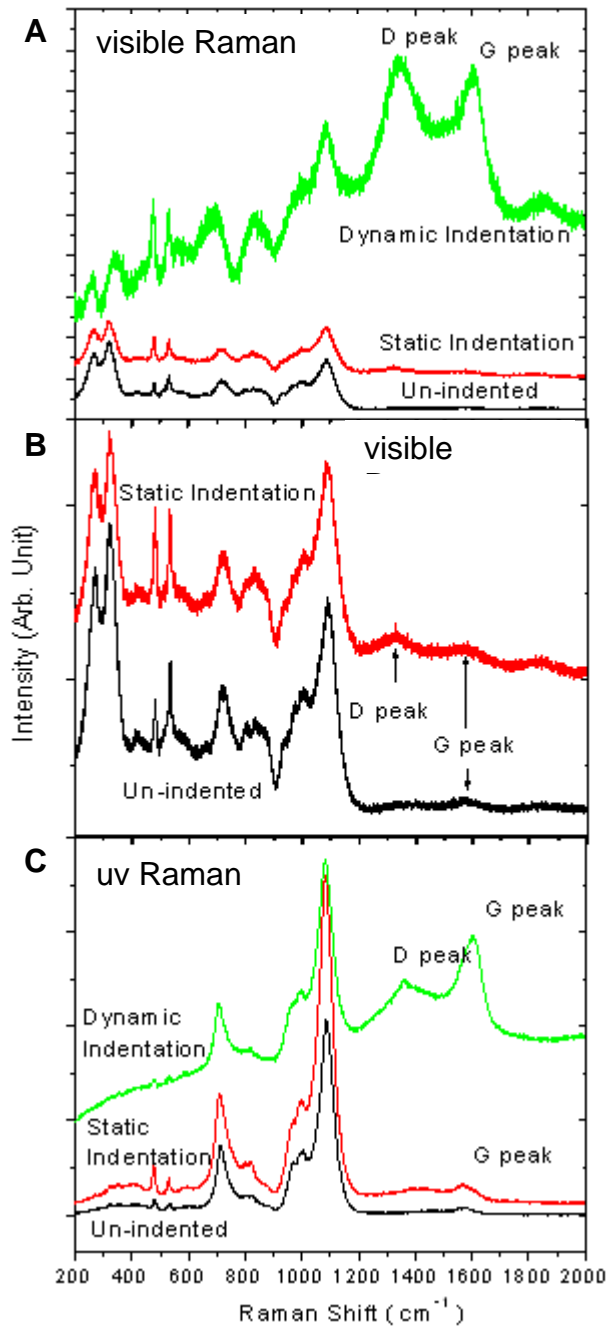


Figure 3-11. A) visible Raman spectra and C) uv Raman spectra from the un-indented surface and damaged regions beneath the static and dynamic indentations. B) Magnified view of two of the spectra in A.

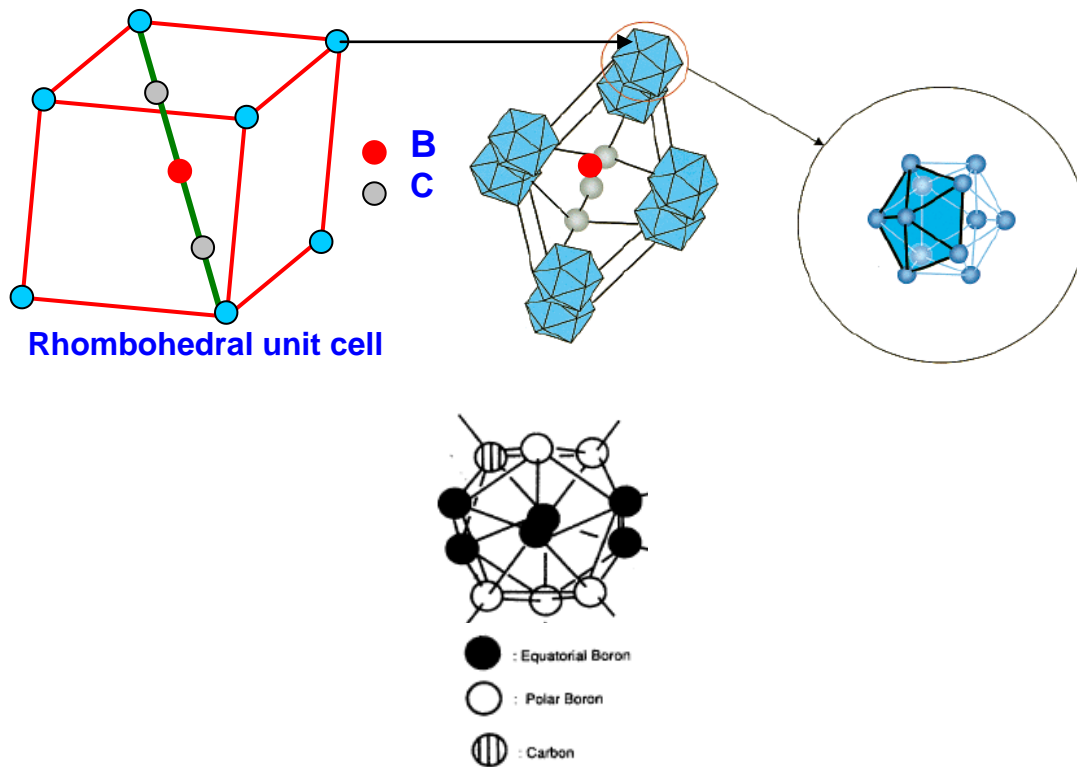


Figure 3-12. Crystal structure of boron carbide (B_4C).

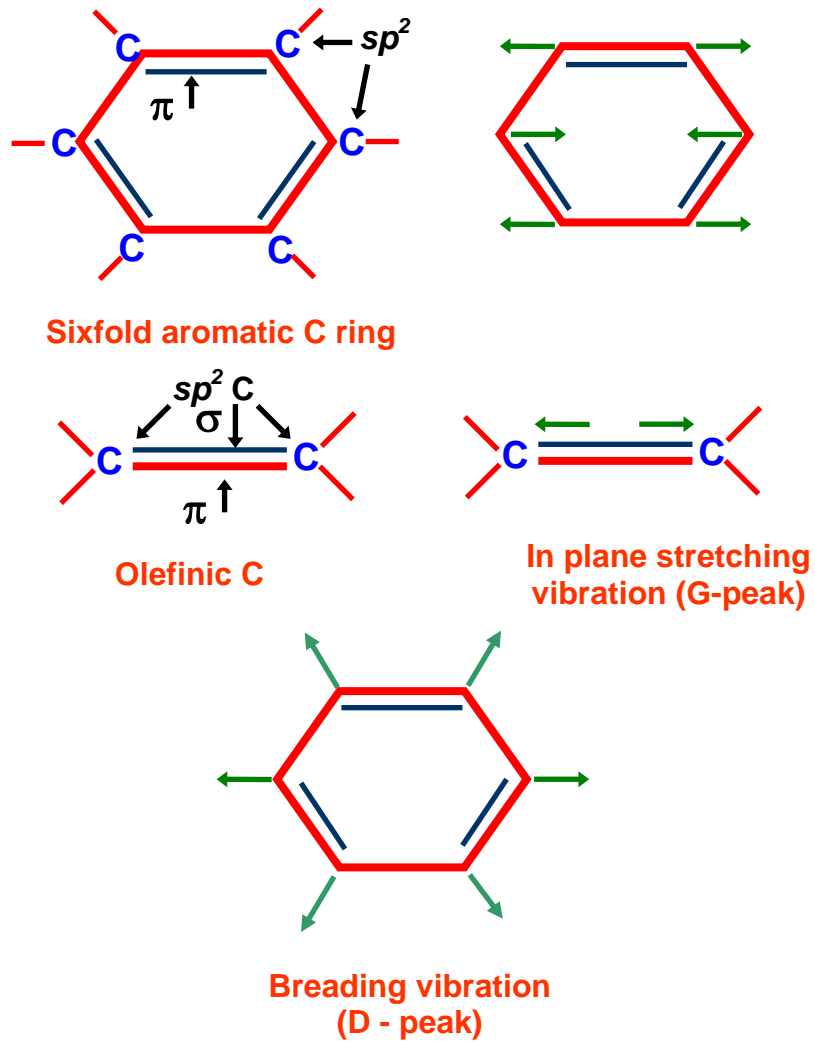


Figure 3-13. Origin of D-peak and G-peak.

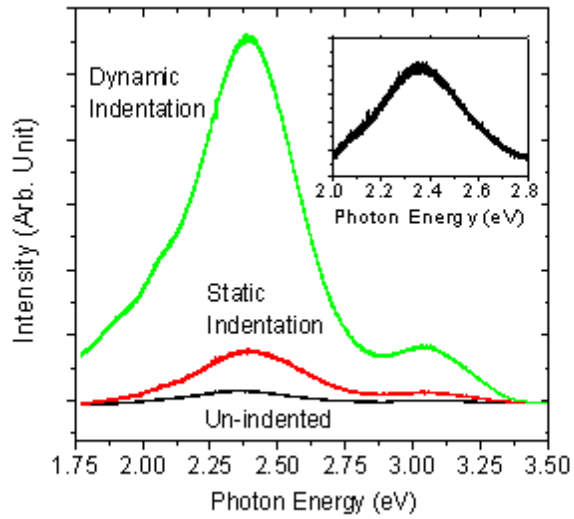


Figure 3-14. Photoluminescence from the un-indented surfaces and damaged regions beneath the static and dynamic indentations.

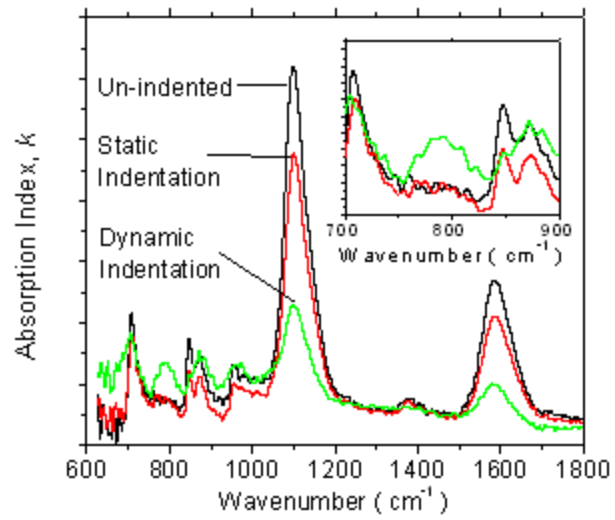


Figure 3-15. FTIR spectra from the un-indented surfaces and damaged regions beneath the static and dynamic indentations.

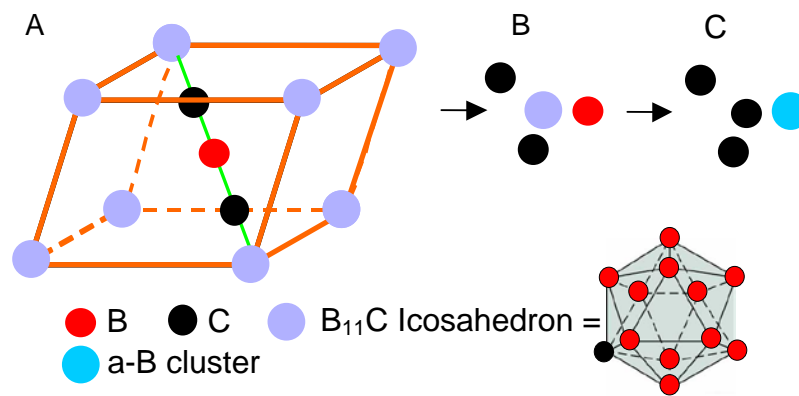


Figure 3-16. Schematic of A) a rhombohedral unit cell of B_4C with eight $B_{11}C$ icosahedrons at the corners. B) Amorphization of each unit cell will form two carbon and one boron atoms and a $B_{11}C$ icosahedron. C) One $B_{11}C$ icosahedron and one boron atom will reorganize into one amorphous boron (a-B) cluster, and a carbon atom that form carbon clusters with adjacent carbon.

Table 3-1. Comparison of average dynamic and static hardness and fracture toughness values

Grain size (μm)	HV_s (GPa)	HV_d (GPa)	% Change $\frac{(HV_s - HV_d)}{HV_s}$	K_C^s ($\text{MPa}\cdot\text{m}^{0.5}$)	K_C^d ($\text{MPa}\cdot\text{m}^{0.5}$)	% Change $\frac{(K_C^s - K_C^d)}{K_C^s}$
1.6	25.41 ± 1.00	18.17 ± 2.00	28.49	3.39 ± 0.25	2.69 ± 0.27	20.65
2.0	27.45 ± 2.00	26.15 ± 2.50	4.74	3.61 ± 0.30	3.00 ± 0.29	16.89
2.7	27.45 ± 2.50	23.37 ± 3.00	14.86	3.22 ± 0.16	2.81 ± 0.36	12.73

CHAPTER 4 SCRATCH-INDUCED DEFORMATION IN ZrB_2 -SiC COMPOSITE

4.1 Introduction

As mentioned in Chapter 1, during service, aerospace structural components such as heat-shields, nose cones, leading edges, engine cowl inlets, etc., are often subjected to abrasion-dominated wear scenarios (abrasive wear) due to the impact with atmospheric debris particles. As ultra high-temperature ceramics (UHTCs), in recent times, have been identified as the potential candidates for the aforementioned aerospace applications, it is, therefore, important to investigate their fundamental inelastic deformation mechanisms. Among the available ultra high-temperature ceramics, zirconium diboride-silicon carbide (ZrB_2 -SiC) composites have received significant attentions owing to their improved oxidation behavior compared to ZrB_2 ceramics. So far, most of the recent studies have been mainly focused on the processing and the oxidation behavior of the ZrB_2 -SiC composites.³⁷⁻⁴⁸ However, investigations on the evaluation of wear characteristics of UHTCs are limited. Similarly, studies on the fundamental deformation and fracture characteristics in polycrystalline ZrB_2 -SiC composites and other UHTCs are also not available.

Indentation and scratch experiments have been effectively used to model deformation and damage mechanisms that evolve in ceramics during an abrasion process. While the scratch experiments involve both normal and tangential point loads, indentation experiments only apply a normal point load on the surface. Therefore, in this dissertation, scratch experiments were preferred for investigation of complex contact interactions and were used for wear

characterization of a $\text{ZrB}_2\text{-5wt\%SiC}$ composite. Two types of experiments were conducted in the current investigation: (i) constant low-load and low-velocity and (ii) variable high-load and high-velocity scratches. The current dissertation mainly emphasizes on the results of low-velocity scratch experiments. The high-velocity scratch results have been discussed briefly.

During scratch process, materials beneath the scratch tool undergo elastic-plastic deformation. Directly beneath the indenter tool, a plastically deformed groove is formed which remains surrounded by the elastically deformed region. From experimental and theoretical studies, it has been shown that due to the strain-incompatibility between these two regions localized residual stresses are induced within the materials (will be discussed in more detail in section 4.3).¹⁵⁰⁻¹⁵² During the unloading phase, the accumulated deformation-induced residual stress causes lateral cracking. Initiation of such damage and consequent material removal from the surface due to these contact processes may result in lower mechanical reliability of the components made out of UHTCs. Therefore, quantification of mechanical residual stress due to scratch or abrasion phenomenon is necessary for a fundamental understanding of the material removal process and for design of abrasion-resistant materials. However, no such studies in the $\text{ZrB}_2\text{-SiC}$ composites, so far, are available in open literature. In the current investigation, micro-Raman spectroscopic technique has been utilized for the measurement of scratch-induced residual stress in the $\text{ZrB}_2\text{-SiC}$ composite.

Rest of the Chapter is divided in to two parts. The first part, section 4.2, is mainly focused on the low-load and low-velocity scratch studies along with some results of high-load and high-velocity scratch investigations. This section describes the microstructural features as a result of the scratch process which rationalized in the context of elastic stress field resulting from application of combined normal and tangential point loads. In section 4.3, results from the scratch-induced residual stress measurements, employing micro Raman spectroscopy, are discussed. This section describes the Raman spectroscopic measurements which are explained on the basis of sliding blister field model for residual elastic stress field. Since, zirconium diboride ceramic is extremely weak in Raman scattering (will be discussed latter in section 4.3), in the current investigation, the scratch-induced residual stress measurements were limited to the particulate phase (SiC) of the composite. The following discussion will start with the scratch studies in the ZrB_2 -5wt%SiC composite.

4.2 Scratch Studies

4.2.1 Experimental

4.2.1.1 Constant low-load and low-velocity scratches

The scratch studies were conducted in a ZrB_2 -5wt%SiC composite, processed via (P²C[®]) technique as discussed in Chapter 2. For scratch experiments, specimens of rectangular dimensions 6mm×3mm×4mm were cut from the rectangular slab of the processed composite using a low-speed diamond saw. One of the 6mm×3mm surfaces was first ground successively with 120, 240, 320, 400 and 600 grit silicon carbide for around 10 min each and then polished for 15 min using 6 μm diamond paste. A MTS nanoindenter[®] XPS

system was utilized to impart scratches on the polished surfaces at constant loads employing a Berkovich nanoindenter (tip radius ~ 100 nm) at a translational speed of 5 $\mu\text{m/s}$. Scratches of length 200 μm were conducted at five different constant loads of 50, 100, 150, 200 and 250 mN.⁷²

4.2.1.2 Variable high-load and high-velocity scratches

The high velocity (~500 mm/s) scratch experiments were conducted in a custom-built instrumented scratch tester.¹⁵³⁻¹⁵⁸ A schematic of the scratch tester has been shown in Fig. 4-1. The specimen was held on top of a high frequency (200 kHz) load cell which was housed in a rigid steel block. This load cell measures the normal force (thrust) during the scratch process. The indenter tool (a diamond conical indenter with 90° included angle) was held in a pendulum holder that was supported by two high-precision ball-bearing bushings housed in a rigid steel frame. A pneumatically driven piston was used to swing the pendulum and cause the diamond tip to transverse a path of circular arc, and create a scratch of variable depth on the specimen surface. Total scratch length and maximum depth-of-cut of each scratch can be varied by changing the length of the tool in the pendulum holder. The residual scratch tracks from both types of experiments were then investigated using a scanning electron microscope (using JEOL JSM-6400 and JEOL JSM-6335F) to reveal the resulting scratch-induced deformation and fracture patterns in the composite.

4.2.2 Results

4.2.2.1 Microstructural features of constant load low-velocity scratches

Figure 4.2 presents the typical constant low-load scratch patterns conducted at five different loads on the polished surfaces of the ZrB₂-5wt%SiC

composite (here after referred to as $\text{ZrB}_2\text{-SiC}$ composite).⁷² Traces of plastically deformed grooves with intact edges along the length were observed at all load levels. The width of the scratches increased with load. Scratches at 50 and 100 mN, see Figs. 4-2 (A) and 4-2 (B), were smooth and without any significant macroscopic damage. But as the load increased beyond 100 mN, damage (to be discussed in more detail later) was visible within the scratch grooves, see Figs. 4-2 (C)-4-2 (E). In Figs. 4-3 and 4-4, the residual scratch path and the corresponding scratch-length vs penetration-depth profiles are shown for loads of 50 mN and 250 mN, respectively. Magnified view of the small damaged regions along the scratch groove at 50 mN is also shown in Fig. 4-3. The fluctuations in the depth profiles, see Figs. 4-3 (A) and 4-4 (B), correspond to the regions where either grain pullout has occurred earlier during polishing or severe microscopic damage occurred ahead of the indenter tip during the scratch process. Clearly, greater fluctuations in the scratch-length vs penetration-depth profile for 250 mN correspond to greater extent of damage and material removal compared to that at 50 mN, as is evident from the comparison of Figs. 4-3 (A) and 4-4 (B). The increase in the penetration depth as the scratch load increased from 50 to 250 mN can be seen clearly from Fig. 4-5. In the following, the deformation mechanisms and the nature of damage that occurred along the scratch grooves at different load levels will be analyzed in more detail.

SEM micrographs in Fig. 4-6 show the deformation features developed within a scratch groove at a load of 250 mN. Figure 4-6 (A) reveals closely spaced parallel lines and microcracks within the ZrB_2 matrix and Fig. 4-6 (B)

shows a magnified view of region (A) revealing the above deformation features. Cracks emanating from both sides of a SiC particle are seen in Fig. 4-6 (B). The closely spaced parallel lines, indicative of plastic deformation during the scratch process, were also observed within the scratch grooves at other load levels. These plastic deformation line features are akin to 'slip line' patterns observed in ZrB₂ single crystal.¹⁵⁹ On the other hand, microcracks oriented almost normal to the scratch direction, were mainly observed at scratch loads greater than 100 mN. In Figs. 4-6 (A) and 4-6 (B), microcracks and slip line patterns were concentrated only on one side of the scratch either because of the asymmetrical orientation of the Berkovich indenter or due to slight inclination of the specimen with respect to the scratch plane. The material that is in contact with the sharp-edge of the indenter experiences more severe deformation compared to the material that is in contact with the flat surface (on the opposite side) of the indenter. Accordingly an asymmetry in the deformation pattern was observed on two sides of the scratch. Note that the closely spaced parallel lines (slip lines) within the scratch groove in Fig. 4-6 (B) were oriented at an angle to the scratch direction and occurred only in the ZrB₂ matrix phase. It is interesting to note that the slip line spacing and pattern were unaltered across any microcrack or across the cracks emanating from the SiC particle (shown in the white elliptical regions in Fig. 4-6 (B)). The cracks seem to slightly disturb only the continuity of the slip line patterns. Therefore, it is inferred that the slip lines must have formed before the microcracking during the scratch process. Figure 4-6 (C) reveals many sets of intersecting slip lines oriented randomly to the scratch direction. Slip lines were

present even well outside the scratch groove. Orthogonal microcracks were also seen at many other locations within the scratch groove where slip lines were absent, see Fig. 4-6 (C). The mechanistic rationale for the above sequence of formation of these slip lines and microcracks will be explored in the analytical modeling section.

Figure 4-7 (A) shows an image of one of the damaged regions along the scratch groove at a load of 250 mN. Several damage features such as ZrB₂ grain-boundary fracture, microcracks within the ZrB₂ grains and small scratch debris can be observed. Microcracks within a ZrB₂ grain and the small scratch debris (~ 1 μm) clearly indicate transgranular fracture within the ZrB₂ matrix. In Fig. 4-7 (B), microcracks originating from the ZrB₂-SiC interface as well as microcracks almost orthogonal to the scratch direction are seen. Figure 4-8 shows another region along the scratch groove at 250 mN where no slip bands were present but extensive microcracking normal to the scratch direction occurred within a single ZrB₂ grain. It is speculated that the origin of these microcracks is different from those seen in Figs. 4-6 and 4-7. Clearly, the material removal mechanisms within the scratch groove of the ZrB₂-SiC composite were a combination of transgranular and grain-boundary modes of fracture.

4.2.2.2 Microstructural features of variable load high-velocity scratches

Figures 4-9 (A)- (C) reveal a high velocity scratch path, extensive transgranular microcracks orthogonal to the scratch direction and the corresponding normal force vs. scratch length profile.¹⁶⁰ At the beginning of the

scratch path, the load is small which resulted in a smooth plastically deformed groove without any significant brittle damage. As the load increased, severe macroscopic brittle fracture features such as extended lateral cracking and material removal occurred in the middle of the scratch groove where the load was maximum. A closer view of the scratch groove revealed orthogonal transgranular microcracking and flattened debris, see Fig. 4-9 (B). Note that in the previous constant low-load (50-250 mN) and low-velocity (5 $\mu\text{m/s}$) scratch experiments were resulted in the formation of smooth plastically deformed grooves with occasional transgranular microcracking. In the variable high-velocity and high-load (8 N, maximum load) scratch experiments, the intensity of microcracking was significantly higher compared to previous scratch studies. Microstructural analysis of the regions containing lateral cracks also revealed the predominance of transgranular fracture in the composite. Similar to the low-velocity scratch experiments, microplasticity in terms of slip-line formation was also observed in these high velocity scratch grooves within the ZrB_2 phase, see Fig 4-10. However, a majority of the regions containing slip lines were probably removed due to extensive lateral cracking and the associated material removal. Thus, these studies revealed that during high velocity scratch process, extensive transgranular microcracking and severe lateral cracking caused significant damage and material removal in the composite. The force profile (Fig. 4-9 (C)) reveals that the load is minimum at the beginning and reaches maximum at the center of the scratches, and then again falls down to zero towards the exit end. Similarly, the scratch width is also minimum at both ends and maximum in the

middle. The fluctuations in the force vs. distance profile are attributed to the brittle cracking and the associated material removal during the scratch process.

It is interesting to note that plastic deformation features (slip-lines) were observed in a typical ceramic matrix composite. ZrB_2 has a hexagonal closed pack (hcp) crystal structure.^{2,159} In hcp structures, many slip systems have been observed to operate during plastic deformation.^{35,159,161-165} Slip occurs on basal $\{0001\}$, prismatic $\{10\bar{1}0\}$ and pyramidal $\{10\bar{1}1\}$ planes. ZrB_2 single crystals have been reported to undergo plastic deformation by prismatic slip during room temperature micro-indentation and basal slip during uniaxial high temperature experiments.¹⁵⁹ The observed line patterns within the ZrB_2 -SiC composite in this study were similar to the residual slip-line patterns observed in the above studies on ZrB_2 single crystals¹⁵⁹ as well as in materials with hexagonal symmetry.¹⁶⁵ Therefore, it is inferred that the observed deformation patterns in terms of closely spaced parallel lines within the scratch grooves of ZrB_2 -SiC composite, presented in Fig. 4-6 and Fig. 4-7, resulted from activation of slip mechanism during the scratch experiments. But the identification of particular slip systems that were activated during the scratch process in ZrB_2 requires more in-depth investigation using transmission electron microscopy (TEM) and was not pursued here. Note that these slip-lines were present only within the ZrB_2 matrix but did not extend into SiC particles. In general, it has been found that deformation induced defects in SiC particles consisted of stacking faults¹⁶⁶ which can only be discerned using TEM and other techniques. To our knowledge, the formation of slip-lines due to dislocation motion in SiC has not been reported.

4.2.3 Influence of Elastic Stress Field on the Scratch-induced Deformation

During a scratch event, the material beneath an indenter undergoes elastic-plastic deformation.^{150,151} In the current investigation, it was postulated that the observed transgranular microcracking orthogonal to the scratch direction within the ZrB₂ phase might have resulted from the tensile stress field. On the other hand, the shear stress component could cause the observed plastic deformation. In the following, we will utilize the elastic stress field solutions to rationalize the evolution sequence of slip-lines and microcracking in ZrB₂-SiC composite.

The single-pass scratch process has been well studied in the literature.¹⁵⁰⁻¹⁵⁸ It has been modeled as a sliding microindentation event where the point loads are applied simultaneously in normal (F_n) and tangential (F_t) directions on the surface of a specimen. Ahn *et al.*,¹⁵⁰ modeled the scratch process by superposition of Boussinesq field (due to F_n), Cerruti field (due to F_t)¹⁶⁷ and blister field solutions¹⁶⁸ to rationalize various crack systems that evolve during the scratch event. Recently, Jing *et al.*,¹⁵¹ utilized a wedge indentation model and estimated the plastic zone size as well as the damage zone size during a scratch process. Subhash *et al.*,¹⁵⁴ studied the influence of Boussinesq and Cerruti stress fields in the presence of a pre-existing microcrack and identified the most favorable orientation of cracks that activate during a scratch process. However, in all the above studies, the focus was always on crack activation in the wake of the scratch tip. The evolution of plastic deformation during the scratch process was never investigated. In our study, we have noticed both microcracks and slip

bands in the scratch groove. Therefore, we will focus on analyzing the stress components responsible for these inelastic features.

A schematic of the scratch process and the relevant stress fields are shown in Fig. 4-11. As the indenter moves forward on the specimen surface, it is assumed that a semi-cylindrical scratch groove of radius a is created which is surrounded by a semi-cylindrical inelastic zone of radius b as shown in Fig. 4-11 (B). The elastic stress field is now constructed from the superposition of the Boussinesq field and Cerruti field. The Boussinesq field arises due to the point normal load (F_n) and its components on a x - y plane at a depth $z = c$ below the surface are given by^{150,151,154,167}

$$\sigma_x^n = \frac{F_n}{2\pi c^2} \left[\frac{1-2\nu}{\bar{r}^2} \left\{ \left(1 - \frac{\bar{z}}{\bar{\rho}}\right) \frac{\bar{x}^2 - \bar{y}^2}{\bar{r}^2} + \frac{\bar{z} * \bar{y}^2}{\bar{\rho}^3} \right\} - \frac{3 * \bar{z} * \bar{x}^2}{\bar{\rho}^5} \right], \quad (4-1)$$

$$\sigma_y^n = \frac{F_n}{2\pi c^2} \left[\frac{1-2\nu}{\bar{r}^2} \left\{ \left(1 - \frac{\bar{z}}{\bar{\rho}}\right) \frac{\bar{y}^2 - \bar{x}^2}{\bar{r}^2} + \frac{\bar{z} * \bar{x}^2}{\bar{\rho}^3} \right\} - \frac{3\bar{z} * \bar{y}^2}{\bar{\rho}^5} \right], \quad (4-2)$$

and

$$\tau_{xy}^n = \frac{F_n}{2\pi c^2} \left[\frac{1-2\nu}{\bar{r}^2} \left\{ \left(1 - \frac{\bar{z}}{\bar{\rho}}\right) \frac{\bar{x} * \bar{y}}{\bar{r}^2} - \frac{\bar{x} * \bar{y} * \bar{z}}{\bar{\rho}^3} \right\} - \frac{3\bar{x} * \bar{y} * \bar{z}}{\bar{\rho}^5} \right]. \quad (4-3)$$

Similarly, the Cerruti field arises due to the point tangential load (F_t) and its components on the x - y plane at a depth $z = c$ below the surface are given by^{150,151,154,167}

$$\sigma_x^t = -\frac{F_t}{2\pi c^2} \left[\frac{3\bar{x}^3}{\bar{\rho}^5} - (1-2\nu) \left\{ \frac{\bar{x}}{\bar{\rho}^3} - \frac{3\bar{x}}{\bar{\rho}(\bar{\rho} + \bar{z})^2} + \frac{\bar{x}^3}{\bar{\rho}^3(\bar{\rho} + \bar{z})^2} + \frac{2\bar{x}^3}{\bar{\rho}^2(\bar{\rho} + \bar{z})^3} \right\} \right], \quad (4-4)$$

$$\sigma_y^t = -\frac{F_t}{2\pi c^2} \left[\frac{3\bar{x} * \bar{y}^2}{\bar{\rho}^5} - (1-2\nu) \left\{ \frac{\bar{x}}{\bar{\rho}^3} - \frac{\bar{x}}{\bar{\rho}(\bar{\rho} + \bar{z})^2} + \frac{\bar{x} * \bar{y}^2}{\bar{\rho}^3(\bar{\rho} + \bar{z})^2} + \frac{2\bar{x} * \bar{y}^2}{\bar{\rho}^2(\bar{\rho} + \bar{z})^3} \right\} \right], \quad (4-5)$$

and

$$\tau_{xy}^t = -\frac{F_t}{2\pi c^2} \left[\frac{3\bar{x}^2 * \bar{y}}{\bar{\rho}^5} + (1-2\nu) \left\{ \frac{\bar{y}}{\bar{\rho}(\bar{\rho} + \bar{z})^2} - \frac{\bar{x}^2 * \bar{y}}{\bar{\rho}^3(\bar{\rho} + \bar{z})^2} - \frac{2\bar{x}^2 * \bar{y}}{\bar{\rho}^2(\bar{\rho} + \bar{z})^3} \right\} \right]. \quad (4-6)$$

where σ and τ are the normal and the shear stress components and the superscripts n and t refer to the normal and tangential load directions. The Poisson's ratio is denoted by ν and the normalized variables \bar{x} , \bar{y} , \bar{z} , $\bar{\rho}$ and \bar{r} are defined as

$$\bar{x} = \frac{x}{c}, \quad \bar{y} = \frac{y}{c}, \quad \bar{z} = \frac{z}{c} = 1, \quad \bar{\rho} = \frac{\rho}{c} \quad \text{and} \quad \bar{r} = \frac{r}{c} \quad (4-7)$$

Also, $r^2 = x^2 + y^2$ and $\rho^2 = x^2 + y^2 + z^2$ define the distance from the point load to the field point in the x-y plane and the total distance, respectively.

Furthermore, F_n and F_t are related by

$$F_t = kF_n \quad (4-8)$$

where 'k' is defined as the friction coefficient or as a proportionality constant between normal and tangential point loads.^{150,151} Now the total normal (σ_x and σ_y) and shear stress (τ_{xy}) components due to the combined Boussinesq and Cerruti fields can be expressed as

$$\sigma_x = \sigma_x^n + \sigma_x^t, \quad \sigma_y = \sigma_y^n + \sigma_y^t \quad \text{and} \quad \tau_{xy} = \tau_{xy}^n + \tau_{xy}^t. \quad (4-9)$$

To rationalize the observed microcracking and plastic deformation patterns in our study, the maximum principal stress component (σ_1) and the

maximum shear stress component (τ_{\max}) have been computed from σ_x , σ_y and τ_{xy} . Our intent was to identify the regions with high tensile stress and high shear stress where microcracking and plastic deformation, respectively, can occur during a scratch process. In Fig. 4-11, along with a schematic of a scratch event, the distribution of the normalized maximum principal stress component, $\bar{\sigma}_1 = 2\sigma_1\pi c^2 / F_n$, and the normalized maximum shear stress component, $\bar{\tau}_{\max} = 2\tau_{\max}\pi c^2 / F_n$, see Figs. 4-11 (A) and 4.11 (C), respectively, on the $\bar{x} - \bar{y}$ plane in the vicinity of the indenter tip are presented. For clarity, the 2-D distributions of the stress components along the \bar{x} - axis for various 'k' values are presented in Fig. 4-12. The distribution of $\bar{\sigma}_1$ as shown on the $\bar{x} - \bar{y}$ plane (see Fig. 4-11 (A)) as well as along the \bar{x} - direction (see Fig. 4-12 (A)) indicate a stress singularity at the indenter tip. When $k = 0$, there is no tangential force component and the stress distribution is symmetric about the indenter position ($\bar{x} = 0, \bar{y} = 0$). For $k > 0$, large tensile principal stress develops in the wake of the indenter tip and its amplitude increases with 'k' as shown in Fig. 4-12 (A). Assuming that the maximum principal stress criterion is appropriate for mode-I crack propagation in brittle materials, a crack initiates when the maximum principal stress exceeds the fracture stress of the material and mode-I cracks open up orthogonal to the direction of maximum principal tensile stress. In the experiments, the magnitude of the maximum principal stress component was not large enough at lower scratch loads (e.g., ~ 50 mN) to cause significant microcracking. But as the load increased, a greater extent of microcracking was

observed as a result of the increased maximum tensile principal stress in the wake of the indenter. These observations are rationalized on the basis of increased tensile stress in the wake of the indenter with increasing 'k' as shown in Fig. 4-12 (A). The orientation of the principal tensile stress in the wake of the indenter, shown in Fig. 4-11 (D), causes the crack to open perpendicular to the scratch direction as shown in Figs. 4-6 – 4-9.

To explain the formation of slip-lines, we focus on maximum shear stress distribution during the scratch process. Figure 4-11 (C) shows the maximum shear stress distribution in the vicinity of the indenter tip. Note that the amplitude of τ_{\max} is symmetric about the \bar{x} - axis and highest in the regions ahead of the indenter position and slightly away from the \bar{x} - axis. The projected locations of the highest maximum shear stress and the maximum tensile principal stress on the scratch plane are shown at the bottom of Fig. 4-11 (C). The distribution of normalized maximum shear stress along the \bar{x} - direction is plotted for various values of 'k' at $\bar{y} = 0$ in Fig. 4-12 (B) and at $\bar{y} = \pm 0.5$ in Fig. 4-12 (C). These 2-D plots clearly reveal that the maximum shear stress, ahead of the indenter tip, increases with increasing 'k', similar to the normalized principal stress. Also, note that the maximum amplitude of τ_{\max} occurs not along x - axis but slightly away from the axis at $\bar{y} = \pm 0.5$. Depending on the intensity of loading (i.e., for large 'k'), the maximum shear stress can extend beyond the scratch groove resulting in slip-line formation outside the scratch grooves as seen in Fig. 4-6 (C) and Fig. 4-13. We postulate that the slip bands originate in these regions due to this high local shear stress during the scratch process. To validate this postulation, the

region near the exit-end of each of the scratches was observed in SEM. Recall that this end-region was never in the wake of the scratch tool and thus, was never subjected to high tensile stress shown in Fig. 4-11 (A) and Fig. 4-12 (A). On the other hand, this region must have experienced large τ_{\max} because this end-region was ahead of the indenter, see Fig. 4-11 (C) and Figs. 4-12 (B) and 4-12 (C). Therefore, only slip-lines are expected in this region. Figure 4-13 shows a SEM micrograph of a scratch-end revealing only slip-lines present on both sides of the scratch in this region. This observation clearly confirms that slip bands are indeed formed ahead of the scratch tool due to the occurrence of maximum shear stress.

Therefore, it is concluded that slip bands initiate in the regions ahead of the indenter tip during the scratch process and then the same region will experience tensile stress in the direction of scratch after the indenter moves away (in the wake). This will cause microcracks to open up orthogonal to the scratch direction as observed in Figs. 4-6 – 4-8. The present mechanistic study confirmed the sequence of formation of slip bands and microcracking which is in agreement with the experimental observations.

4.2.4 Discussion

In the current investigation on the $\text{ZrB}_2\text{-SiC}$ composite, two kinds of transgranular microcracks were observed in the ZrB_2 matrix; (i) within the slip bands, see Figs. 4-6 (A-B) and Fig. 4-7 (B), and (ii) in regions where no slip bands were observed, see Fig. 4-6 (C), Fig. 4-7 (A) and Fig. 4-8. It is believed that the sources for occurrence of these microcracks are different. In brittle

materials, defects can be categorized to two types; (i) processing-induced (inherent) flaws and (ii) deformation-induced defects. As the nomenclature indicates, the former are inherent in the microstructure of the ceramic materials (once ceramics are processed) and the latter result from the mechanical loading. Processing-induced defects include inter- and intra-granular microcracks, grain-boundary phases such as sintering aids, inhomogeneous grain size distribution, triple-point junctions, pores, agglomerates, impurities and weak interfaces along the second phase particles, etc. These defects are also referred to as 'strength limiting' flaws. On the other hand, mechanical deformation-induced defects include dislocations, twins, stacking faults, and regions of phase transformation and localized amorphization, etc. While the number of processing-induced defects remains constant in a given ceramic, the number of deformation induced defects continues to grow with the severity of deformation. Brittle materials, in general, show limited plasticity (i.e., microplasticity) due to limited number of favorable slip systems and low dislocation mobility.^{169,170} As a result, as soon as plasticity initiates, stress concentration occurs at dislocation pile-ups which can lead to microcracking to relieve the stress. On the other hand, processing-induced microcracking most commonly occurs as a result of differential thermal expansion between the grains of same phase or multi-phase materials.¹⁷¹

In ZrB₂-SiC composite, thermal residual stress arises because of thermal expansion anisotropy within ZrB₂ grains and due to difference in thermal expansion coefficients between ZrB₂ and SiC phases.² It is believed that the microcracks, facilitated by the tensile stress in the wake of the indenter and in

regions where slip bands did not develop, might have originated from the processing-induced defects to relieve the thermal residual stress (e.g., Fig. 4-8). On the other hand, the microcracks inside the slip bands are believed to have originated from the deformation-induced defects to relieve the stress associated with low dislocation mobility in the composite (e.g., Figs. 4-6 (A) and 4-6 (B) and Fig. 4-7 (B)). It is well-known that microcracking is the preferred mode of deformation in the absence of either well-defined slip systems or low dislocation mobility.^{169,170} Thus, microcracks outside the slip bands progress easily with further application of load and cause fragmentation as seen in Fig. 4-7 (A). However, such fragmentation or debris formation was not witnessed in the regions containing microcracks within slip bands.

Apart from microcracking, the high-velocity scratch experiments caused lateral crack evolution and significant material removal in the composite which was almost absent in low-velocity scratches, see Fig. 4-2 and Fig. 4-9 (A). As mentioned before, numerous experimental and theoretical investigations have shown that the loading phase of scratch process causes elastic-plastic deformation within a brittle material. Therefore, upon unloading residual stress is generated within the material. It has been well-known that scratch-induced residual stress component perpendicular to the scratch surface causes lateral cracking (will be discussed in detail in next chapter).¹⁵⁰ In Fig. 4-2, subsurface lateral crack growth within a constant load scratch groove at 250 mN can be observed. However, due to the low-load level used in these experiments, extension of the lateral crack up to the top surface was limited. During high

velocity scratches, the applied scratch load was significantly higher and resulted in extensive lateral cracking as seen in Fig. 4-9 (A).

The above mechanistic rationale for slip-line formation and microcracking in ZrB₂-SiC composite is also consistent with the well-known stick-slip mechanism studied in sliding interactions.¹⁷²⁻¹⁷⁸ The stick-slip mechanism arises from the changes in the frictional force during sliding contact due to the difference in static and kinetic friction coefficients. During a scratch process, pile-up of material ahead of the indenter-tip resists its motion and as a result, the indenter momentarily sticks to the material (or its motion is temporarily halted) resulting in an increased frictional force.^{152,172-178} This leads to an increased static friction coefficient and hence a greater force is required to overcome this resistance. Once the tangential force is large enough to overcome this frictional resistance, the indenter slips and moves forward. Thus the frictional force (or kinetic friction coefficient) is now decreased. This stick-slip mechanism continues during the scratch process which is reflected in the saw-tooth behavior of the frictional force as has been observed for several materials.^{176,178} During the stick-period, although the indenter motion is temporarily halted, the indenter continuously pushes the material piled-up ahead of it causing the material to deform first elastically and then plastically.^{152,156,158,177} Atomistic-scale investigations using MD simulations have predicted dislocation generation in the pile-up regions.^{177,179-181}

As discussed in the previous section, the analytical model clearly revealed that large shear stress develops just ahead of the indenter during sliding motion

(Fig. 4-11, Figs. 4-12 (B) and 4-12 (C)) and leads to plastic deformation in ZrB₂-SiC composite as was confirmed by the experimental observations (Fig. 4-13). Although friction coefficient measurements during the scratch process were not considered in the current investigation, we argue that pile-up of material may occur in the ZrB₂-SiC composite and large shear stress builds up in this region. Also, at a constant scratch load, the frictional force (and hence the friction coefficient) will increase due to the pile-up and as a result the induced shear stress will also increase as shown in Figs. 4-12 (B) and 4-12 (C). Eventually, the shear stress is relieved by the slip mechanism (dislocation generation) and the formation of slip-lines occurs within the ZrB₂ phase as shown in Figs. 4-6 and 4-7 (B).

The changes in frictional coefficient may also influence the microcracking observed within the ZrB₂ phase, see Figs. 4-6 – 4-8. If the stick-slip mechanism occurs during the scratch process, then the increase in friction coefficient (when the indenter is temporarily halted) will also increase the magnitude of maximum principal tensile stress behind the indenter (see Fig. 4-12 (A)) which can lead to greater microcracking orthogonal to the scratch direction.

The above investigation reveals that the ZrB₂-SiC UHTC can accommodate moderate ductility through initiation of slip bands at room temperature. This effect, in turn, can result in higher fracture toughness compared to traditional brittle ceramics. In pure ZrB₂, the fracture toughness² has been observed to be around 3.5-4.2 MPa.m^{1/2}. In typical brittle ceramic materials such as boron carbide (B₄C) fracture toughness⁷¹ values are lower than 3 MPa.m^{1/2}. The higher

fracture toughness in ZrB₂ ceramics can be a result of moderate ductility as observed in the current study. To investigate ductility in UHTC ceramics, future studies on the analysis of deformation behavior under elevated temperature are required. Such studies are expected to provide more insight on the deformation behavior these materials experience under more realistic operating environments.

4.3 Residual Stress Measurement within SiC Grains in ZrB₂-SiC Composite

4.3.1 Micro-Raman Spectroscopy

Raman spectroscopy has emerged as a useful nondestructive tool for residual stress measurements. The sensitivity of a Raman peak to mechanical stress (or more precisely the strain) was first reported by Anastassakis *et al.*¹⁸² In particular, micro-Raman spectroscopy (MRS) is useful in determining local residual stress due to its high spatial resolution (of the order of 1 μm).¹⁸²⁻¹⁸⁹ For example, in thin films and MEMS devices, micro-Raman spectroscopy is largely used for residual stress determination that arises as a result of coefficient of thermal expansion (CTE) mismatch between the substrate and the film materials.^{183,185,188,189} Indentation- and scratch-induced residual stress analyses have also been conducted using micro-Raman spectroscopy.^{186,187} In crystalline materials, the atomic vibrational frequencies depend on the interatomic force constants.¹⁸⁸ In strain-free crystalline materials, interatomic force constants as well as the vibrational frequencies correspond to the equilibrium atomic spacing. Residual stress resulting from either thermal process (such as sintering) or mechanical deformation (such as indentation, scratch, etc.) causes a definitive residual strain which in turn changes the equilibrium atomic spacing within a

material and thus the interatomic force constants. As a result, Raman scattering wave numbers are also perturbed. Depending upon the tensile or compressive nature of the residual stress, bond lengths and force constants either increase or decrease compared to the equilibrium values. Accordingly, a Raman peak shifts to lower or higher frequency for tensile or compressive residual stress, respectively,^{182,183,188,189} though there is no unique general relationship between the Raman spectrum parameters (particularly the wave number shift) and the residual stress-state.

One way to establish such relationships is the calibration procedure which correlates Raman peak shift in a material with the known applied stress. Then using the calibration curve, unknown residual stresses can be determined from the changes in Raman peak positions for that particular material. However, the resultant calibration curve also depends on the applied stress-state and therefore, there is no unique relationship between residual stress and Raman peak shift for a given material. On the other hand, explicit expressions relating Raman peak shift and residual stress have been derived for simple situations such as uniaxial stress-state, hydrostatic or equi-biaxial stress-state which can also approximate the residual stresses in materials.^{183,188,190} Therefore, expressions for appropriate scenario must be developed to estimate residual stress within Raman active materials utilizing micro-Raman spectroscopy.

Raman spectrum of ZrB_2 ceramics is not available in open literature, however, the current investigation has revealed that ZrB_2 is extremely weak Raman active. On the other hand, SiC is known to be strong Raman active and

its characteristic Raman peaks, particularly for cubic SiC, are highly sensitive to the residual stress.¹⁹⁰⁻¹⁹² Therefore, it is possible to determine the magnitude of the residual stresses from the stress/strain sensitive Raman peaks of SiC material. In this dissertation, changes in Raman peak positions of SiC grains, located within the scratch grooves of the ZrB₂-5wt%SiC composite, have been measured as a function of the scratch load. Then, from these Raman spectroscopic measurements, a mechanics based expression has been derived to estimate scratch-induced mechanical residual stress within the SiC grains in the composite.

4.3.2 Experimental

In the current study, a micro-Raman spectrometer, Renishaw[®] inVia Raman Microscope, was utilized for scratch-induced residual stress measurements. The Raman spectrometer consisted of a Si-laser (532 nm) to excite the specimen, a single spectrograph fitted with holographic notch filters, and an optical microscope (a Leica[®] microscope with a motorized XYZ mapping stage) rigidly mounted and optically coupled to the spectrograph. The spectrometer was initially calibrated with a Si standard using a Si band position at 520.3 cm⁻¹. A 100× objective lens was used to focus the incident beam on the desired SiC grains and to collect the scattered beam from the specimen. The spot size of the incident beam on the specimen was in between 1-1.5 μm. A maximum 25 mW of the laser power was used. Raman spectra were collected from several SiC grains located within the scratch grooves present in the ZrB₂-5wt%SiC composite. For comparison purposes, Raman spectra were also collected from

several SiC grains located outside the scratch grooves. All the Raman measurements were performed at room temperature.

4.3.3 Results of Micro-Raman Spectroscopy

Figure 4-14 reveals Raman spectra collected from the ZrB₂ and the SiC phases of the composite. It can be clearly seen that the Raman peaks from ZrB₂ phase were significantly weaker compared to the Raman peaks from SiC grains. Therefore, the Raman peaks from ZrB₂ were not further utilized in the current study for residual stress measurements. Fig. 4-15 shows the Raman spectra collected from the SiC grains located outside the groove and within the scratch grooves resulting from constant loads at 50, 150 and 250 mN. The Raman spectrum from SiC grains outside the scratch groove as shown in Fig. 4-15 is typical of 3C-SiC¹⁹⁰⁻¹⁹² which consists of one transverse optical (TO) peak at 796 cm⁻¹ and one longitudinal optical (LO) phonon peak at 972 cm⁻¹. These two peak positions have been consistently reported for many annealed 3C-SiC thin films and thus can be adopted to correspond to Raman peaks in stress-free 3C-SiC.¹⁹⁰⁻¹⁹² However, in the current study, SiC grains away from the scratch grooves showed both the TO- and LO-peaks at higher wave numbers (around 802.3 cm⁻¹ and 978.9 cm⁻¹, respectively) compared to stress-free 3C-SiC. Therefore, it was inferred that compressive residual stress is present within these SiC grains in the as-processed composite. The origin of compressive residual stress within the as-processed composite is due to the mismatch in Young's moduli (E) and CTE (α) between $H\text{-ZrB}_2$ ($E = 489 \text{ GPa}$, $\alpha_{avg} \sim 5.9 \times 10^{-6} \text{ K}^{-1}$)² and 3C-SiC ($E = 694 \text{ GPa}$, $\alpha \sim 3.5 \times 10^{-6} \text{ K}^{-1}$),^{193,194} as well as the difference between

room temperature (25°C) and sintering temperature (1750°C) of the composite. Because the CTE of polycrystalline ZrB₂ is greater than that of 3C-SiC, cooling of the consolidated compact from sintering temperature will result in compressive residual stresses within SiC grains.

With increasing scratch load, both the TO- and LO-peaks in the Raman spectra collected from the SiC grains within the scratch grooves progressively shifted to lower wave numbers compared to the Raman spectra collected from the SiC away from the scratches, see Fig. 4-15. With increasing scratch load, greater peak widening as well as asymmetry in peaks can be seen in these spectra. Raman peak shift to lower wave numbers indicates development of tensile residual stress in these SiC grains. The magnitude of the peak shift (and hence tensile residual stress) increased with scratch load. Figure 4-16 (A) shows the measured LO- and TO-peak positions for scratch loads of 50, 100, 150 and 250 mN and Fig. 4-16 (B) shows the shift in TO-peak and LO-peak positions compared to the same peaks in stress-free 3C-SiC materials (796 cm⁻¹ for TO-peak and 972 cm⁻¹ for LO-peak). At 50 mN scratch load, both the TO-peak and LO-peak were lower than the stress-free position indicating the presence of compressive residual stress in SiC grains. As the scratch load increased beyond 50 mN, both the peaks further shifted to lower wave numbers indicating development of a tensile stress state within these grains. In SiC grains, present within the scratch grooves, the total residual stress-state (σ^R) is the sum of processing-induced thermal residual stress (σ_t^R) and scratch-induced mechanical residual stress (σ_s^R), i.e.,

$$\sigma^R = \sigma_t^R + \sigma_s^R. \quad (4-10)$$

Now, in the SiC grains that exist within the unscratched regions of the composite, $\sigma^R = \sigma_t^R$ which is compressive as indicated by the Raman spectroscopy. In contrast, the scratch process induces σ_s^R within the SiC grains and its magnitude increases with load.

Peak broadening and peak asymmetry of the Raman spectra due to the scratch process, can clearly be observed in Fig. 4-15. This indicated a structural disorder inside the SiC grains.¹⁹¹ The extent of disorder increased with increasing scratch load. Stacking faults have been identified as the primary defects in SiC whiskers¹⁹⁵ and in polycrystalline SiC.¹⁹⁶ It has been reported that an increase in number of stacking faults caused Raman peak shift to lower wave numbers as well as peak broadening in 3C-SiC ceramics.¹⁹¹ Based on the bond polarizability model, Rohmfeld *et al.*,¹⁹¹ simulated the influence of stacking fault distance on the TO-phonon mode in 3C-SiC. It was shown that as the average stacking fault distance decreased (i.e., structural disorder increased with increase in stacking fault density), the peak shifted to lower frequencies and line-broadening was observed in the TO-phonon peak.

In the current study, similar observations with increasing scratch load were noted in the Raman spectra collected from the SiC grains residing within the scratch grooves. Therefore, it is argued that as the scratch load increased, a greater number of stacking faults (i.e. structural disorder) was generated within the SiC grains which in turn caused an increase in the residual tensile stress. In the following, the shift in the Raman peak positions with scratch load will be

quantified in terms of residual stress within the SiC grains. The TO-peaks were relatively more symmetric compared to the LO-peak and therefore, we will consider only the TO-peak shifts for residual stress calculation.

4.3.4 Evolution of Residual Stress Field

Before embarking on the determination of residual stress from Raman spectra, first the processing-induced residual stress state within the composite¹⁹⁷ and residual stress field that evolves in a brittle material due to a scratch process have been discussed.^{150,151} Then, Raman peak shift has been correlated to the appropriate stress component to determine the scratch-induced residual stress.

4.3.4.1 Residual stress in SiC grains of as-processed composite

In the ZrB₂-SiC composite, the SiC grains (which are assumed equiaxed and almost spherical as can be seen from Fig. 4-6) can be assumed as the elastic spheres of uniform size distributed in an infinite elastic continuum of ZrB₂ matrix.¹⁹⁷ This results in axially symmetric stress distribution around SiC grains. Let us consider that the grain has an effective radius a and the surrounding matrix has a radius b . It has been shown that the ceramic grain will be under a uniform/hydrostatic pressure P which can be expressed as¹⁹⁷

$$P = \frac{(\alpha_m - \alpha_p)\Delta T}{\left[\frac{0.5(1 + \nu_m) + (1 - 2\nu_m)V_p}{E_m(1 - V_p)} + \frac{1 - 2\nu_p}{E_p} \right]} \quad (4-11)$$

where ν is Poisson's ratio, ΔT is temperature change, V_p is volume fraction of grains, and subscripts m and p stand for matrix and grain. On the other hand,

radial (σ_{rad}) and tangential (σ_{tan}) stresses within the ZrB₂ matrix and at a distance r from the center of grain are expressed, respectively, as¹⁹⁷

$$\sigma_{rad} = \frac{P}{1-V_p} \left[\frac{a^3}{r^3} - V_p \right] \quad \text{and} \quad \sigma_{tan} = -\frac{P}{1-V_p} \left[\frac{a^3}{2r^3} + V_p \right]. \quad (4-12)$$

Thus, from the above equations it can be seen that when $\alpha_m > \alpha_p$, as is the case for ZrB₂-SiC composites, cooling of the composite from the sintering temperature will induce a uniform compressive stress within the SiC grains. The radial and tangential stresses within ZrB₂ will be compressive and tensile, respectively, and both the stresses will be maximum at the ZrB₂-SiC interface.

4.3.4.2 Residual stress in SiC grains located within the scratch grooves

The mechanical residual stress induced by the scratch process needs more in-depth analysis. As discussed before, single-pass scratch processes have been widely modeled^{150,151} as a sliding microindentation event where point loads are simultaneously applied in normal (F_n) and tangential (F_t) directions on the surface of a specimen as shown schematically in Fig. 4-11. Also, see Fig. 4-17 where various crack systems which evolve as a result of the scratch process are shown and will be further discussed later in this section. The complete elastic stress field during the scratch process is constructed from the superposition of the Boussinesq field, Cerruti field^{150,151,167} and Yoffe's blister field.¹⁶⁸ The origin of Boussinesq and Cerruti elastic fields has been already discussed in section 4.2. The blister field is an inelastic stress field related to the residual stress due to loading and unloading of the point normal loads.

During the sliding process, due to the misfit strain of deformation between elastic and plastic regions, residual stresses are induced within the material during unloading of the scratch tool. According to sliding blister field model (SBFM)^{150,151} the normal residual elastic-stress components (σ^R) along x-, y- and z- directions are expressed as

$$\frac{\sigma_x^R}{2B} = -\frac{2\nu(y^2 - z^2)}{(y^2 + z^2)^2} + \frac{x}{(y^2 + z^2)^2 \rho^5} * (2\nu x^4 y^2 - 2x^2 y^4 + 6\nu x^2 y^4 - 2y^6 + 4\nu y^6 - 2\nu x^4 z^2 - 4x^2 y^2 z^2 + 2\nu x^2 y^2 z^2 - 3y^4 z^2 + 6\nu y^4 z^2 - 2\nu x^2 z^4 - 4\nu x^2 z^4 + z^6 - 2\nu z^6) \quad (4-13)$$

$$\frac{\sigma_y^R}{2B} = -\frac{2y^2(y^2 - 3z^2)}{(y^2 + z^2)^3} + \frac{x}{(y^2 + z^2)^3 \rho^5} * (2x^4 y^4 + 6x^2 y^6 - 2\nu x^2 y^6 + 4y^8 - 2\nu y^8 - 6x^4 y^2 z^2 - 7x^4 y^2 z^2 - 6\nu x^2 y^4 z^2 - 2y^6 z^2 - 8\nu y^6 z^2 - 12x^2 y^2 z^4 - 6\nu x^2 y^2 z^4 - 15y^4 z^4 - 12\nu y^4 z^4 + x^2 z^6 - 2\nu x^2 z^6 - 8y^2 z^6 - 8\nu y^2 z^6 + z^8 - 2\nu z^8) \quad (4-14)$$

$$\frac{\sigma_z^R}{2B} = -\frac{2z^2(y^2 - 3y^2)}{(y^2 + z^2)^3} + \frac{xz^2}{(y^2 + z^2)^3 \rho^5} * (6x^4 y^2 + 15x^2 y^4 + 9y^6 - 2x^4 z^2 + 10x^2 y^2 z^2 + 12y^4 z^2 - 5x^2 z^4 - 3y^2 z^4 - 6z^6) \quad (4-15)$$

where $\rho^2 = x^2 + y^2 + z^2$ and B is the blister field strength per unit length.^{150,151}

Figure 4-18 shows the 3-D distribution of the three normal residual stress components σ_x^R , σ_y^R and σ_z^R (all normalized with $\frac{P}{2c^2}$) for $B/P = 0.005$ on the x-y plane in the vicinity of the indenter tip during a scratch process.¹⁵⁰ These normal residual stress components arise during a scratch process as the indenter moves from $\bar{x} = -\infty$ ($\bar{x} = \frac{x}{c}$) to its present location at $\bar{x} = 0$. It is seen from Fig. 4-18 (C) that σ_z^R is highly tensile in the wake of the scratch tool whereas σ_x^R and σ_y^R are compressive directly behind the indenter along the \bar{x} -axis. σ_y^R is slightly tensile

away from \bar{x} -axis behind the indenter. σ_z^R reaches its maximum value just behind the indenter ($\bar{x} < 0$), see Fig. 4-18 (C), and its magnitude is significantly larger than σ_x^R and σ_y^R . From these 3-D scratch-induced residual stress distributions, it is clear that σ_z^R is the most dominant residual stress component and is known to contribute to subsurface lateral crack initiation¹⁵⁰ which was also observed to some extent in the current study. With increasing scratch load, the strength B of the sliding blister field also increases and therefore, the magnitude of σ_z^R will also increase causing greater lateral cracking and material removal in brittle materials. Due to these reasons, in the following section, the above residual stress component σ_z^R will be correlated to the Raman peak shifts observed in Figs. 4-15 and 4-16, and magnitude of residual stress within the SiC grains residing within the scratch grooves will be quantified.

4.3.5 Relationship between Mechanical Residual Stress and Raman Spectroscopy

Recall that Raman peak shift is related to induced strain in a deformed specimen. If the Raman wave numbers of optical phonons, in the absence and the presence of strain, are denoted by w_{0j} and w_j ($j = 1-3$), respectively, then the strain-induced Raman shift, Δw_j , is expressed as^{183,188}

$$\Delta w_j = w_j - w_{j0} \approx \frac{\lambda_j}{2w_{j0}} \quad (4-16)$$

where λ_j are the Eigen values of the well known “secular equation”, relating strain to Raman peak shift for diamond and zinc-blende structures,^{183,188,192,198} as

$$\begin{vmatrix} p\varepsilon_x^R + q(\varepsilon_y^R + \varepsilon_z^R) - \lambda & r\gamma_{xy}^R & r\gamma_{xz}^R \\ r\gamma_{xy}^R & p\varepsilon_y^R + q(\varepsilon_x^R + \varepsilon_z^R) - \lambda & r\gamma_{yz}^R \\ r\gamma_{xz}^R & r\gamma_{yz}^R & p\varepsilon_z^R + q(\varepsilon_x^R + \varepsilon_y^R) - \lambda \end{vmatrix} = 0 \quad (4-17)$$

where p , q and r are the phonon deformation potentials which describe the change in effective spring constants induced by the strain, and ε^R and γ^R are the residual normal and shear strain tensor components, respectively. 3C-SiC has a zincblende crystal structure¹⁹² and the relation between residual strain and stress tensor components, for this structure, can be expressed according to Hooke's law as^{189,199}

$$\begin{Bmatrix} \varepsilon_x^R \\ \varepsilon_y^R \\ \varepsilon_z^R \\ \gamma_{xy}^R \\ \gamma_{xz}^R \\ \gamma_{yz}^R \end{Bmatrix} = \begin{bmatrix} S_{11} & S_{12} & S_{13} & 0 & 0 & 0 \\ S_{21} & S_{22} & S_{23} & 0 & 0 & 0 \\ S_{31} & S_{32} & S_{33} & 0 & 0 & 0 \\ 0 & 0 & 0 & S_{44} & 0 & 0 \\ 0 & 0 & 0 & 0 & S_{55} & 0 \\ 0 & 0 & 0 & 0 & 0 & S_{66} \end{bmatrix} \begin{Bmatrix} \sigma_x^R \\ \sigma_y^R \\ \sigma_z^R \\ \tau_{xy}^R \\ \tau_{xz}^R \\ \tau_{yz}^R \end{Bmatrix} \quad (4-18)$$

where the S terms represent the compliances and σ^R and τ^R are the residual normal and shear stress components, respectively. For cubic structures,

$$S_{11} = S_{22} = S_{33}, \quad S_{12} = S_{13} = S_{21} = S_{23} = S_{31} = S_{32} \quad \text{and} \quad S_{44} = S_{55} = S_{66}.$$

As discussed previously, the magnitude of σ_z^R is significantly greater compared to the other two normal stress components and therefore, to simplify the residual stress calculations, we neglect all other residual normal (σ_x^R and σ_y^R) and shear stress (γ_{xy}^R , γ_{yz}^R and γ_{xz}^R) components in the subsequent discussions. Accordingly, solving equation (4-18), the following relationships will be obtained

$$\varepsilon_x^R = S_{13}\sigma_z^R, \quad \varepsilon_y^R = S_{23}\sigma_z^R, \quad \varepsilon_z^R = S_{33}\sigma_z^R \text{ and } \gamma_{xy}^R = \gamma_{xz}^R = \gamma_{yz}^R = 0. \quad (4-19)$$

Noting that $S_{33} = S_{11}$ and $S_{13} = S_{23} = S_{12}$, the normal strain components in equation (4-19) can be rewritten as

$$\varepsilon_x^R = S_{12}\sigma_z^R, \quad \varepsilon_y^R = S_{12}\sigma_z^R \text{ and } \varepsilon_z^R = S_{11}\sigma_z^R. \quad (4-20)$$

Thus, equation (8) reduces to

$$\begin{vmatrix} p\varepsilon_x^R + q(\varepsilon_y^R + \varepsilon_z^R) - \lambda & 0 & 0 \\ 0 & p\varepsilon_y^R + q(\varepsilon_x^R + \varepsilon_z^R) - \lambda & 0 \\ 0 & 0 & p\varepsilon_z^R + q(\varepsilon_x^R + \varepsilon_y^R) - \lambda \end{vmatrix} = 0 \quad (4-21)$$

Solving for λ and substituting ε_x^R , ε_y^R and ε_z^R from equation (4-20), the following expressions are obtained

$$\lambda_1 = \sigma_z^R \{S_{12}(p+q) + S_{11}q\},$$

$$\lambda_2 = \sigma_z^R \{S_{12}(p+q) + S_{11}q\},$$

$$\text{and } \lambda_3 = \sigma_z^R (S_{11}p + 2S_{12}q). \quad (4-22)$$

Now, substituting the above λ_1 , λ_2 and λ_3 expressions in equation (4-16), the relation between Raman shift and residual stress can be expressed as

$$\Delta w_1 = \frac{1}{2w_{o1}} \{S_{12}(p+q) + S_{11}q\} \sigma_z^R, \quad (4-23)$$

$$\Delta w_2 = \frac{1}{2w_{o2}} \{S_{12}(p+q) + S_{11}q\} \sigma_z^R, \quad (4-$$

24)

and

$$\Delta w_3 = \frac{1}{2w_{o3}} \{S_{11}p + 2S_{12}q\} \sigma_z^R. \quad (4-25)$$

Now the above equations will be used to calculate the residual stress from the observed Raman peak shifts shown in Fig. 4-16. In strained diamond cubic and zinc-blende crystal structures, a maximum of three Raman modes are possible, two TO- vibrations and one LO-vibration.¹⁹⁸ The first two Raman modes (w_1 and w_2) correspond to TO-peaks whereas the third Raman mode (w_3) is associated with the LO-peak. Therefore, equations (4-23) and (4-24) can be used to calculate residual stress from TO-peak shift whereas equation (4-25) can be utilized to calculate residual stress from LO-peak shift. The values of p and q for 3C-SiC are not available directly in literature. Therefore, these values have been calculated in the following way. The mode Grüneisen parameters for hydrostatic stress (γ_o) and uniaxial stress (γ_s) are defined as¹⁹²

$$\gamma_o = -\frac{(p+2q)}{6w_o^2} \quad \text{and} \quad \gamma_s = \frac{(p-q)}{2w_o^2} \quad (4-26)$$

where w_o is the Raman peak in strain-free condition. The mode Grüneisen parameter for the TO-phonon (γ_o^{TO}) in 3C-SiC is 1.56,¹⁹² but the value of γ_s^{TO} is not readily available. Although, for uniaxial and biaxial stresses, γ_s^{TO} and γ_o^{TO} may differ, it has been assumed here that $\gamma_s^{TO} = \gamma_o^{TO} = 1.56$. For the TO-peak, assuming $w_o = 796 \text{ cm}^{-1}$, one obtains $p^{TO} = -0.623 \times 10^6 / \text{cm}^2$ and $q^{TO} = -2.634 \times 10^6 / \text{cm}^2$. Also, for residual stress calculation, the following values of compliances have been used: $S_{11} = 3.7 \times 10^{-13} \text{ cm}^2/\text{dyn}$ and

$S_{12} = -1.05 \times 10^{-13} \text{ cm}^2/\text{dyn}$.²⁰⁰ The final expression for residual stress calculation from the TO-peak, using equation (4-23), is expressed as

$$\sigma_z^R = \frac{2w_{o1}}{\{S_{12}(p+q) + S_{11}q\}} \Delta w_1 = -251.66 \Delta w_{TO} \text{ (MPa)} \quad (4-27)$$

where Δw_{TO} is the shift in TO-peak position. From equation (4-27), it is clear that shift of TO-peaks to lower or higher wave number will result in tensile or compressive residual stress, respectively.

4.3.6 Determination of Residual Stress

Thermal residual stresses in the as-processed composite were calculated from equations (4-11) and (4-12) using the material properties and volume fractions of ZrB_2 and SiC phases as given in Table 4-1, and assuming an average radius of 1 μm for SiC phase. The temperature difference, ΔT , used in equation (4-11) was 1725°C . The calculation revealed that the SiC grains were under a uniform compressive residual stress of 1.731 GPa whereas the compressive radial and tensile tangential stresses at ZrB_2 -SiC interfaces were 1.731 GPa and 1.126 GPa, respectively. Magnitudes of these stresses decrease sharply away from the interface. The high tensile tangential stress at the interface can cause radial microcracking in the ZrB_2 matrix surrounding the SiC grains and eventually act as potential sites for the development of larger cracks or critical flaws.

Figure 4-19 shows the magnitude of mechanical residual stress within SiC grains (calculated from equation (4-27)) due to the scratch process as a function of applied scratch load. At 50 mN, residual stress was still compressive whereas

above 50 mN tensile residual stress was generated within the SiC grains and increased almost linearly in magnitude with scratch load. The highest mechanically-induced tensile residual stress at 250 mN within SiC grains was estimated to be around 2.6 GPa. Such large magnitude of residual stress has been reported on many material systems in the literature. Raman spectroscopic measurements have revealed tensile residual stress as high as 2.1 GPa in diamond films,^{201,202} up to 2 GPa in carbon thin films²⁰³ and up to 1.2 GPa in porous Si films.¹⁸³

The calculated tensile residual stress (2.6 GPa) at 250 mN in the SiC grains was well above the reported tensile fracture stress of 0.9 GPa for polycrystalline 3C-SiC.²⁰⁴ However, it was observed from the SEM micrographs that the SiC grains present within the grooves after the scratch, from which Raman spectra were collected, were crack-free at this scale. For example, Fig. 4-20 revealed that a SiC grain within a groove formed at 250 mN load was completely intact whereas the surrounding ZrB₂ matrix was heavily microcracked due to the scratch process. Similar features were also observed at several locations within the scratch grooves. These observations indicate unusually high fracture strength of the SiC grains in the composite compared to a typical polycrystalline SiC ceramic. In this scenario, it may not be appropriate to directly compare the available fracture strength values of polycrystalline SiC ceramics to SiC grains present within the particulate phase distributed in the ZrB₂-SiC composite. Besides, typical polycrystalline 3C-SiC ceramics contain large elongated grains with a high aspect ratio in the range 2-6,²⁰⁴ whereas the SiC grains present in the

composite were almost equiaxed. Microstructural investigations did not reveal any porosity within SiC phase. Also, no sintering additive was used during the processing and hence no grain boundary glassy phase is expected.

Polycrystalline SiC ceramics are known to exhibit predominantly intergranular fracture mode as opposed to transgranular fracture.^{204,205} The density of critical flaws or defects that can act as nucleation sites for crack propagation is expected to be much higher in a monolithic ceramic compared to the defect density within the isolated grains of same size in a composite. Therefore, in the absence of pores, secondary glassy phase and limited SiC-SiC grain boundary areas, transgranular fracture is expected to be the predominant mode to relieve the accumulated residual stress within the individual SiC grains.

Possible sources of transgranular crack initiation will be the internal flaws present within these individual SiC grains. Fracture stress of a polycrystalline ceramic is limited by the critical flaw size which scales down with grain size. This in turn increases the macroscopic fracture strength. Based on this fact, a simple fracture mechanics based (using Griffith criterion) calculation was made to estimate the minimum fracture strength of these individual grains. Thus, if one considers crack initiation/propagation from a pre-existing critical flaw, then its maximum size will be equivalent to the grain size which will result minimum fracture strength. For a critical flaw size of c , assuming semielliptical surface flaws, the fracture strength (σ_f) and mode I fracture toughness (K_c) are related by²⁰⁶

$$\sigma_f = \frac{K_c}{1.35\sqrt{c}}. \quad (4-28)$$

Clearly, estimation of σ_f is dependent on the chosen K_C and the c values which are not readily known for this particular SiC phase present within the composite. Depending on the assumptions made on the nature of SiC phase (whether monocrystalline or polycrystalline) distributed within the ZrB₂ matrix, the estimated σ_f can differ considerably. If it is considered that the SiC phase in the composite is to be made of several grains, then it is appropriate to consider a critical flaw size of the order of average grain size ($\sim 1\mu\text{m}$) for the estimation of minimum σ_f . The available fracture toughness values for polycrystalline SiC ceramics vary over a broad range (3.4-6.8 MPa.m^{1/2}) and depend process conditions as well as microstructural features such as average grain size, shape, aspect ratio, etc.^{205,206} For these values, equation (4-28) results in a minimum fracture strength between 2.5-5 GPa. These values provide a conservative estimate of σ_f . On the other hand, if one assumes SiC phase to be a single crystal, a more complicated situation arises. In a single crystal, typical processing- or deformation-induced defects are vacancies, interstitials, dislocations, stacking faults, twinning etc., which are significantly smaller in size than a grain level microcrack. In the current study, the measured Raman peak shift has been related to the development of deformation-induced stacking faults within the SiC phase. Therefore, it has been conjectured that stacking faults are the main source for crack nucleation. Based on the micrographs of stacking faults presented in Shih *et al.*,¹⁹⁶ the width of the stacking faults are taken as 50 nm. Using a K_C value of 3.2 MPa.m^{1/2} for a single crystal 3C-SiC thin film,²⁰⁷ a

fracture strength of 10.6 GPa was obtained. This value is only 2-4 times the conservative estimate made earlier based on microscopic flaw size. Therefore, it is argued that due to small size and high fracture strength, SiC grains dispersed within ZrB₂ phase were able to sustain the large scratch-induced tensile residual stress without any fracture.

Raman stress coefficients (defined as the change in Raman peak position per unit residual stress) for diamond, SiC and Si are in the range of 0.4-4 cm⁻¹/GPa.^{183,187-190,192,198,208-210} This indicates that small changes in Raman peak positions may result in large residual stress. In the current investigation large peak shifts to lower wave numbers, particularly at 250 mN, were observed (see Fig. 4-16). From the calculated tensile residual stress, the Raman stress coefficient was estimated to be 3.9 cm⁻¹/GPa which is in the above range of the reported Raman stress coefficients for various materials. Also, residual stress measurements employing micro-Raman spectroscopy are highly dependent on spatial location within the grains (due to small spot size of the incident beam) and hence provides only localized residual stress values within small regions. Therefore, it should be noted that the estimated high tensile residual stress is only a localized value and not necessarily the average over the entire SiC grain(s).

From the above discussion, it is clear that the SiC grains in ZrB₂-SiC composite were initially in a state of residual compressive stress and the scratch process induces large residual tensile stress. Similar to the SiC, tensile residual stress is also expected to develop within the ZrB₂ matrix, particularly at higher

scratch loads. Although the magnitude of residual stress was unknown in the ZrB₂ phase as it is not Raman active, evolution of residual tensile stress-state within ZrB₂ matrix was evidenced from the onset of lateral crack formation at 250 mN. Although unknown, scratch-induced tensile residual stress within ZrB₂ at 250 mN is predicted to be close to its fracture strength (around 500 MPa).² Since the ZrB₂ phase is continuous and coarse-grained, it cannot sustain high tensile residual stress similar to the individual SiC grains. It is argued that up to 200 mN scratch load, the magnitude of tensile residual stress within the ZrB₂ phase was probably below the fracture stress to cause any lateral cracking. But above 250 mN, tensile residual stress can locally become comparable to or higher than the fracture stress of ZrB₂ resulting in lateral cracking as seen in the experiments.

The above model for scratch-induced residual stress estimation within SiC grains in a ZrB₂-SiC composite is based on the sliding blister field model.^{150,151}

This analytical model was derived to predict the scratch-induced residual stress state in a homogeneous brittle material. But the scratch-induced residual stress state in a composite could be more complex and therefore, application of sliding blister model for residual stress determination may not yield exact values.

Another major assumption was that Raman peak shift is related to the dominant stress component (σ_z^R) in the scratch-induced residual stress field. Other stress components may also have some correlation to the observed Raman peak shifts in SiC grains. Nevertheless, the calculated values appear reasonable. Therefore, it was argued that the proposed model can be used for scratch-induced residual

stress determination in Raman active materials with diamond cubic or zinc-blende crystal structures.

4.4 Conclusions

Scratch experiments in constant load mode, using a Berkovich nanoindenter, revealed that both the scratch depth and width increased with scratch load. At lower scratch load levels (50-100 mN), smooth plastically deformed scratch grooves were observed without any significant macroscopic damage. Above a scratch load of 100 mN, considerable amount of damage and material removal along the scratch path were observed. In high velocity scratch experiments, extensive transgranular lateral cracking caused severe brittle damage and material removal in the composite. ZrB₂-SiC composite exhibited microplasticity in terms of multiple sets of slip-lines oriented at random angles to the scratch direction. This feature is attributed to the activation of multiple slip systems or occurrence of dislocation motion along preferred slip systems in randomly oriented grains. Different types of damage modes such as transgranular microcracking in ZrB₂ phase (inside the regions containing slip bands as well as in regions without any slip-lines), extensive lateral cracking, grain-boundary fracture and interfacial cracking at the ZrB₂-SiC interface were observed within the scratch grooves. The limited dislocation mobility is assumed to be responsible for the observed microcracks in the vicinity of slip-lines. On the other hand, microcracks observed outside the slip band regions are assumed to initiate from pre-existing (processing-induced) defects in the composite. Also, the microscopic observations indicated that slip-lines occurred first followed by microcracking. An analytical model, based on the elastic stress field solutions for

a single-pass scratch event, was utilized to rationalize the experimental observations. The analysis revealed that during the scratch process, considerable amount of shear stress develops ahead of the indenter tip whereas tensile stress develops in the wake of the indenter. From the mechanistic analysis, it was concluded that the shear stress resulted in slip-line formation ahead of the indenter, whereas orthogonal microcracks (with respect to the scratch direction) resulted from the tensile stress which develops in the wake of the indenter. The stress analysis also confirmed that the slip-lines formed first followed by microcracking. Micro-Raman spectroscopic measurements were conducted on 3C-SiC grains of as-processed ZrB₂-SiC composite as well as on grains that lie within the scratch grooves. It is found that the TO-peak and LO-Raman peak in 3C-SiC were shifted to increasingly lower wave numbers with increasing scratch loads. An analytical model was developed to relate the scratch-induced mechanical residual stresses within the SiC grains to the Raman peak shift in terms of phonon deformation potentials of 3C-SiC. Residual stress measurements using micro-Raman spectroscopy on SiC grains of ZrB₂-SiC composite revealed that these grains were under compressive residual stress in the as-processed composite and then experience tensile residual stress due to scratch-induced deformation. The magnitude of residual compressive stress in the as-processed composite is around 1.731 GPa and the scratch-induced tensile residual stress increases linearly with load. At 250 mN scratch load, the magnitude of tensile residual stress can be as high as 2.6 GPa.

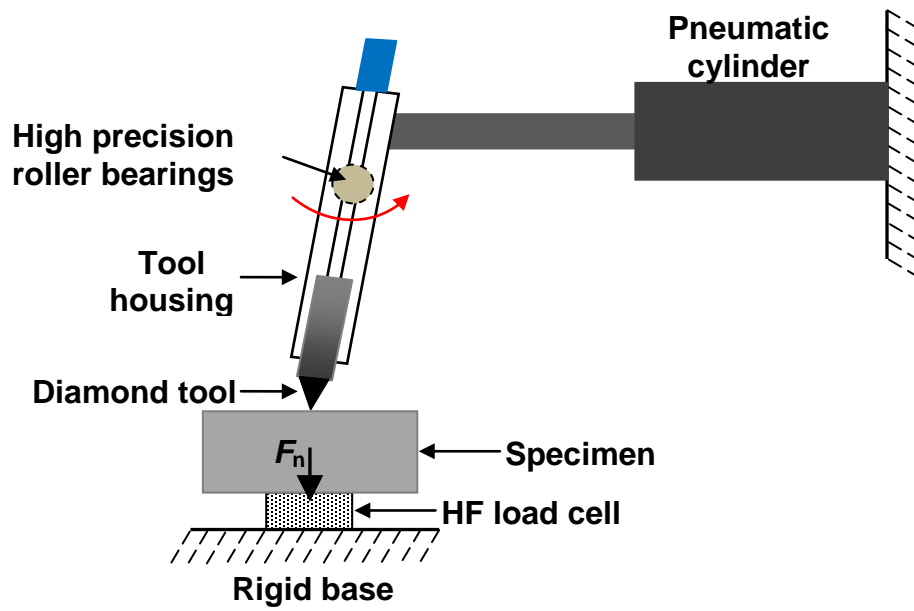


Figure 4-1. A schematic of instrumented high-velocity scratch tester.

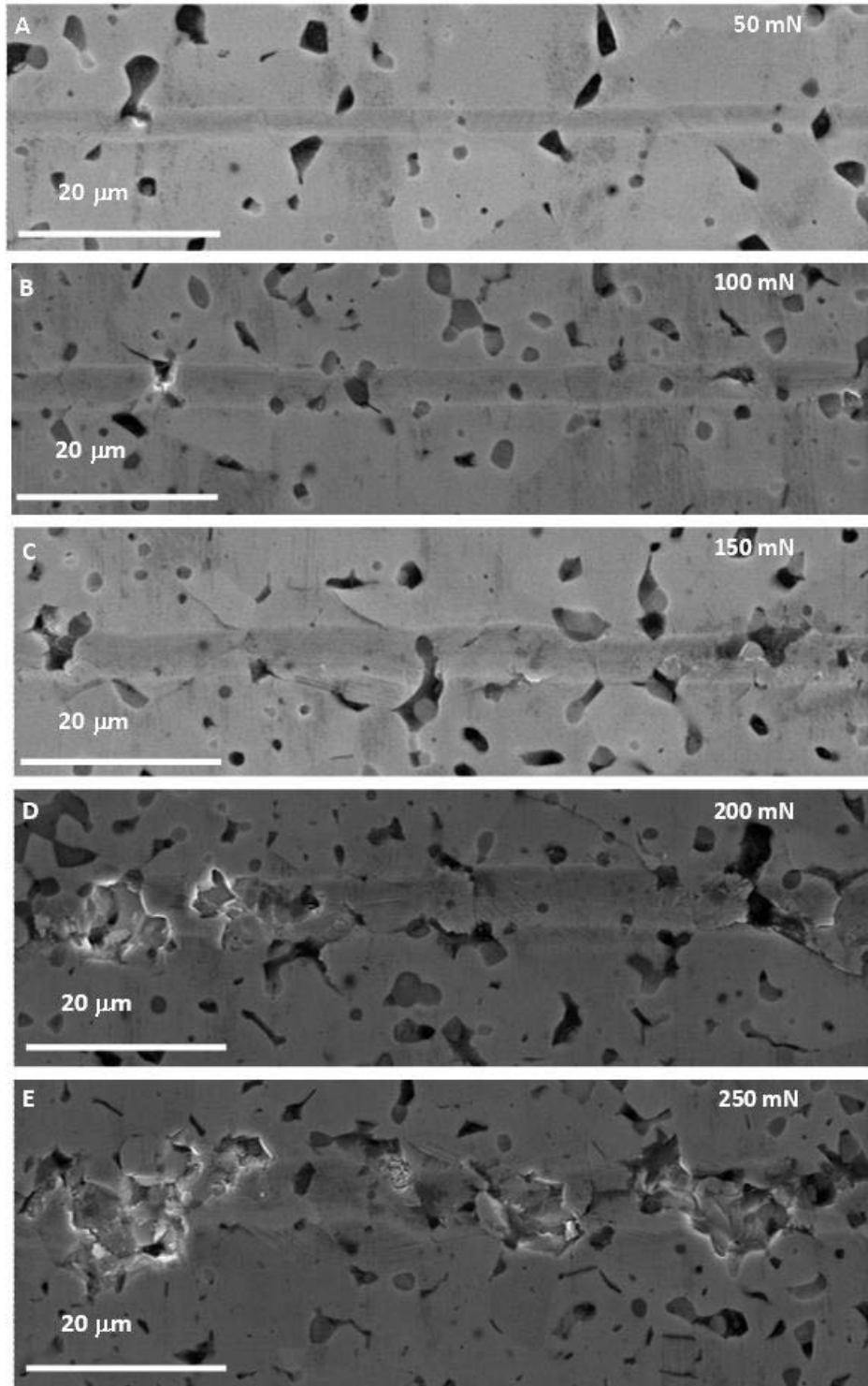


Figure 4-2. Residual scratch profiles on the polished surface of $\text{ZrB}_2\text{-SiC}$ composite at various load levels.

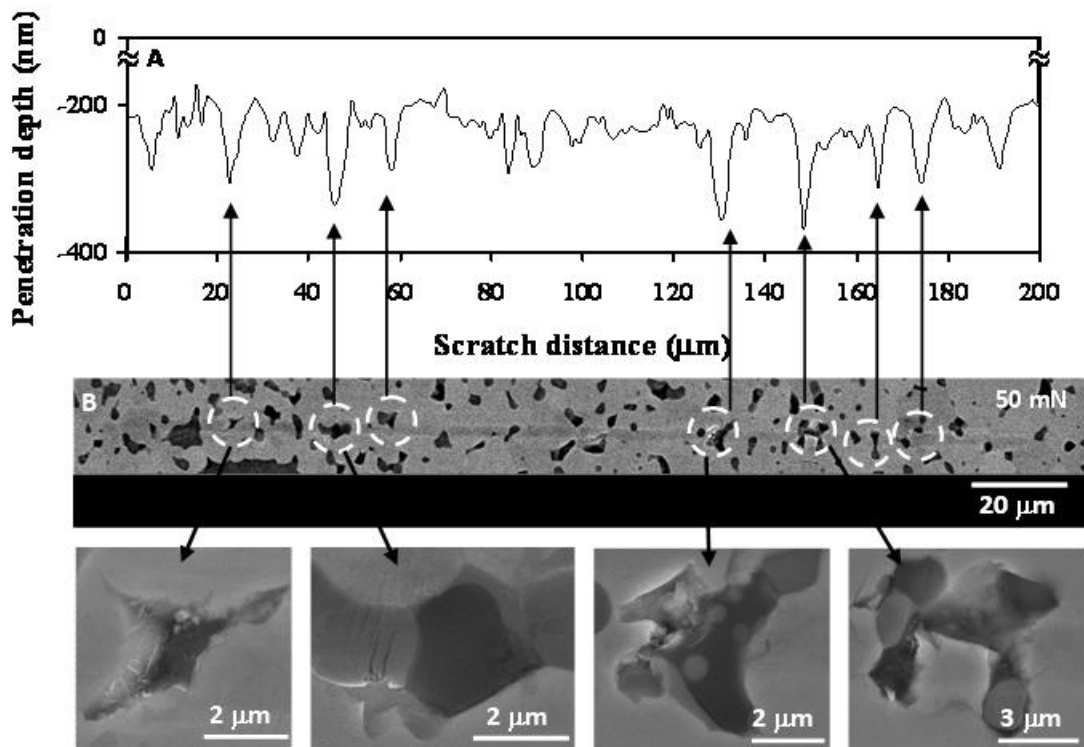


Figure 4-3. A) Penetration depth profile and B) the corresponding trace of residual scratch groove at 50 mN. Increase in scratch depth corresponds to the damaged regions as indicated by the white dashed circles in Fig. 4-3 B). Magnified SEM micrographs of the damaged regions along the scratch path revealed mostly voids, grain pull out, ZrB_2 grain-boundary fracture and some microcracking.

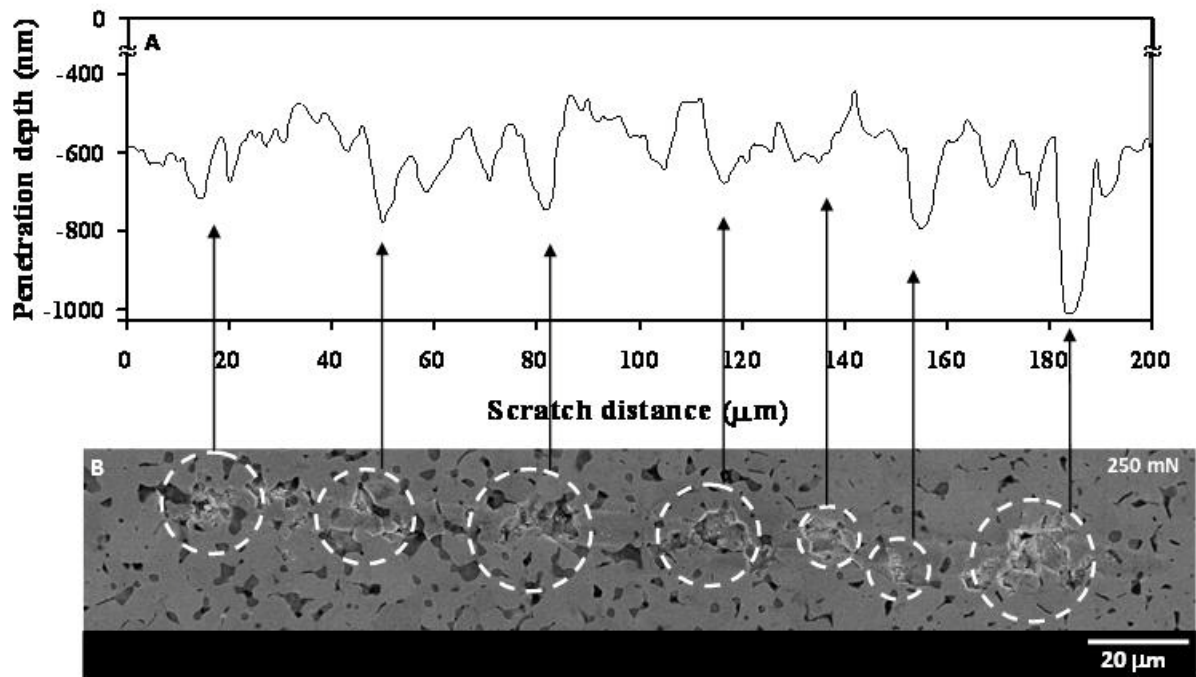


Figure 4-4. A) Penetration depth profile and B) the corresponding trace of residual scratch groove at 250 mN. Damaged regions along the scratch path are shown by the white dashed circles.

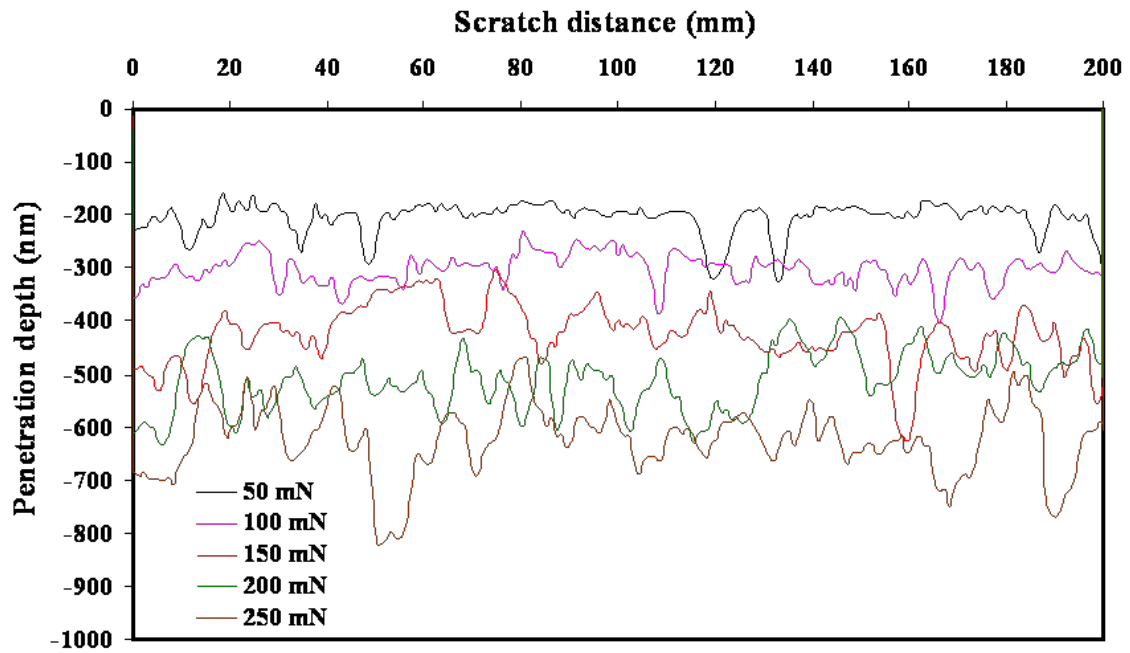


Figure 4-5. Scratch depth profiles during the nanoscratch experiments at different loads.

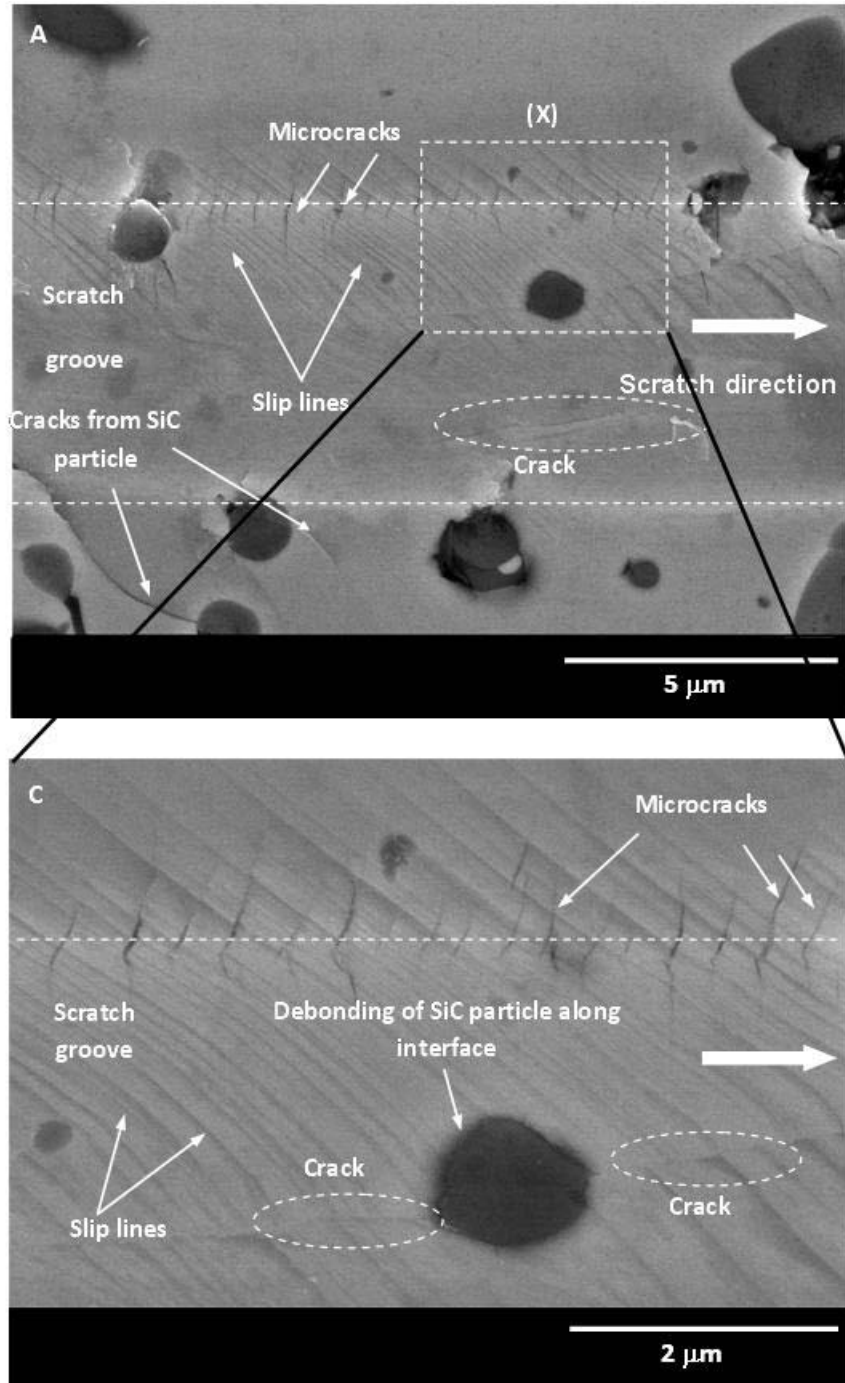


Figure 4-6. A) Micrograph of scratch induced deformation features at a load of 250 mN. B) A magnified view of the region (X) revealing the slip line patterns and microcracks along the scratch groove as well as cracks emanating from a SiC particle. C) Another region along the scratch path revealing several sets of slip lines oriented randomly with respect to the scratch direction.

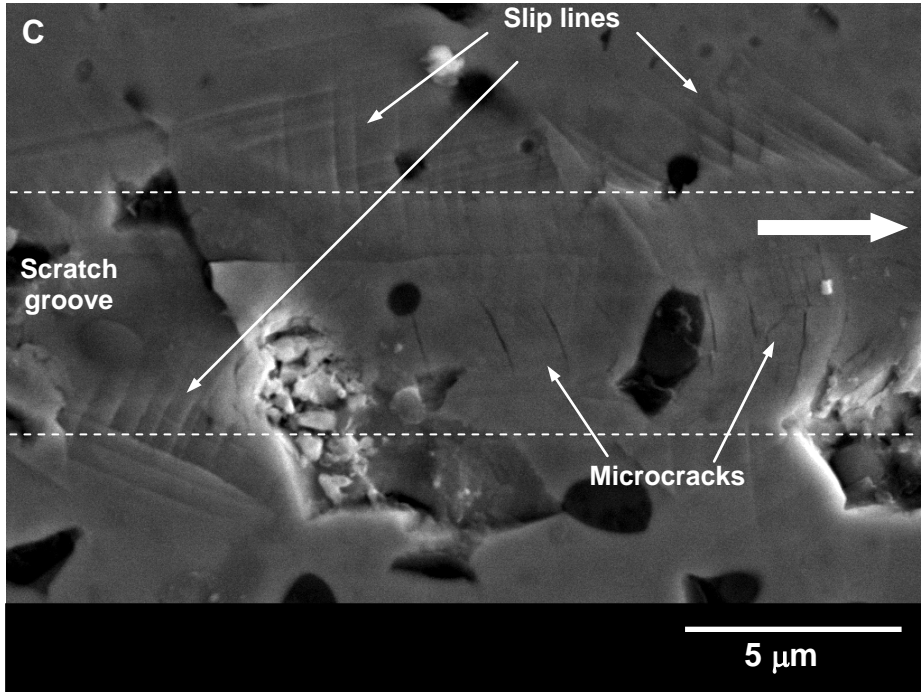


Figure 4-6. Continued

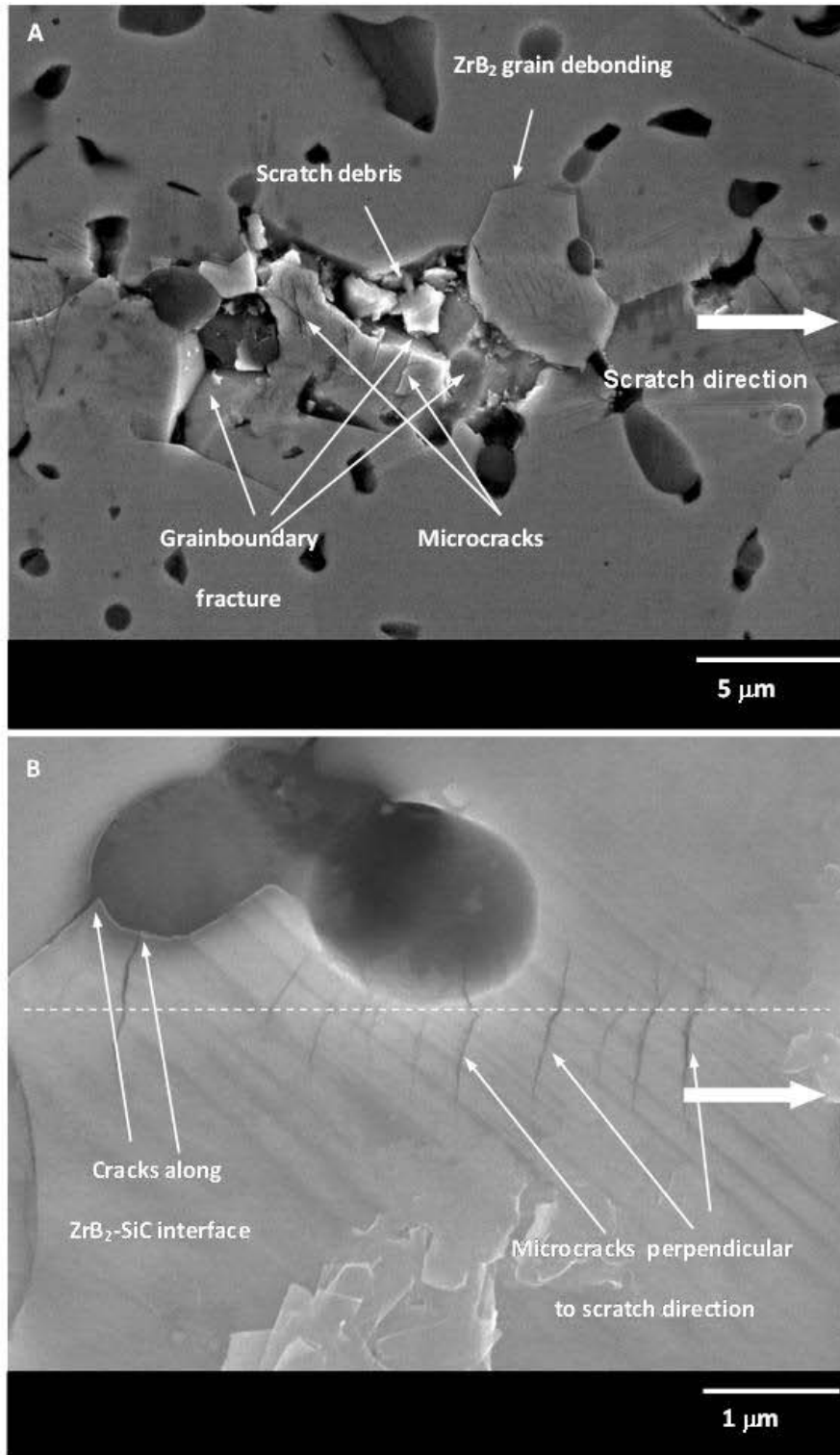


Figure 4-7. Fracture patterns within the scratch groove at a load of 250 mN: A) grain-boundary fracture, microcracking, and scratch debris and B) interfacial cracking between ZrB₂ and SiC phases as well as microcracks perpendicular to the direction of the scratch path.

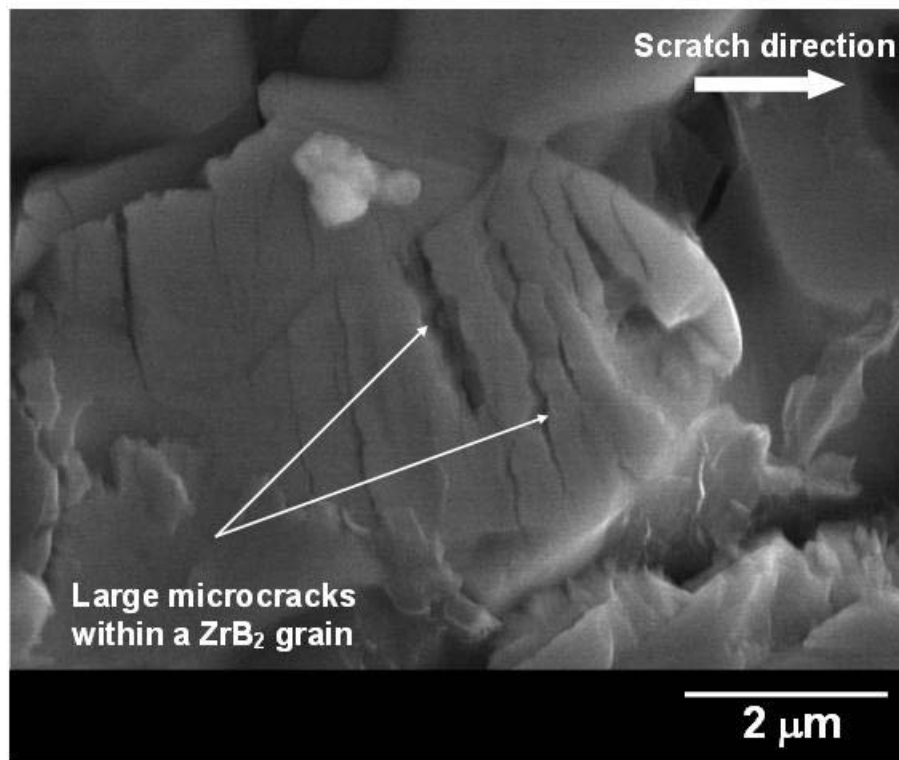


Figure 4-8. Scratch-induced damage at 250 mN, revealing transgranular microcracking in ZrB_2 -SiC composite.

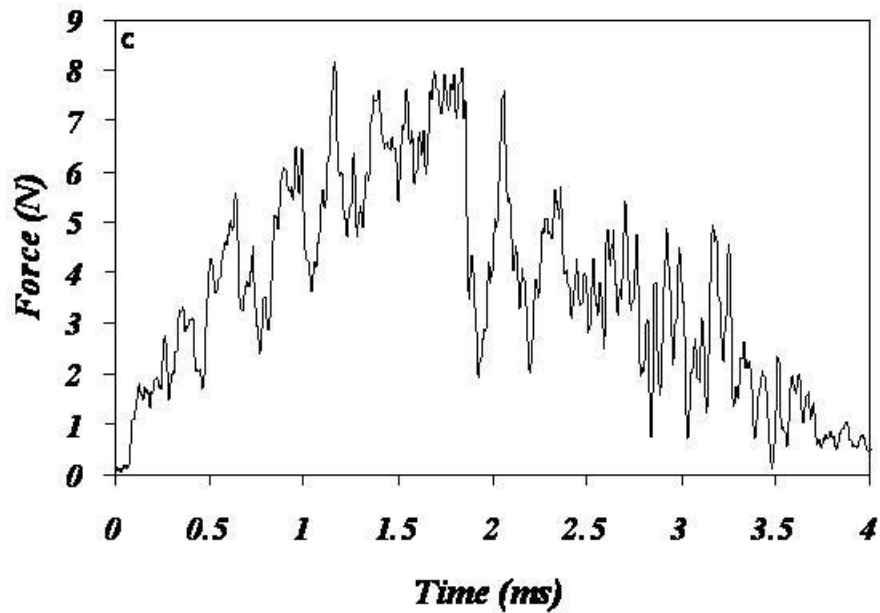
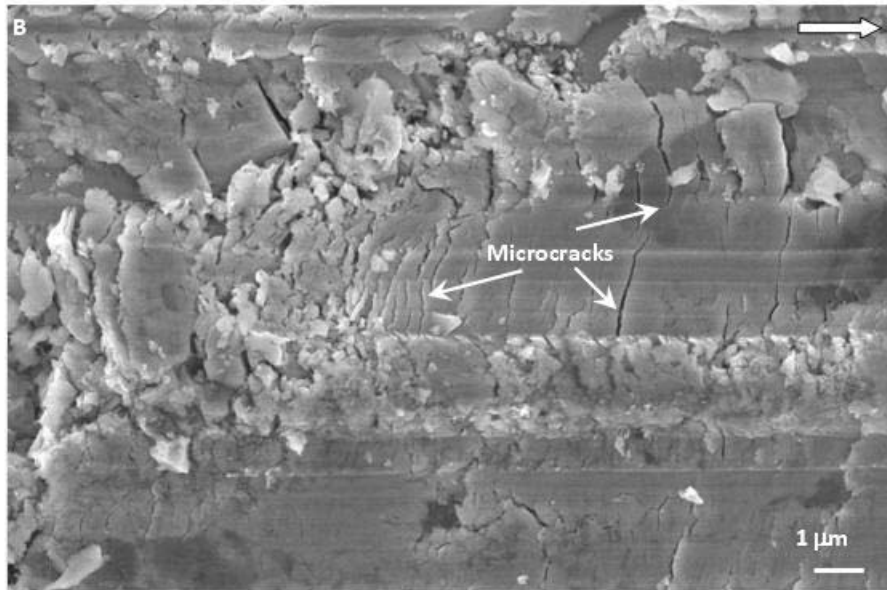
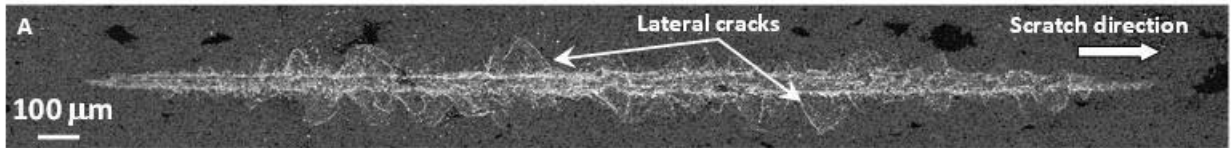


Figure 4-9. A) A high velocity scratch groove, B) high magnification images of extensive transgranular microcracks orthogonal to the scratch direction and C) normal force vs. scratch length profile.

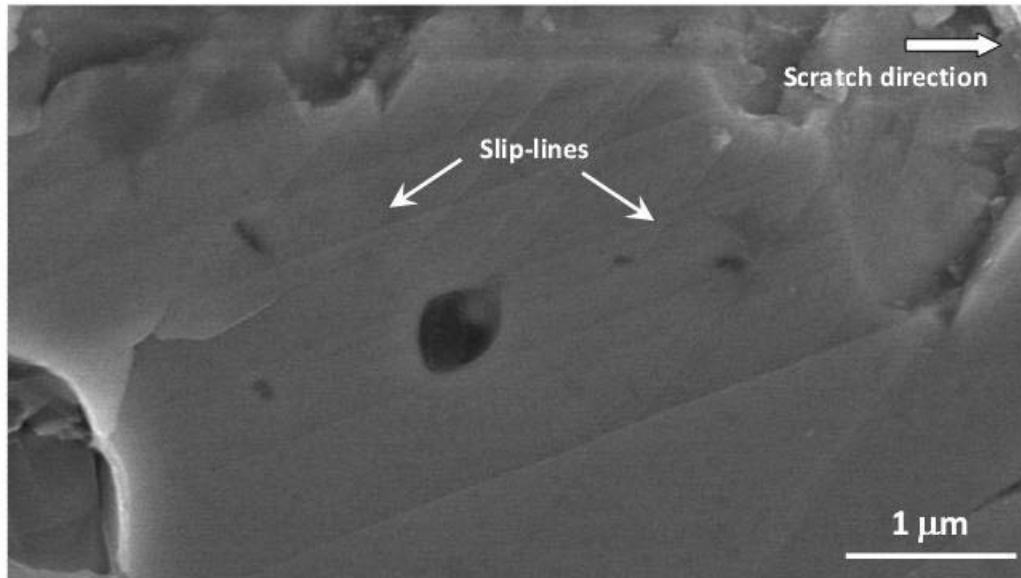


Figure 4-10. Slip-line formation within ZrB₂ phase during high-velocity scratch process.

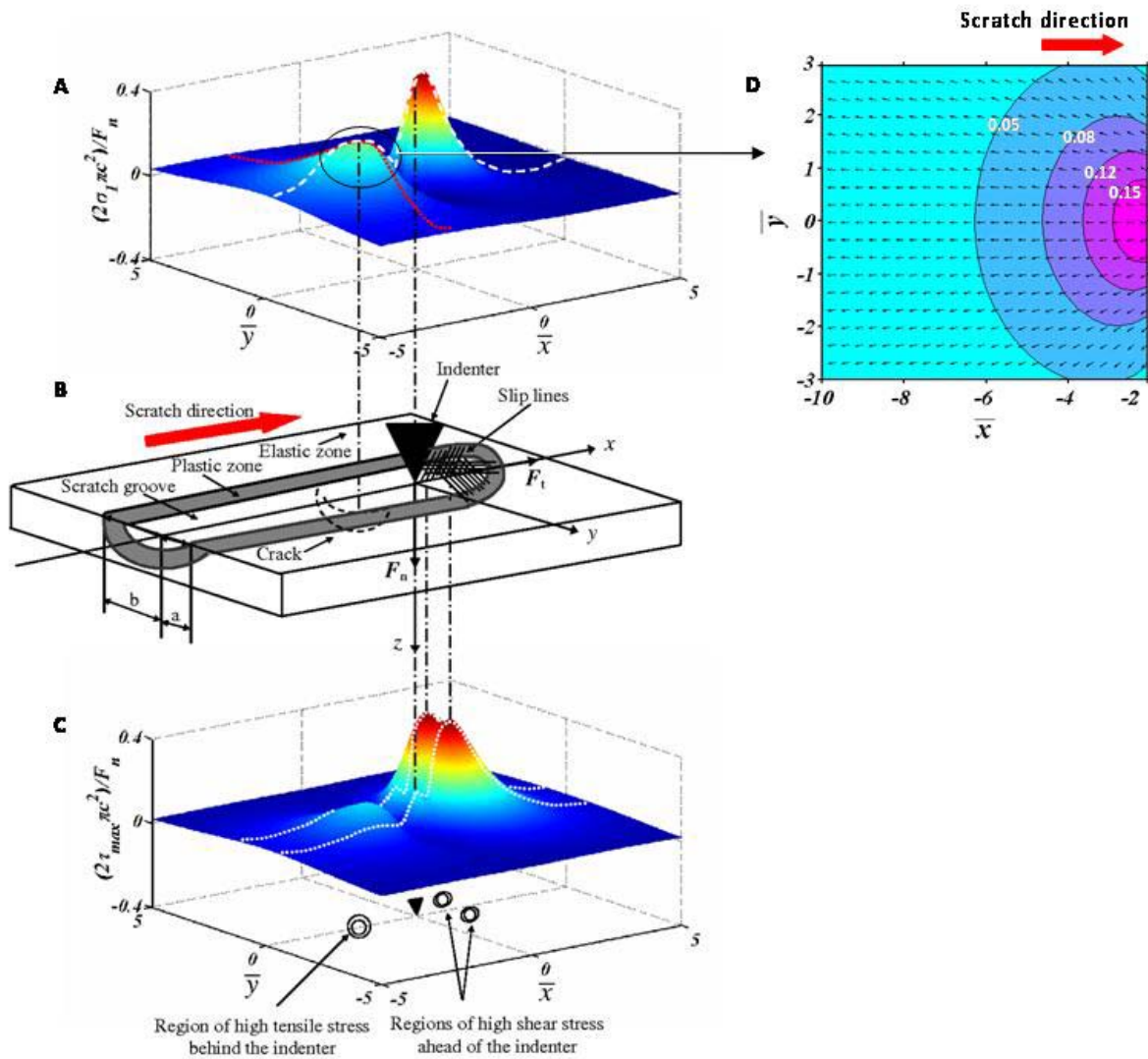


Figure 4-11. A) Normalized maximum principal stress distribution, B) schematic of the scratch process, C) normalized maximum shear stress distribution in the vicinity of indenter tip and D) plot of maximum principal stress contours and orientation in the wake of the indenter.

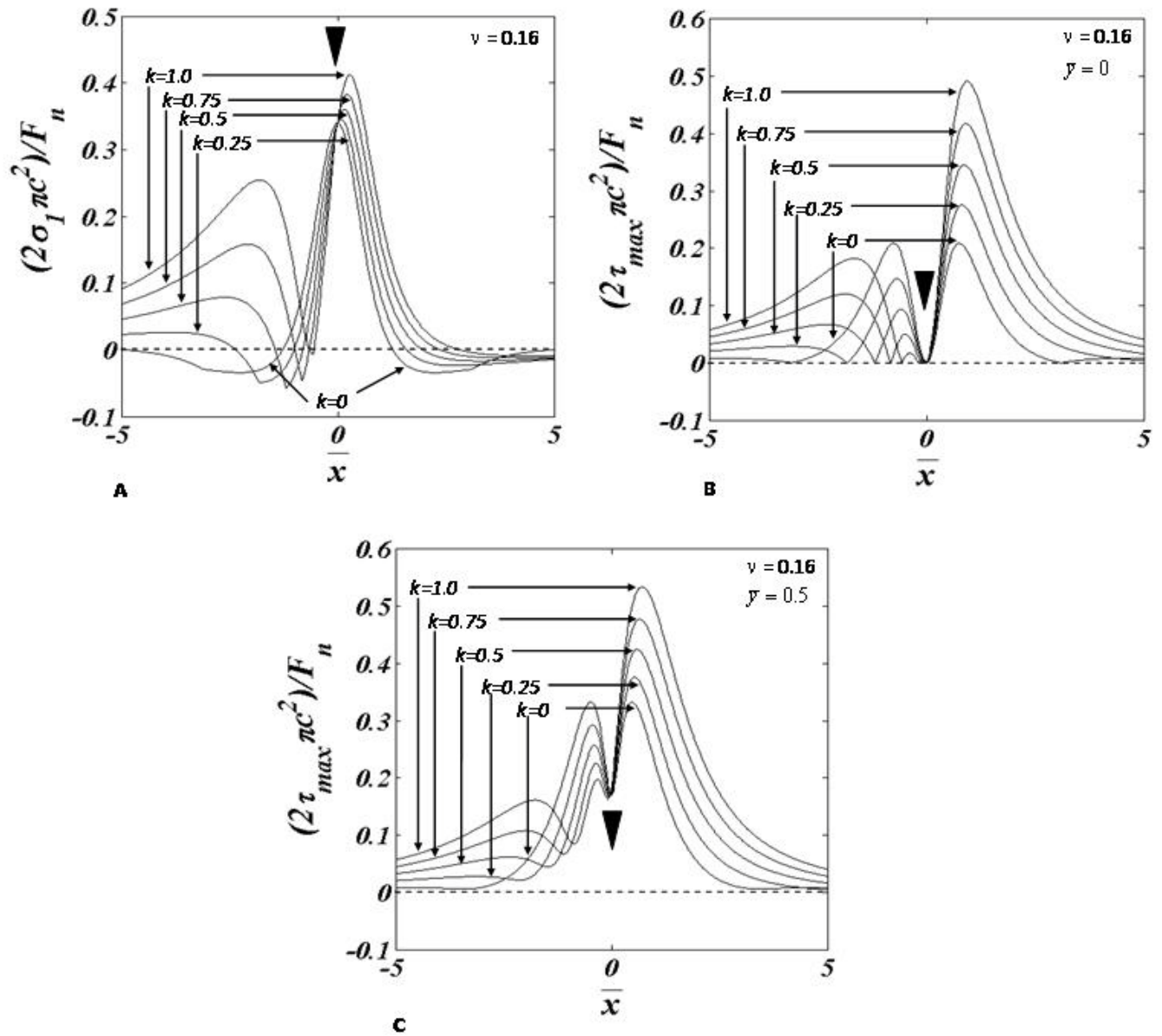


Figure 4-12. Variation of A) normalized maximum principal stress ($\bar{\sigma}_1$) at $\bar{y} = 0$ and B) normalized maximum shear stress ($\bar{\tau}_{max}$) at $\bar{y} = 0$ and C) $\bar{y} = 0.5$ for various values of 'k'. The black triangle indicates the indenter position.

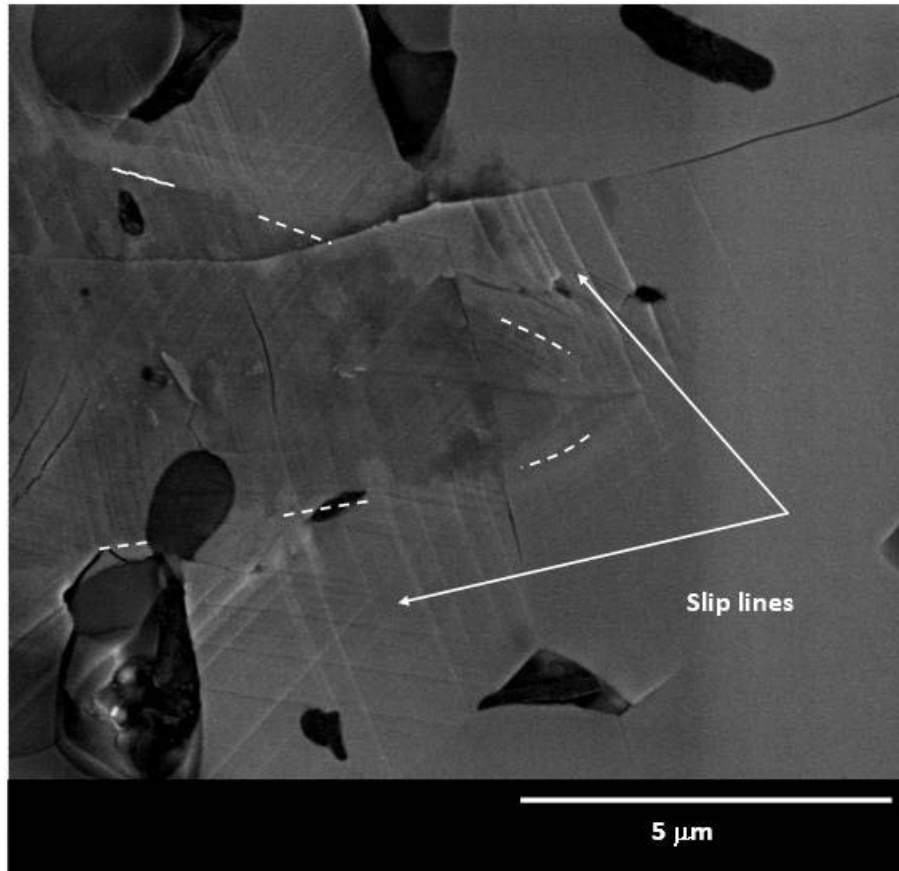


Figure 4-13. Micrograph of the exit-end region of a scratch at 250 mN revealing numerous slip lines. The white dotted lines indicate the boundary of residual scratch exit-end.

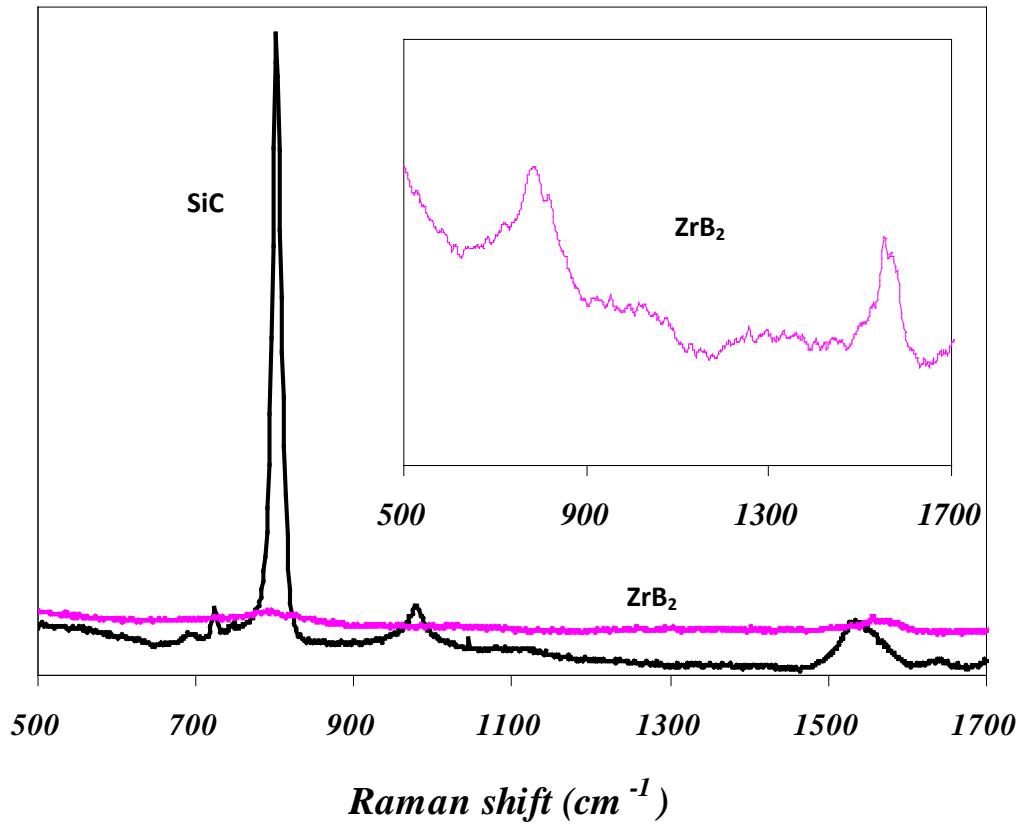


Figure 4-14. Raman spectra collected from the ZrB₂ matrix phase (see the inset also) and the SiC particulate phase present in ZrB₂-SiC composite.

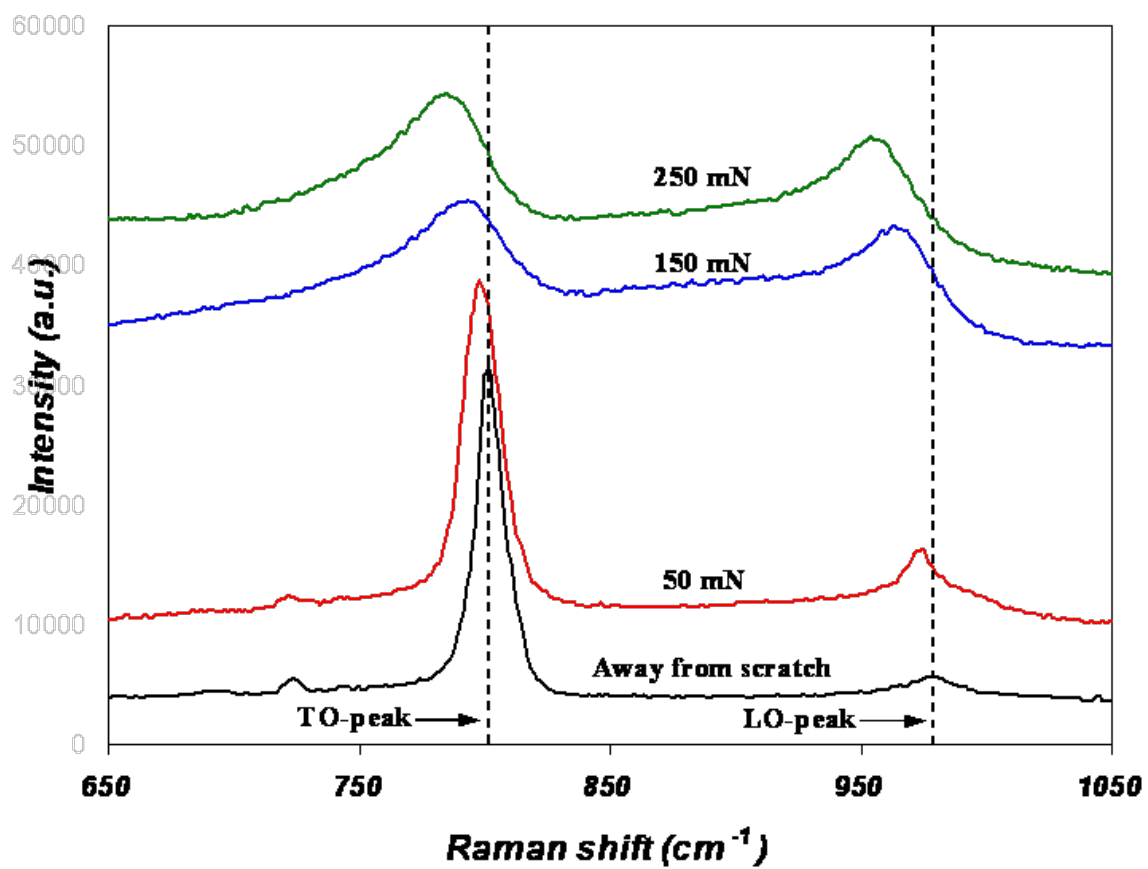


Figure 4-15. Raman spectra collected from the SiC grains present within and away from the scratch grooves.

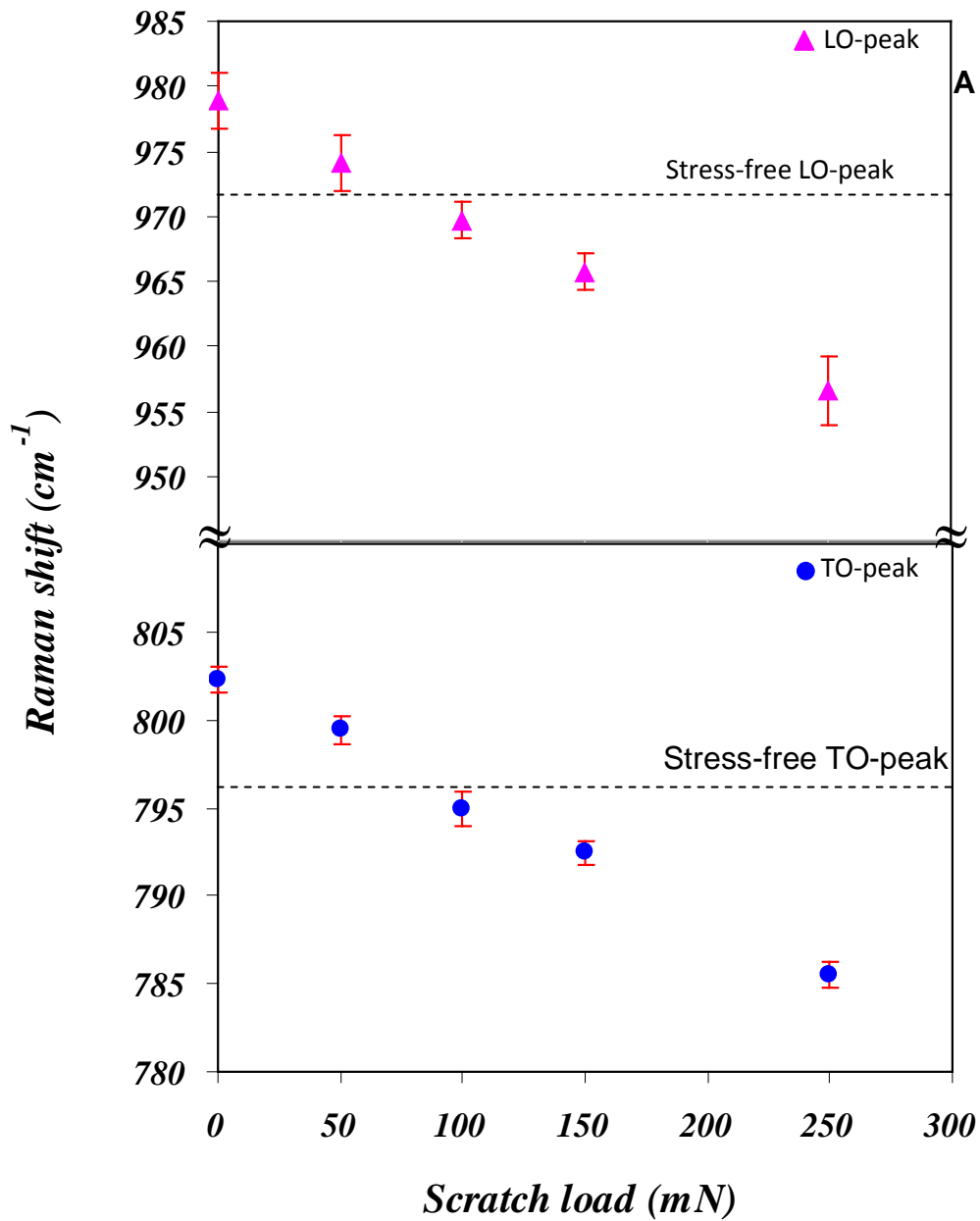


Figure 4-16. A) LO- and TO-Raman peak positions of SiC grains within the scratch grooves at 50, 100, 150 and 250 mN loads. LO- and TO-peak positions at 0 mN correspond to the Raman spectra collected from SiC grains outside the scratch groove. B) Changes in peak positions to stress-free LO- and TO-positions.

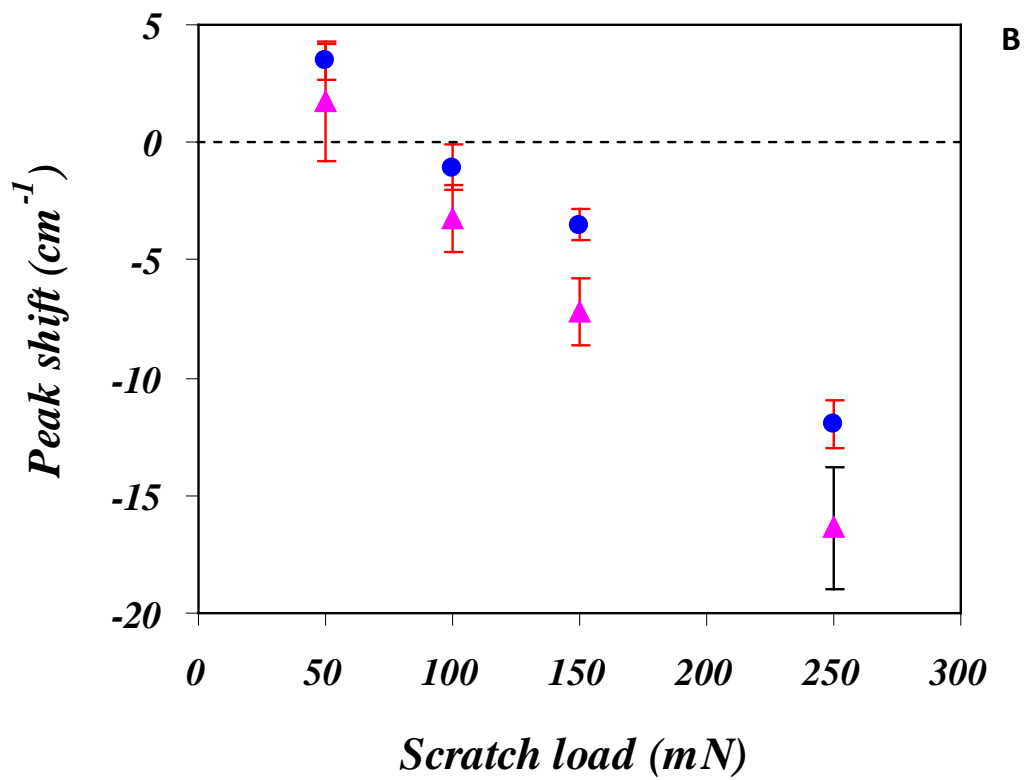


Figure 4-16. Continued

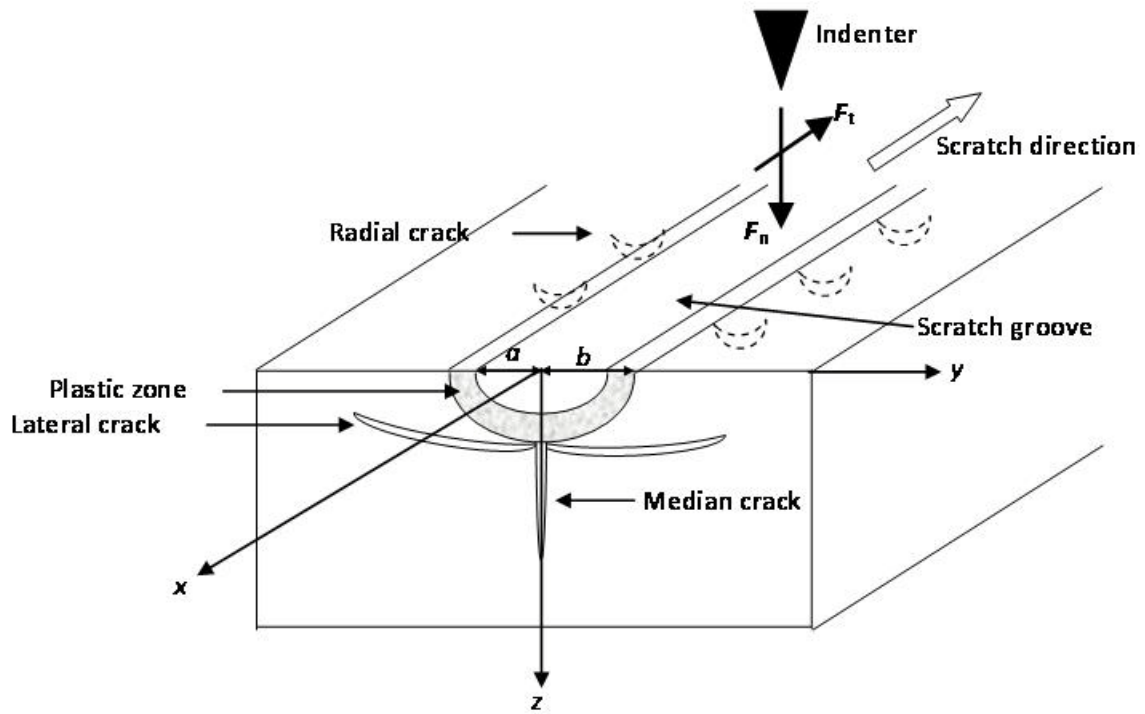


Figure 4-17. Schematic of the scratch process and different crack systems that evolve during the scratch process are shown.

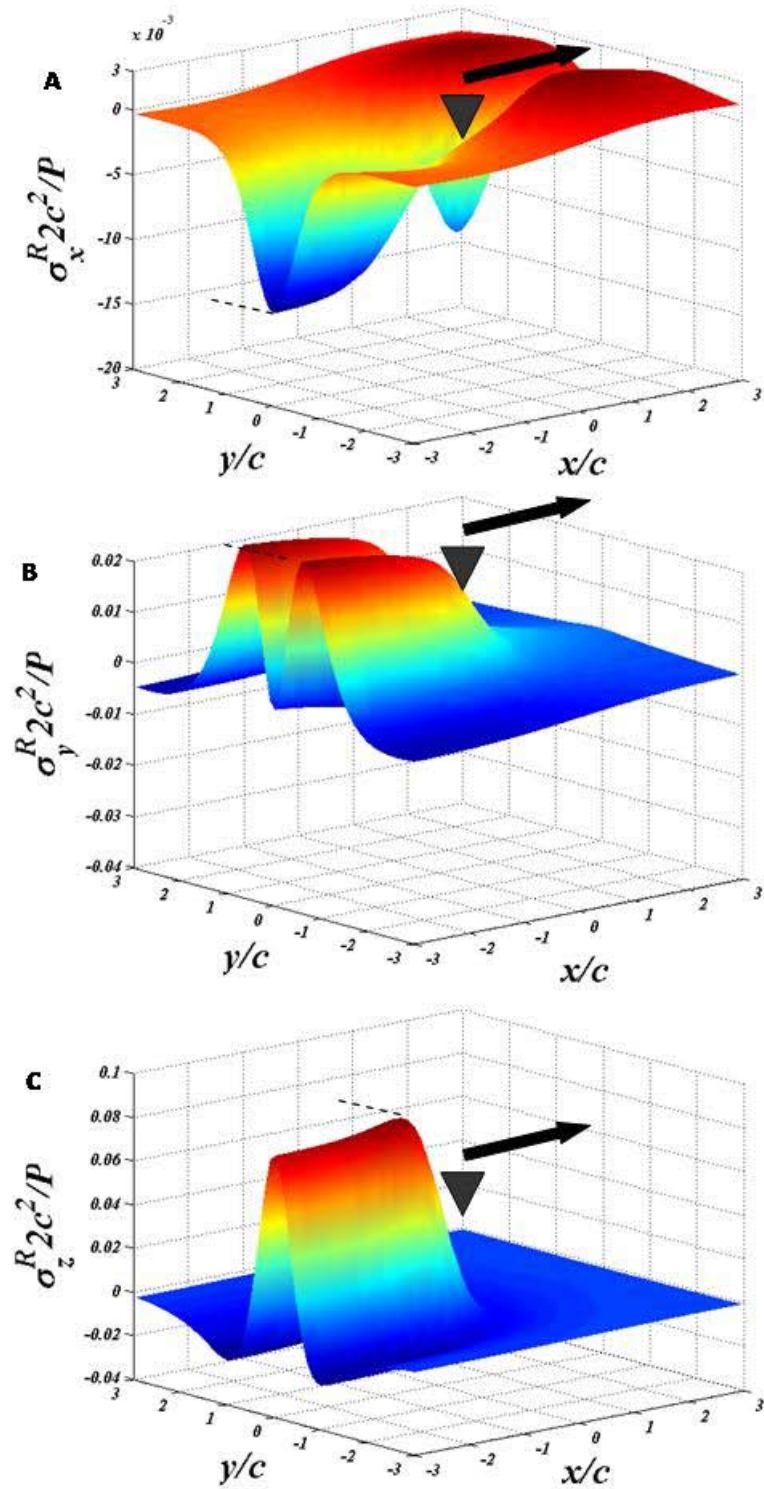


Figure 4-18. Distribution of normalized residual stress components; A) σ_x^R , B) σ_y^R and C) σ_z^R on the x-y plane ($B/P = 0.005$). The black triangle indicates the position of the indenter whereas the black arrow indicates the scratch direction.

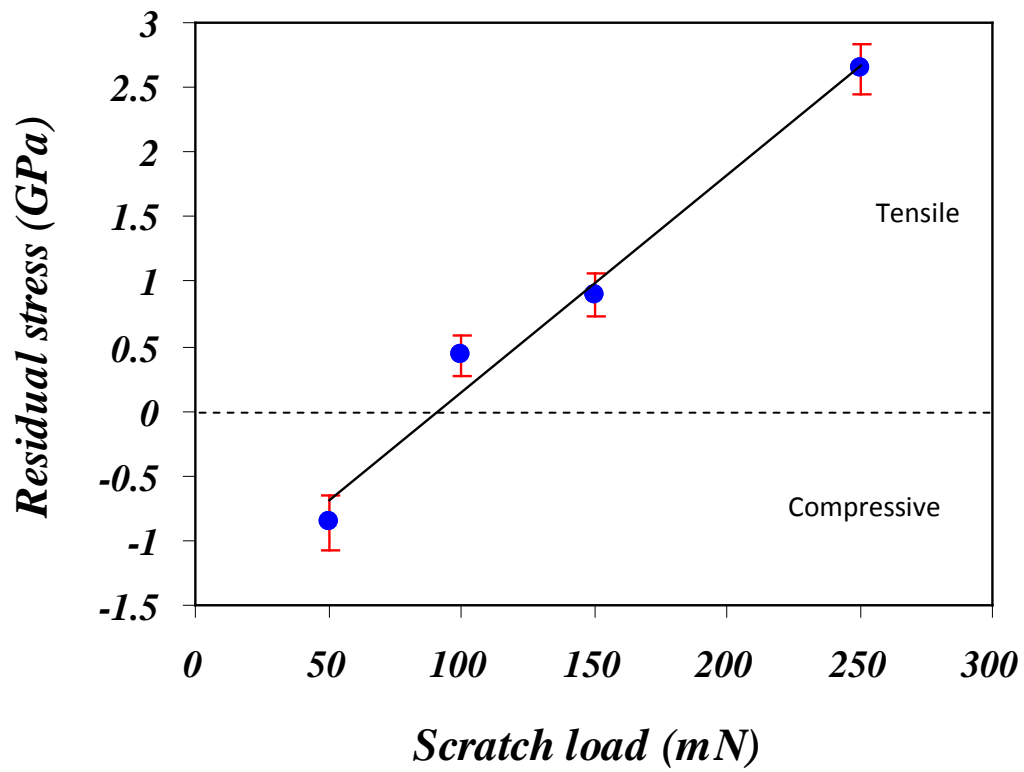


Figure 4-19. Evolution of residual stress within SiC grains as a function of scratch load.

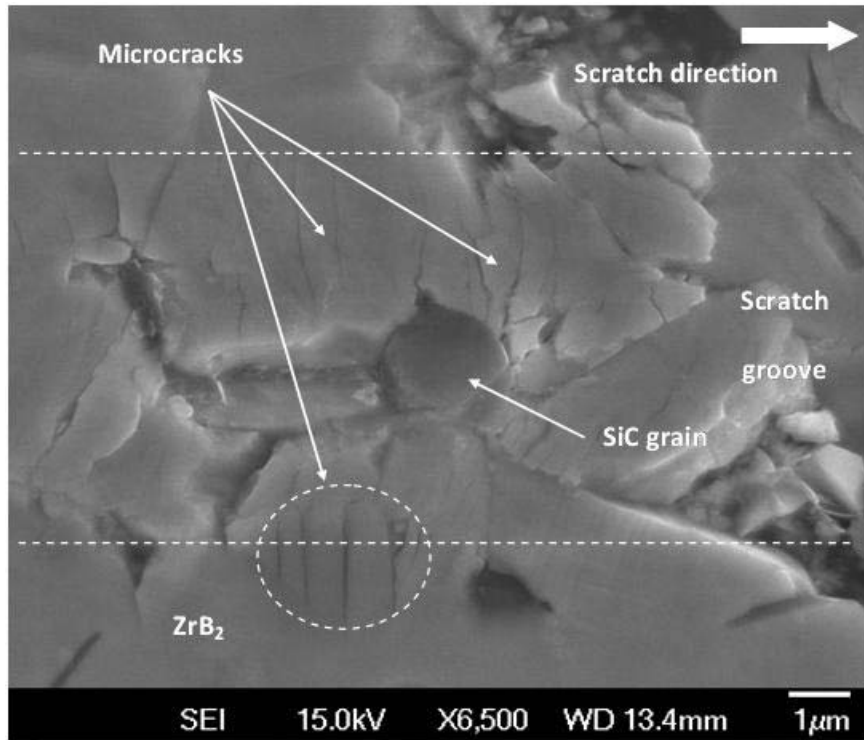


Figure 4-20. SEM micrograph of a scratch groove at 250 mN revealing the uncracked SiC grain surrounded by the heavily microcracked ZrB₂ matrix.

Table 4-1 Material properties

Material	E (GPa)	α (K^{-1})	ν	Volume fraction (%)
ZrB ₂	489 ²	$5.9 \times 10^{-6(2)}$	0.16 ²	~ 91
SiC	694 ¹⁹⁴	$3.5 \times 10^{-6(195)}$	0.17 ¹⁹⁶	~ 9

CHAPTER 5 ROOM-TEMPERATURE DISLOCATION ACTIVITY IN UHTCS

5.1 Introduction

In Chapter 4, it has been shown that during scratch studies at room-temperature readily detectable metal-like plastic deformation patterns called slip-lines, uncharacteristic of hard ceramics, were observed in a polycrystalline zirconium ZrB_2 -5wt%SiC composite.⁷² Similar features were also noted from indentation experiments studies in ZrB_2 and hafnium diboride (HfB_2) ceramics.²¹¹ Figures 5-1 (A) and 5-1 (B) reveal optical micrographs (in Nomarski illumination) of intense slip-line or surface-step formation in the vicinity of indented regions in a polycrystalline ZrB_2 and a polycrystalline HfB_2 ceramics, respectively. Slip-line features were also observed in the SEM micrograph as shown in Fig. 5-1 (C) for the HfB_2 ceramic which are similar to those formed in ZrB_2 as shown in Chapter 4. Such macroscopic slip-steps are clear evidence of dislocation-induced plastic deformation and dislocation mobility at room-temperature in these ultra high-temperature ceramics. At elevated temperatures dislocation assisted plastic deformation is expected to play a significant role in mechanical deformation compared to room-temperature. Therefore, it is important to investigate the nature of dislocations in these materials induced during mechanical deformation.

Owing to the extremely high melting temperature of UHTCs as well as high covalent character in chemical bonding, such plastic behavior is unexpected.²¹² Except the transmission electron microscopic (TEM) observation by Haggerty and Lee¹⁵⁹ on the deformed regions of ZrB_2 single crystals, dislocations have never been identified either in polycrystalline ZrB_2 or in HfB_2 ceramics. Therefore,

in this work, employing TEM, the room-temperature dislocation activity responsible for the observed slip-lines in ZrB₂ ceramics has been investigated. Also, the possible slip systems activated during the mechanical deformation have been identified. Then, an attempt has been made to build up an understanding on the origin of room-temperature dislocation mobility in ZrB₂ ceramics from crystal structure and chemical bonding perspectives.

5.2 Experimental

For identification of deformation features at a finer scale, transmission electron microscopy (TEM) was performed. A site specific cross sectional FIB (FEI Strata DB235) technique²¹³ was employed to prepare TEM specimens from the low-velocity scratch grooves. These grooves were chosen because of the availability of larger smooth areas containing slip-lines in the vicinity of scratches. The FIB technique employs a focused Gallium ion (Ga⁺) beam to prepare a thin TEM specimen of < 200 nm thickness (of approximate dimensions 15μm × 6μm) from the target material through sputtering action. Here a “lift-out” technique²¹³ was used where an electron transparent thin specimen is cut-out from the bulk material and analyzed directly in TEM.

First the area of interest (i.e., the region within a scratch groove containing large number of slip-lines) was protected from any potential damage from the Ga⁺ ion beam by depositing a thin layer of platinum (Pt). Then, progressively deeper trenches were cut on either side to form a thin specimen as shown in Fig. 5-2 illustrating a FIB-cut transverse cross-sectional sample within a constant load scratch groove of 250 mN. The specimen was then cut through the depth on two

ends (where the specimen is attached to the bulk of the material) so as to relax the residual stress (without cracking) which had developed as a result of elastic-plastic deformation during the scratch process. The beam current was then reduced and milling was performed on both sides of the sample until thinned down to thickness of about 200 nm. The specimen was set free from the scratch groove and analyzed in a TEM (JEOL 200CX).

5.3 Results and Discussion

The TEM investigations revealed high density of dislocations within the deformed ZrB_2 grains in the regions directly beneath the scratch groove. A low magnification bright-field image of the TEM specimen is shown in Fig. 5-3 (A) where as Fig. 5-3 (B) presents a high magnification bright-field TEM image, at $[0001]$ zone, of a selected area from Fig. 5-3 (C) revealing highly deformed region beneath the scratch groove. Clearly, the TEM micrograph revealed dense dislocation activity and clustering within the deformed ZrB_2 grains. Dislocations in three different orientations were clearly visible, suggesting slip on multiple planes. Similarly, multiple and intersecting slip-bands were observed at a macroscopic scale on the deformed surfaces, see Fig. 5-3 (C). These dislocations and slip bands, observed from the TEM and SEM images, respectively, appear to be at an orientation of approximately 60° to one another.

At $[0001]$ zone axis, the diffraction pattern contains three prismatic \mathbf{g} vectors, $(10\bar{1}0)$, $(\bar{1}100)$ and $(01\bar{1}0)$. It should be noted here that the $\langle 11\bar{2}0 \rangle$ type directions are the closest-pack directions contained within the $\{10\bar{1}0\}$ type prismatic planes, $\{10\bar{1}1\}$ type pyramidal planes and (0001) basal plane. Also,

these directions are oriented 90° from the poles of these prismatic, pyramidal and basal planes. However, such intersecting dislocations at $[0001]$ zone axis and their three-fold symmetry suggested prismatic or pyramidal slip in ZrB_2 during mechanical deformation.

To distinguish between prismatic and pyramidal slip, a simple two-beam analysis as described in the following was performed. These three sets of dislocations observed at $[0001]$ zone axis were imaged in two-beam condition with prismatic \mathbf{g} vectors. If the dislocations are of prismatic type, then one of the sets of dislocations will go out of contrast for each of these three diffracting conditions due to $\vec{\mathbf{g}} \cdot \vec{\mathbf{b}} = 0$. Geometrically, this means that the direction of Burgers vector must lie in the plane responsible for the operating reflection. Therefore, pole of the plane will be perpendicular to the direction of Burgers vector. For example, pole of the $(1\bar{1}0\ 0)$, $(\vec{\mathbf{g}})$, plane is perpendicular to the $[11\bar{2}0]$, $(\vec{\mathbf{b}})$, direction (closest-pack direction). Therefore, $\vec{\mathbf{g}} \cdot \vec{\mathbf{b}}$ will be zero. In contrast, if the dislocations are of pyramidal type, then all these three sets of dislocations will remain in contrast when imaged with prismatic \mathbf{g} vectors $\vec{\mathbf{g}} \cdot \vec{\mathbf{b}} \neq 0$. In the current work, it was indeed observed that one of the three sets of dislocations was always out of contrast for each of the three diffracting conditions with prismatic \mathbf{g} vectors i.e., $\vec{\mathbf{g}} \cdot \vec{\mathbf{b}} = 0$. These observations suggested prismatic slip within ZrB_2 grains. As mentioned before that $\langle 11\bar{2}0 \rangle$ type of directions are the closest-pack directions, therefore, it was inferred that Burgers vectors of these dislocations are parallel to the $\langle 11\bar{2}0 \rangle$ directions. In ZrB_2 crystal, $[0001]$ is also a possible close-pack direction as the c/a ratio in ZrB_2 is 1.114. However, the

possibility of $[0001]$ as the Burgers vector for these three sets of dislocations observed at $[0001]$ was excluded since these dislocations were clearly visible at $[0001]$ zone axis, see Fig. 5-3 (A). Thus, $\{10\bar{1}0\} \langle 11\bar{2}0 \rangle$ slip system was inferred in this ceramic.

The TEM investigations also revealed another slip system less commonly reported in HCP materials [161]. Figure 5-4 (A) and Fig. 5-4 (B) reveal a bright-field image of dislocations, at $[\bar{1}2\bar{1}0]$ zone axis, and the corresponding selected area electron diffraction pattern, respectively. Burgers vector of these dislocations was determined in the following way. For this set of dislocations, however, Burgers vector cannot be of $[\bar{1}2\bar{1}0]$ type, closest-pack direction in ZrB_2 , (as was observed for the set of dislocations in Fig. 5-3 (B)) or parallel to this direction. If the Burgers vector of a set of dislocations is parallel to a zone axis, then those dislocations will be invisible at that zone axis. This is because all the planes at the zone contains the zone axis direction (or parallel) and therefore, for all the \mathbf{g} vectors at the zone, $\vec{\mathbf{g}} \cdot \vec{\mathbf{b}} = 0$ will be zero. Since the dislocations shown in Fig. 5-4 (A) were visible at $[\bar{1}2\bar{1}0]$ zone axis, their Burgers vector cannot be parallel to this orientation, for they would be invisible.

$[\bar{1}2\bar{1}0]$ zone contains (0001) , $(10\bar{1}0)$ and $(10\bar{1}1)$ reciprocal lattice vectors (\mathbf{g}), corresponding to basal, prismatic and pyramidal planes, respectively. Contrast experiments revealed that these dislocations (as seen in Fig. 5-4 (A)) remained in contrast when imaged with (0001) and $(10\bar{1}1)$ \mathbf{g} vectors. For example, Fig. 5-4 (C) shows a bright-field image of the dislocations (seen in Fig. 5-4 (A)) imaged in two-beam condition with (0001) \mathbf{g} vector. That is for (0001)

and $(10\bar{1}1)$ \mathbf{g} vectors, $\vec{\mathbf{g}} \cdot \vec{\mathbf{b}} \neq 0$. This excluded the possibility of $\{0001\} \langle 11\bar{2}0 \rangle$ basal slip in ZrB_2 . This is because for basal slip, $\vec{\mathbf{g}} \cdot \vec{\mathbf{b}}$ will be zero with (0001) \mathbf{g} vector and dislocations will be invisible in two-beam condition. On the other hand, these dislocations were completely invisible when imaged with $(10\bar{1}0)$ \mathbf{g} vector. As discussed above, $[\bar{1}2\bar{1}0]$ direction was excluded as the Burgers vector. Since the only other low-index direction perpendicular to the pole of $(10\bar{1}0)$ plane is $[0001]$, the above contrast experiments suggested that the Burgers vector is parallel to $[0001]$. For further confirmation, the same set of dislocations was imaged with a $(11\bar{2}0)$ \mathbf{g} vector (in $[\bar{1}100]$ zone) because $\{11\bar{2}0\}$ type of planes (secondary prismatic type) only contain $[0001]$ Burgers vector. It was observed that these dislocations went completely out of contrast when imaged with $(11\bar{2}0)$ \mathbf{g} vector in two-beam condition. Therefore, the same set of dislocations was completely invisible when imaged with $(10\bar{1}0)$ and $(11\bar{2}0)$ \mathbf{g} vectors. The only direction which is contained by $(10\bar{1}0)$ and $(11\bar{2}0)$ planes is $[0001]$. Both the $(10\bar{1}0)$ and $(11\bar{2}0)$ \mathbf{g} vectors will dot to zero with $[0001]$ vector. Therefore, it was concluded that Burgers vectors are parallel to $[0001]$ direction. This Burgers vector has never been reported in open literature for ZrB_2 ceramics.

For dislocations with Burgers vector parallel to $[0001]$, the only possible close-pack slip-plane is of prismatic type, either $\{10\bar{1}0\}$ or $\{11\bar{2}0\}$. The $\{10\bar{1}0\}$ primary prismatic planes have a higher planer density (0.727) compared to that (0.682) of the $\{11\bar{2}0\}$ secondary prismatic planes. Thus, $\{0001\} [0001]$ is the most probable slip system compared to $\{11\bar{2}0\} [0001]$ in ZrB_2 . However, due to nearly comparable packing density of the primary and secondary prismatic

planes, slip may also occur on the $\{11\bar{2}0\}$ planes. Nevertheless, the current TEM investigations clearly revealed prismatic slip as the only identified room-temperature plastic deformation mechanism in polycrystalline ZrB_2 . The above TEM studies are also consistent with the work by Haggerty and Lee in ZrB_2 single crystals.¹⁵⁹

There is also considerable evidence^{214,215} supporting that prismatic slip is favored over basal slip in ZrB_2 . Xuan et al.,²¹⁴ performed Vickers microhardness measurements in ZrB_2 single crystals, on basal, (0001) and prismatic planes, $\{10\bar{1}0\}$ and $\{11\bar{2}0\}$, from room temperature to 1000°C. It was observed that over the entire temperature range, hardness was same on both types of prismatic planes but was lower than that on the basal plane. A similar result was also obtained in the work of Nakano et al.²¹⁵. When a basal plane is indented, only possible slip planes are pyramidal planes. On the other hand, indentation on $\{10\bar{1}0\}$ and $\{11\bar{2}0\}$ planes can cause slip on other prismatic planes from $\{10\bar{1}0\}$ and $\{11\bar{2}0\}$ families as well as on pyramidal planes. Therefore, it is clear that in ZrB_2 prismatic slip is more favorable. The work of Xuan et al.,²¹⁴ and Nakano et al.,²¹⁵ also suggested that dislocation motion is probably equally favorable on both $\{10\bar{1}0\}$ and $\{11\bar{2}0\}$ prismatic planes. The current TEM investigation clearly revealed that prismatic slip was the only identified mechanism responsible for room temperature plastic deformation in polycrystalline ZrB_2 .

Having determined the nature of dislocations, in the following, it has been attempted to rationalize the room-temperature dislocation activity and mobility based on the properties, crystal structure, and chemical bonding present in these

ceramics. The nature of chemical bonding plays a dominant role in governing the properties of metals and ceramics. In general, the non-metallic character of bonding (mainly covalent) in structural ceramics is well reflected in their properties through high elastic modulus, chemical stability at room and high temperatures, extremely low electrical conductivity, and thus, corresponding high electrical resistivity in comparison to metals.²¹⁶ In contrast, UHTCs have a unique combination of properties which are characteristics of both metals and ceramics.² As mentioned before, their high melting temperature ($> 3000^{\circ}\text{C}$), high elastic modulus ($> 400 \text{ GPa}$) and superior thermo-chemical stability are typical of ceramics. In addition, UHTCs have surprisingly high electrical conductivity ($> 10^6 \text{ S/m}$) and thus, low electrical resistivity ($< 10^{-5} \text{ Ohm-cm}$), comparable to those of metals.^{2,217-225} These values are in contrast to the typical structural ceramics such as aluminum oxide (Al_2O_3), silicon carbide (SiC), and silicon nitride (Si_3N_4) as illustrated in Fig. 5-5. Such electrical properties are an indication of significant metallic nature (i.e., metallicity) in chemical bonding present in these ceramics.

ZrB_2 and HfB_2 have $A\text{IB}_2$ -type ($P6/mmm$ space group) hexagonal crystal structure² where the unit cell contains a six-member graphite-like ring or a net of boron (B) atoms in two-dimension which alternates with close-packed layers of metal (M) atoms, see Fig. 5-6. Vajeeston et al.,²²⁶ studied electronic structure and nature of chemical bonding in $A\text{IB}_2$ -type ceramics using the self-consistent tight-binding linear muffin-tin orbital (TB-LMTO) method. Zhang et al.,²²⁷ utilized the first principles total-energy plane-wave pseudopotential (PW-PP) method and investigated the electronic structures and elastic properties of ZrB_2 and HfB_2

ceramics. The theoretical analysis of Vajeeston et al.,²²⁶ and Zhang et al.,²²⁷ have revealed the existence of three types of chemical bonds in this crystal structure: (i) B-B, (ii) M-B and (iii) M-M (M=Zr, Hf).^{226,227} While the B-B bonds are purely covalent, the M-B bonds are a mixture of covalent and ionic characters. However, due to small difference in electronegativity values (1.33, 1.30 and 2.04 for Zr, Hf and B, respectively), ionicity is less than 8%. In contrast, the M-M bonds are predominantly metallic due to nearly free-electron non-bonding *d*-orbital states which attribute significant metallicity to these ceramics.^{226,227} Both of these bonds are known to exhibit strong influence on properties of materials. Here, it is argued that such metallic character of chemical bonding in ZrB₂ and HfB₂ ceramics is well reflected in their *metal-like* mechanical deformation behavior observed in indentation and scratch studies, see Fig. 5-1, at room-temperature.^{72,160}

In the following, arguments for the origin of room temperature dislocation mobility in ZrB₂ ceramic, may also be applicable for other TMB₂ ceramics such as HfB₂, are presented. During dislocation motion, chemical bonds constantly distort, break, and reform.^{228,229} The nature of chemical bonding (i.e., how tightly electrons are bound, their directionality, and symmetry) has a strong influence on dislocation mobility for a given crystal structure at room temperature.

Gilman^{228,229} suggested that local or non-local nature of chemical bonding determines mobility at room temperature and proposed a simple but fundamental chemical approach to describe dislocation mobility in pure covalently bonded solids. In this approach, optical band gap, a measure of localized nature of

chemical bonding, is assumed to be related to glide activation energy. In a similar fashion, qualitatively, dislocation mobility can also be correlated to the local or non-local character of chemical bonding in ZrB_2 and in other AlB_2 -type UHTCs as having a mixture of covalent and metallic bonds.^{226,227} Similar to the optical band gap, the electrical conductivity can also reflect the local or non-local nature in chemical bonding. While the exact mechanism of high electrical conductivity in ZrB_2 and HfB_2 ceramics is not known, Zhang et al.,²²⁷ suggested that their unusually high conductive nature is related to the Zr-Zr and Hf-Hf metallic bonding. It is argued that such bonding characteristics can also play a significant role in the room-temperature plastic deformation and the associated dislocation mobility in these ceramics.

One of the reasons why such room-temperature macroscopic plastic deformation features are not readily observed in other structural ceramics (e.g., Al_2O_3 , ZrO_2 , SiC, Si_3N_4) is that they possess strong covalent and ionic bonding instead of direct metal-metal bonds.²³⁰⁻²³³ Direct metal-metal bonding does not exist in these materials. Strong covalent and ionic bonding makes dislocation mobility extremely difficult, particularly at room temperature where availability of thermal energy is low. Dislocation mobility is strongly influenced by the width of a dislocation core which depends on the type of chemical bonding. While metallic bonding results in wide dislocation core, covalent bonding makes it narrow.²³⁰ For wide dislocation core, consisting of non-directional metallic bonds, the energy barrier for dislocation mobility will be lower compared to that of a narrow core structure made up of highly directional covalent bonds.²³⁰ A classic example is

cubic-SiC which has the required number of independent slip-systems to exhibit room temperature plasticity but due to its pure covalent bonding, the width of dislocation core is narrow and thus, dislocations are immobile at room temperature.²³⁰

An accurate description of dislocation core structure and its motion in ZrB₂ (or HfB₂) crystal structure is complex, and requires a fully atomistic approach. However, for a prismatic slip in ZrB₂, the dislocation core structure not only involves B-B and Zr-B bonds but also the Zr-Zr bonds. Existence of metallic bonds can make the dislocation core relatively wider compared to a core made up of only B-B or Zr-B bonds. Thus, the Zr-Zr bonds are assumed to play a crucial role in enhancing the dislocation mobility at room temperature by lowering the chemical barrier. Due to this non-localized nature of Zr-Zr bonds and the associated increased dislocation mobility during mechanical deformation, dislocations are not restricted to a small material volume (typical of ceramics) rather extend over a relatively larger region allowing the dislocation activity to be readily visible even at room temperature at distances further away from the region of load application as seen in Fig. 5-1.

5.4 Conclusions

ZrB₂ and HfB₂ ceramics were observed to exhibit metal-like slip-line patterns at room temperature when deformed by indentations and scratch loads. This deformation pattern indicated significant room temperature dislocation mobility in these ceramics. In-depth TEM analysis in a ZrB₂-SiC composite revealed that dislocations were indeed generated within the ZrB₂ phase as a result of mechanical deformation at room temperature. Prismatic slip was

identified as the major plastic deformation mechanism in polycrystalline ZrB_2 ceramic. Finally, a possible role of Zr-Zr metallic bonds in room temperature dislocation mobility in ZrB_2 ceramics was discussed.

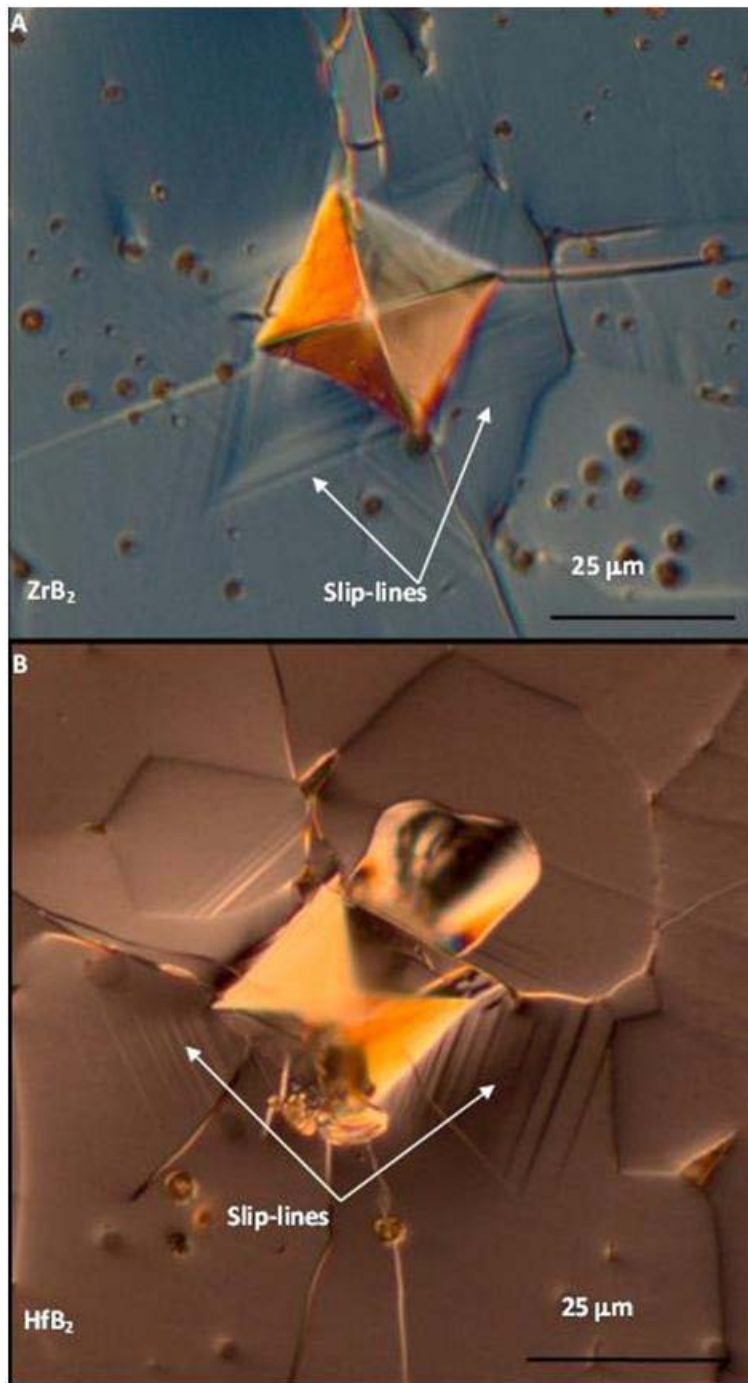


Figure 5-1. Optical micrographs revealing slip-lines formed in the vicinity of indented regions of A) ZrB₂ and B) HfB₂ ceramics.

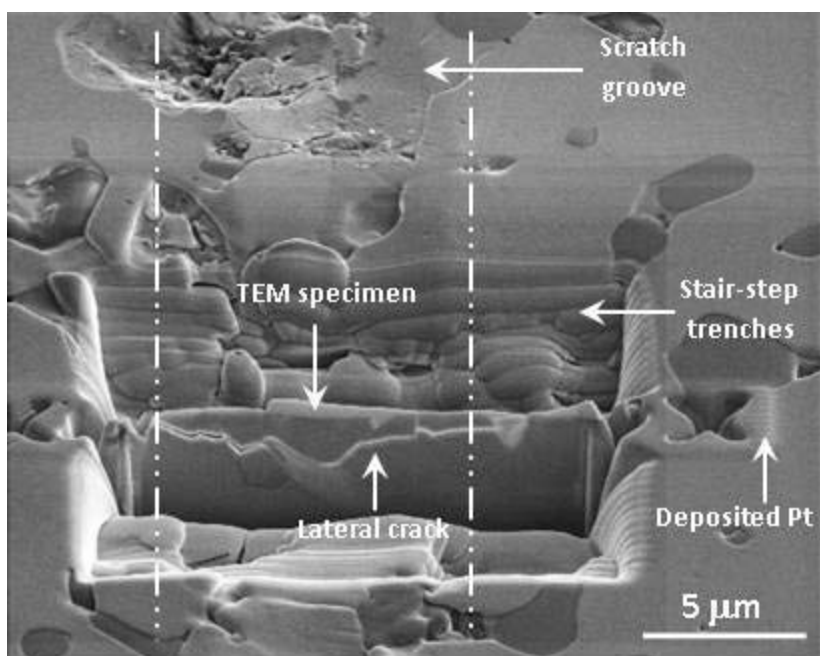


Figure 5-2. FIB-cut TEM specimen within a constant load (250 mN) scratch groove.

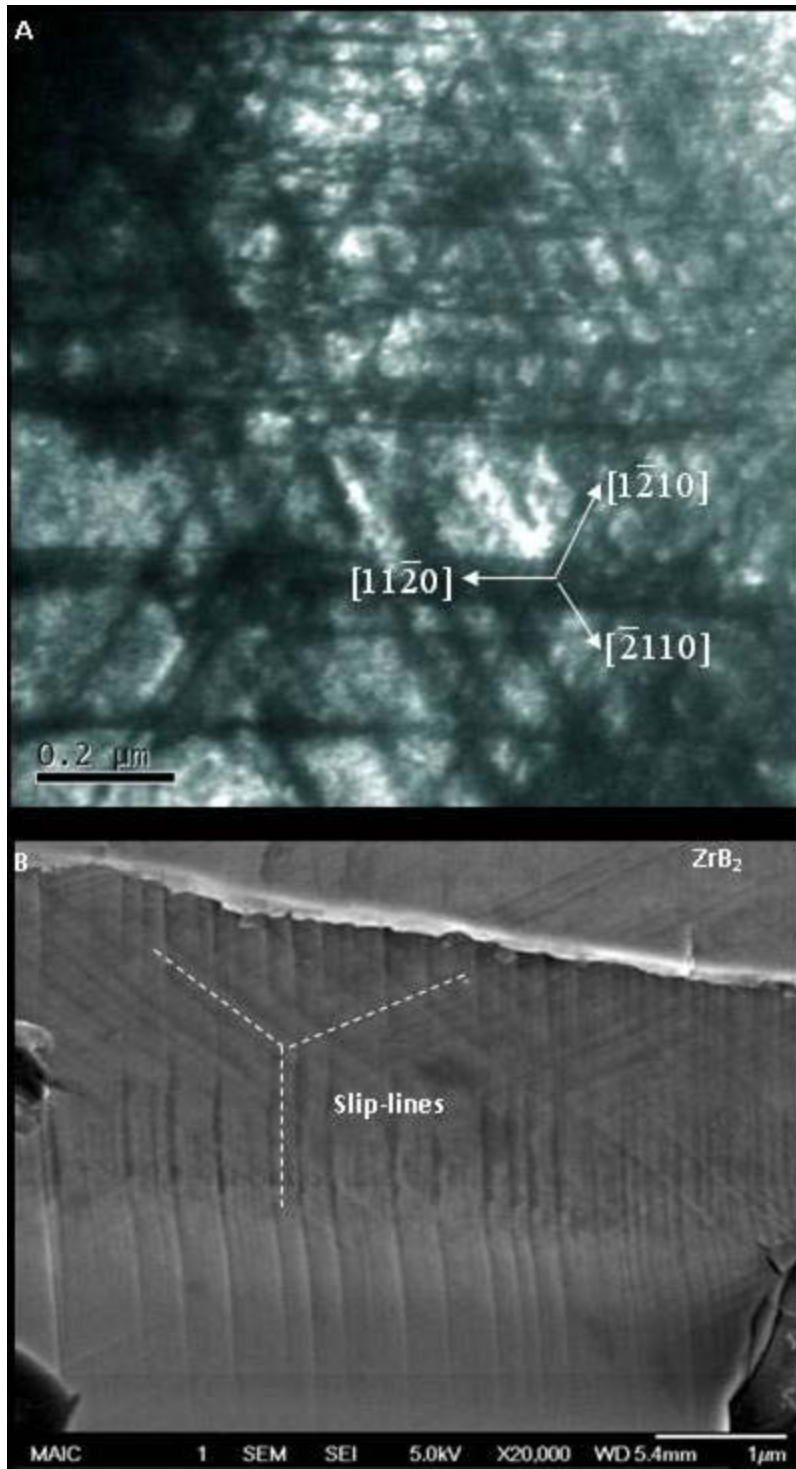


Figure 5-3. A) A bright field TEM micrograph revealing dense dislocation activity on prismatic planes and B) multiple sets of intersecting slip-lines formed on the surface due to scratch load, resembling patterns observed in A).

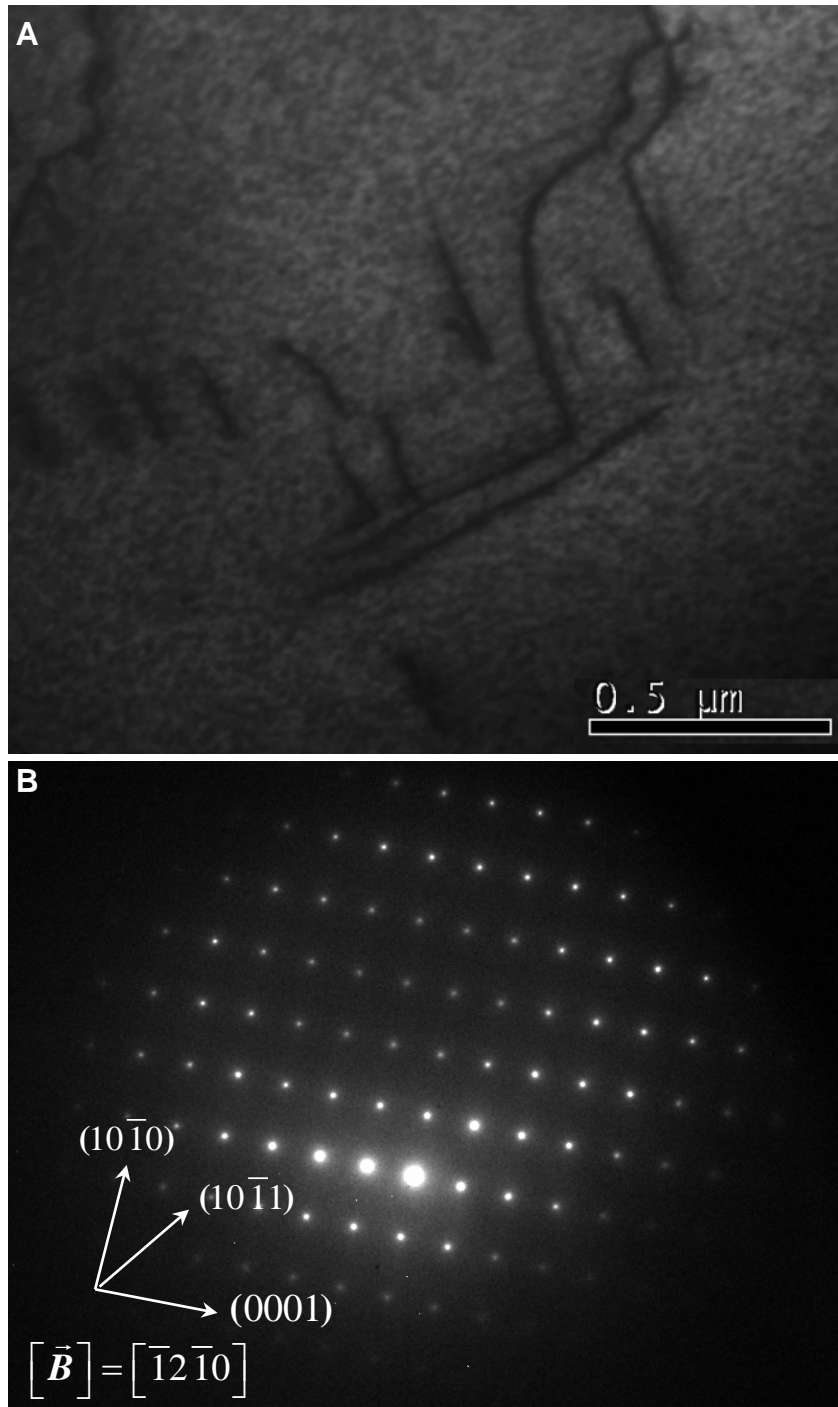


Figure 5-4. A) Bright-field TEM micrograph at $[\bar{1}2\bar{1}0]$ zone axis and B) the corresponding selected area electron diffraction pattern. C) Bright-field TEM image of dislocations in two-beam condition with (0001) \mathbf{g} vector.

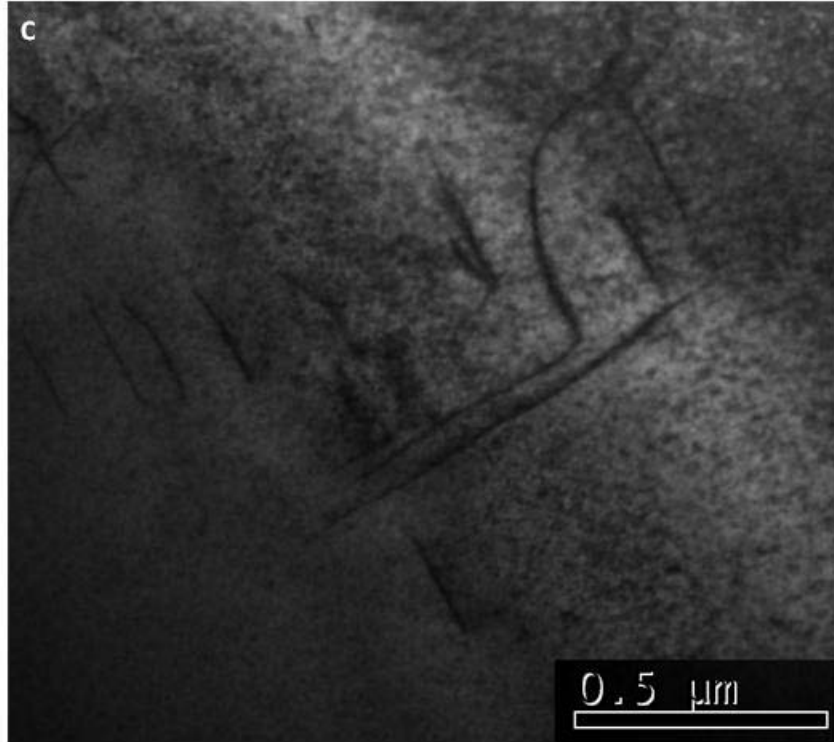


Figure 5-4. Continued

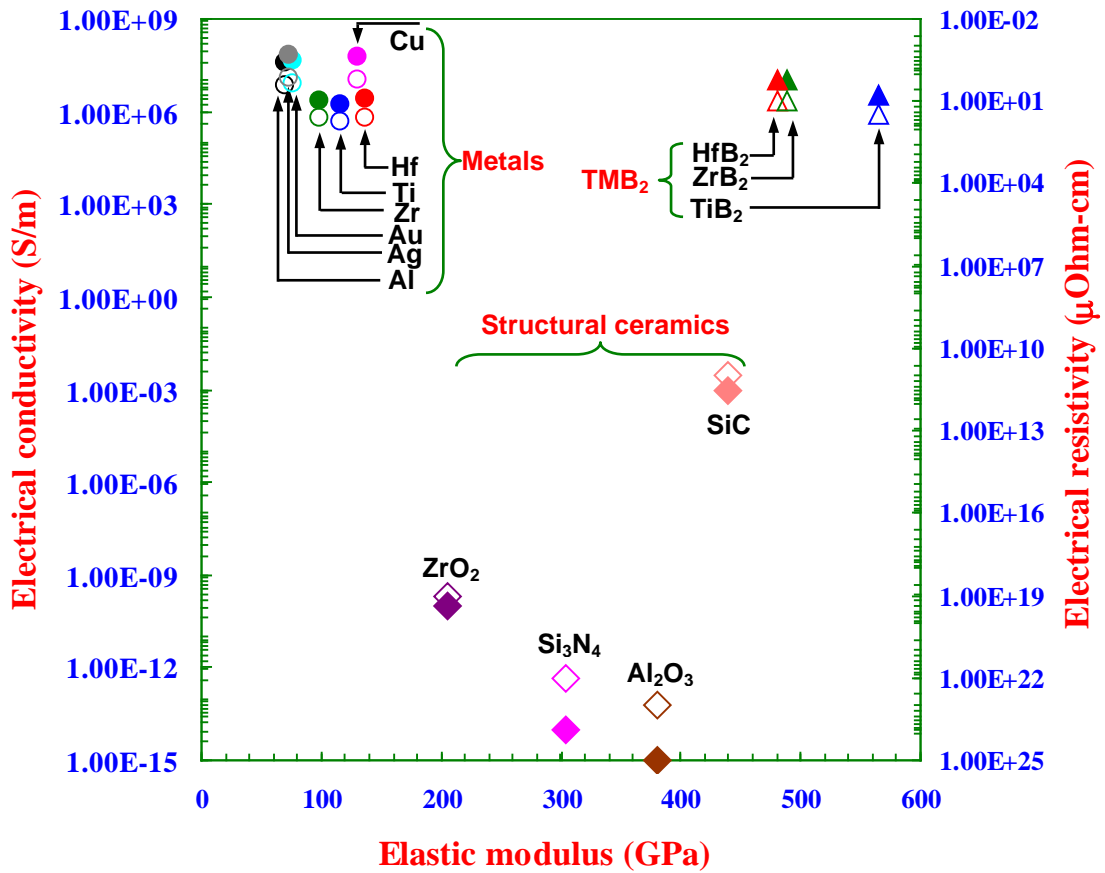


Figure 5-5. Electrical conductivity (filled symbols) and electrical resistivity (open symbols) of metals and ceramics.

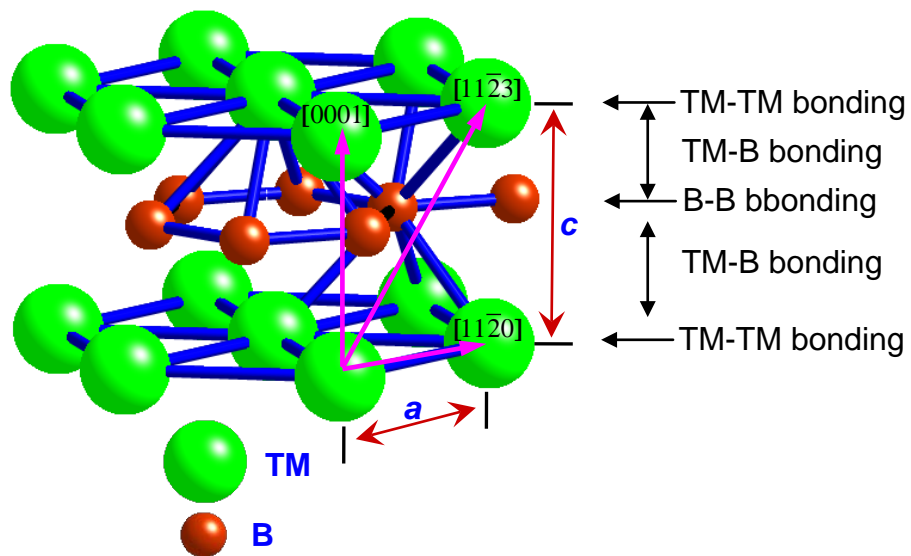


Figure 5-6. Crystal structure of transition metal diborides.

CHAPTER 6 SUMMARY AND FUTURE WORK

6.1 Conclusions

Plasma pressure compaction technique has been utilized to process high-melting point and difficult-to-sinter materials such as boron carbide ceramics⁷¹ and zirconium diboride-silicon carbide composite.⁷² These materials have high covalent bonding characteristics and hence conventional methods which require high sintering temperature and pressure as well as long consolidation times are not suitable to produce dense compacts. In the current work, use of P²C[®] technique successfully produced high density large sintered ceramic compacts at relatively lower temperature, lower compaction pressure, and over a shorter period of time compared to traditional techniques such as pressureless sintering and hot-pressing. Also, it was shown for boron carbide ceramics that grain growth was limited in P²C[®] technique due to lower sintering temperature which aided in the production of fine-grained B₄C ceramics.⁷¹

Boron carbide ceramics with three different grain sizes were subjected to static and dynamic indentation experiments to reveal the influence of grain size and strain rate on mechanical properties. Static indentation experiments were conducted using a traditional Vickers indentation tester where as a dynamic Vickers indentation tester was employed to perform the dynamic hardness measurements. In static indentations load was delivered within a duration of 15 seconds which corresponded to a deformation rate on the order of 10⁻⁵/s. In contrast, dynamic loads were delivered within 100 μs resulting in a deformation rate of approximately 10³/s. It was consistently observed that for all the B₄C ceramics, dynamic hardness and dynamic fracture toughness were lower compared to static hardness and static fracture toughness.⁷¹

To reveal the subsurface region of indentation, bonded interface technique on split specimens was employed. Static and dynamic indentations at similar load levels were then performed along the interface of the bonded specimen. Microstructural investigation of subsurface regions of indentations revealed that dynamic loads resulted in significantly higher damaged regions beneath the indentations compared to the static indentations which are consistent with the hardness and fracture toughness measurements.⁷¹ For further investigations, these subsurface regions of indentations were probed using a series of spectroscopic techniques such as Raman, photoluminescence and infrared spectroscopy. These studies revealed newer peaks from the subsurface damaged regions which indicated that localized phase transformation due to structural changes occurred within these regions.²³⁴ It was also observed that extent of structural changes/disordering was significantly higher in dynamic indentations compared to static indentations. From in-depth analysis of Raman and PL spectroscopy, it was confirmed that amorphous carbon clusters were formed within the indented regions. Also, FTIR analysis revealed the existence of amorphous boron clusters within the dynamically indented region. Thus, the current studies clearly revealed the influence of strain rate on mechanical properties as well as structural changes in boron carbide.

Scratch experiments were performed on a ZrB_2 -5wt%SiC composite to reveal the contact-induced damage and deformation mechanisms which can evolve in this ultra high-temperature ceramic during service. These studies revealed unique metal-like plastic deformation features in terms of slip-lines within the ZrB_2 matrix phase which indicated room-temperature dislocation activity and mobility.^{72,160} Similar deformation

features were also noted from indentation experiments.^{160,211,235} Such room-temperature deformation patterns are highly unusual in ceramics having high melting temperature.²¹² Apart from slip-lines, transgranular microcracks were observed to develop perpendicular to the scratch direction. To rationalize the experimental observations, elastic stress field solutions combining Boussinesq field and Cerruti field solutions for normal and tangential point contact loads, respectively, were utilized. From the elastic stress field distribution, it was shown that as the scratch progresses, considerable amount of shear stress is developed ahead of the indenter tip whereas tensile stress is developed in the wake of the indenter. Also, the maximum principal normal tensile stress was oriented in the direction of scratch. Thus, it was concluded that the shear stress ahead of the scratch tool resulted in slip-line formation whereas the normal tensile stress in the wake of the scratch resulted the orthogonal microcracks (with respect to the scratch direction).⁷² The stress analysis also confirmed that the slip-lines were formed first followed by microcracking.

Deformation-induced residual stress is detrimental to any brittle materials and the magnitude of residual stress may increase as the deformation progresses. Towards this end, an analytical model was developed which can calculate scratch-induced residual stress from the Raman spectroscopic measurements.²³⁶ This analytical framework was developed by combining the well-known 'secular' equation for diamond-like or zinc-blende crystal structure and the concept of 'blister' field solutions. In this framework, residual stress is calculated from the Raman peak shift using phonon deformation potentials of a material. This model is applicable to materials having diamond-like or zinc-blende crystal structure. In the current work, this model was applied to the SiC

particulate phase of the composite which has zinc-blende crystal structure (3C-SiC) and the residual stress was calculated.²³⁶ Raman spectra were collected from the SiC grains residing within and outside of the scratch grooves. It was observed that the characteristic Raman peaks of 3C-SiC gradually shifted to the lower wave numbers with increasing scratch load indicating accumulation tensile residual stress. The measurements revealed that initially residual stress within the grains in the composite (outside of scratch groove) was compressive and gradually became tensile within increasing scratch load.²³⁶

Existence of dislocations within the ZrB₂ phase was confirmed through transmission electron microscopic analysis of deformed regions within the scratch grooves.^{160,211} Prismatic slip was identified as the plastic deformation mechanism in polycrystalline ZrB₂. It was argued that similar to having extremely high electrical conductivity which is comparable to metals, formation of typical metal-like plastic deformation features at room-temperature was also a reflection of metallicity present in chemical bonding in these ceramics. In this context, a possible role of Zr-Zr metallic bonds, present in the ZrB₂ crystal structure, which can favor dislocation mobility at room-temperature has been discussed.²¹¹

In conclusion, two major findings can be drawn from this thesis: (i) development of a simple technique that can induce structural changes in B₄C ceramics and similar to that observed in ballistically investigated ceramic tiles, and (ii) presence of unequivocal evidence for room-temperature dislocation mobility in UHTCs.

6.2 Future Work

6.2.1 Determination of Transition Point of Phase Transformation in B₄C

In this dissertation, it has been shown that localized phase transformation or structural changes occurred during static and dynamic indentations. However, the question still needed to be answered is that if there a transition point in terms of indentation load or velocity or pressure, when the transformation initiates. Also, there are several factors such as microstructure, composition, and presence of graphite phase may have an influence on the extent of phase transformation. However, the use of extremely sharp indenters such as Berkovich and Vickers results in high enough pressure even at a low load to trigger localized phase transformation or structural disordering. Instead, use of spherical indenters with different tip radii can be helpful in capturing a possible existence of transition point for solid-state phase transformation in B₄C as a function of load, indenter velocity, etc.

6.2.2 Scratch Response of Oxidized Surfaces of ZrB₂-SiC Composite

It has been shown that the surface morphology of ZrB₂-SiC composite changes with temperature due to oxidation of both the phases.^{2,37-40} In the temperature range of 800 - 1200°C, oxidation rate of ZrB₂ is higher than that of SiC. ZrB₂ produces molten B₂O₃ (melting point ~ 450°C) and crystalline ZrO₂ at 1000°C. This process results in a porous layer of crystalline ZrO₂ and SiC above the unoxidized ZrB₂-SiC composite. Thus, above 1000°C, the oxidized surface of the ZrB₂-SiC composite consists of a porous ZrO₂+SiC layer covered by a thin B₂O₃ amorphous layer.³⁷⁻⁴⁰ At this temperature range, further oxidation of unreacted ZrB₂, present below the porous ZrO₂+SiC layer, is controlled by the diffusion of oxygen (O₂) through the thin glassy layer of B₂O₃. Figures 6-1 (A), 6-1 (B) and 6-1 (C) show the cross-sectional areas of the ZrB₂-5wt%SiC

specimens oxidized at 1000°C in ambient conditions for 1, 5 and 15 hours, respectively. It can be seen from Fig. 6-1 that upon oxidation different layers were formed from the top. As the oxidation time increases total thickness of the oxidized layers also increases. Surface morphology of ZrB₂-SiC composite also changes as the temperature increases. At temperatures above 1200°C, the upper B₂O₃ layer starts to volatilize (i.e., B₂O₃(l) → B₂O₃(g)) and oxidation of SiC results a thin SiO₂-rich layer (it may also contained some B₂O₃ due to incomplete evaporation or continued oxidation of ZrB₂) above the porous ZrO₂ layer. Above 1400°C, the thickness of the outer SiO₂ layer increases while the B₂O₃ content composition of reduces significantly. Clearly, at this temperature, the structure and the oxidized surface layer is considerably different than that at lower temperatures.³⁷⁻⁴⁰ For example, Fig. 6-2 shows a schematic of the cross-section of ZrB₂-SiC specimen oxidized at 1500°C.

Thus, it is clear that the composition and morphology of the oxidized surfaces change with temperature. Recall that these ZrB₂-SiC composites are used as thermal protection systems for leading edges and nose cones of hypersonic vehicles, and re-entry vehicles which are subjected to intense erosion upon re-entry.² Presence of outer porous layers of different compositions can drastically affect the overall mechanical response of the structure. Also, the thickness of the oxidized layers will vary with oxidation time. Therefore, it is also important to investigate the influence of oxide layer thickness on the wear properties. Therefore, future work should focus first on developing oxidized surfaces at different temperatures and at different oxidation times. Then these surfaces should be subjected to scratch studies to investigate wear properties of ZrB₂-SiC composites.

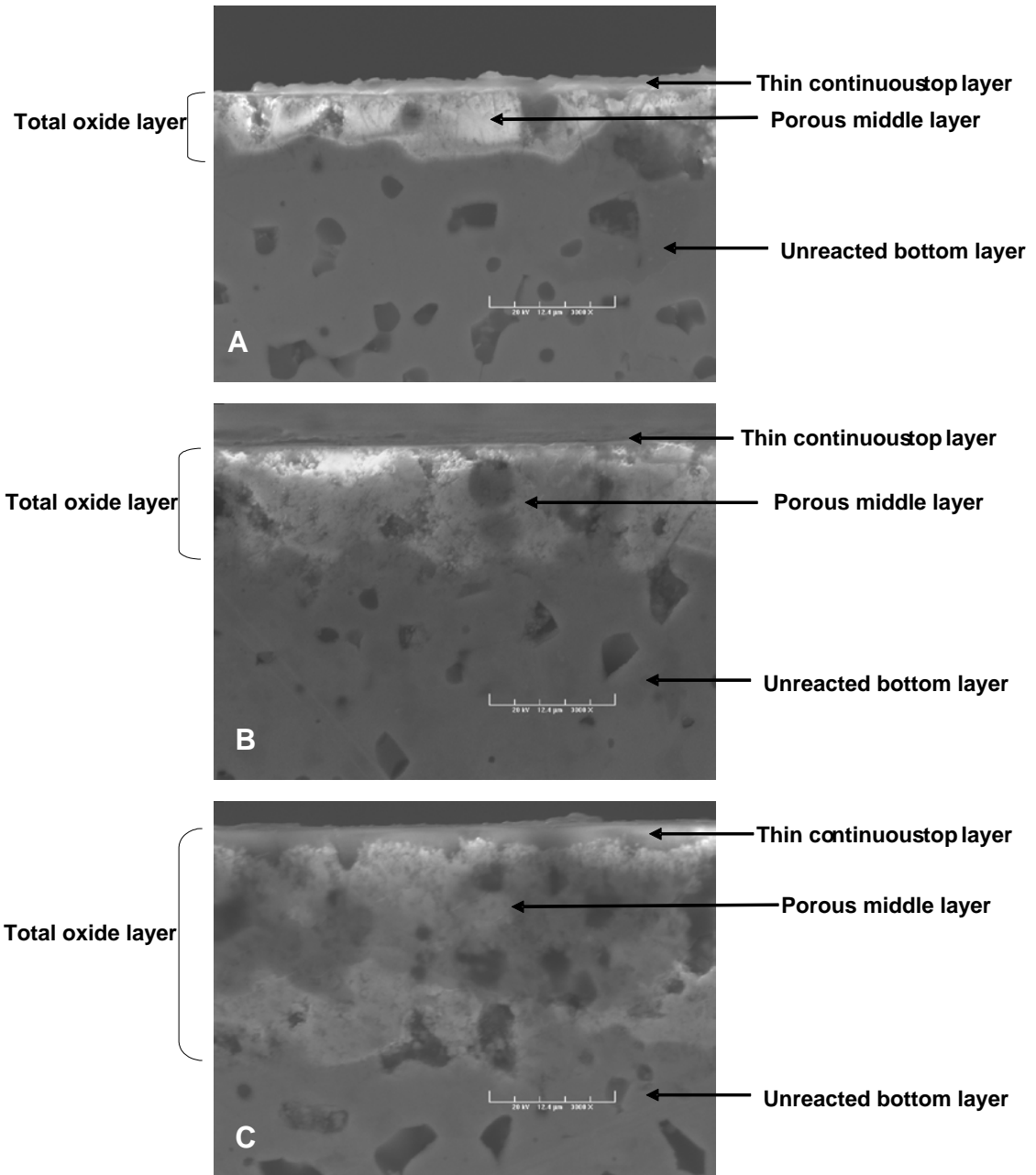


Figure 6-1. Cross-sectional areas of the ZrB₂-5wt%SiC specimens oxidized for A) 1 B) 5 and C) 15 hours.

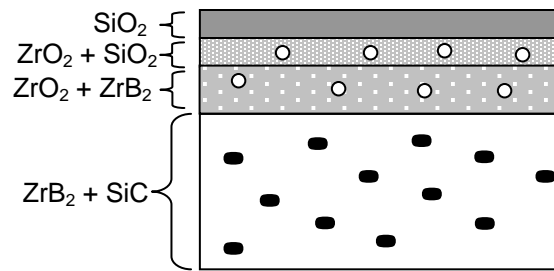


Figure 6-2. Evolution of structures in a ZrB_2 -SiC composite during oxidation at 1500°C .

APPENDIX
DYNAMIC INDENTATION RESPONSE OF B₄C CERAMICS

Figures A-1 and A-2 show the plots of c vs. P and l vs. P for dynamic indentations, respectively.

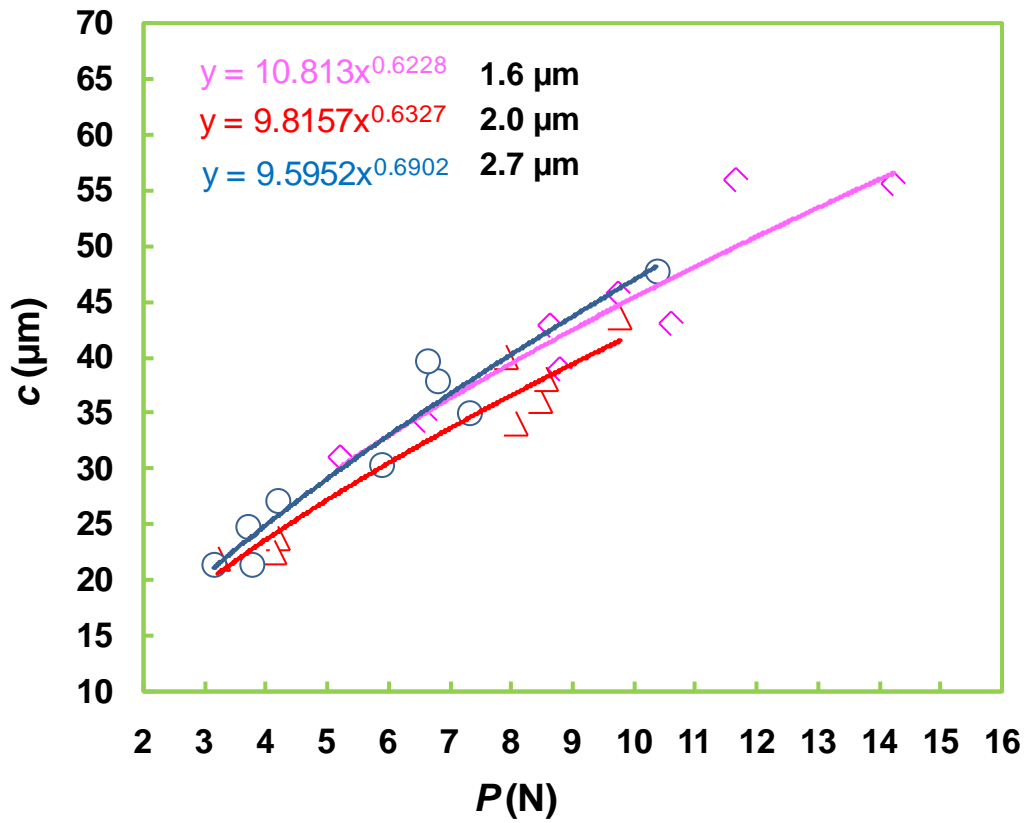


Figure A-1. Variation of c vs. P in B₄C ceramics for dynamic indentations.

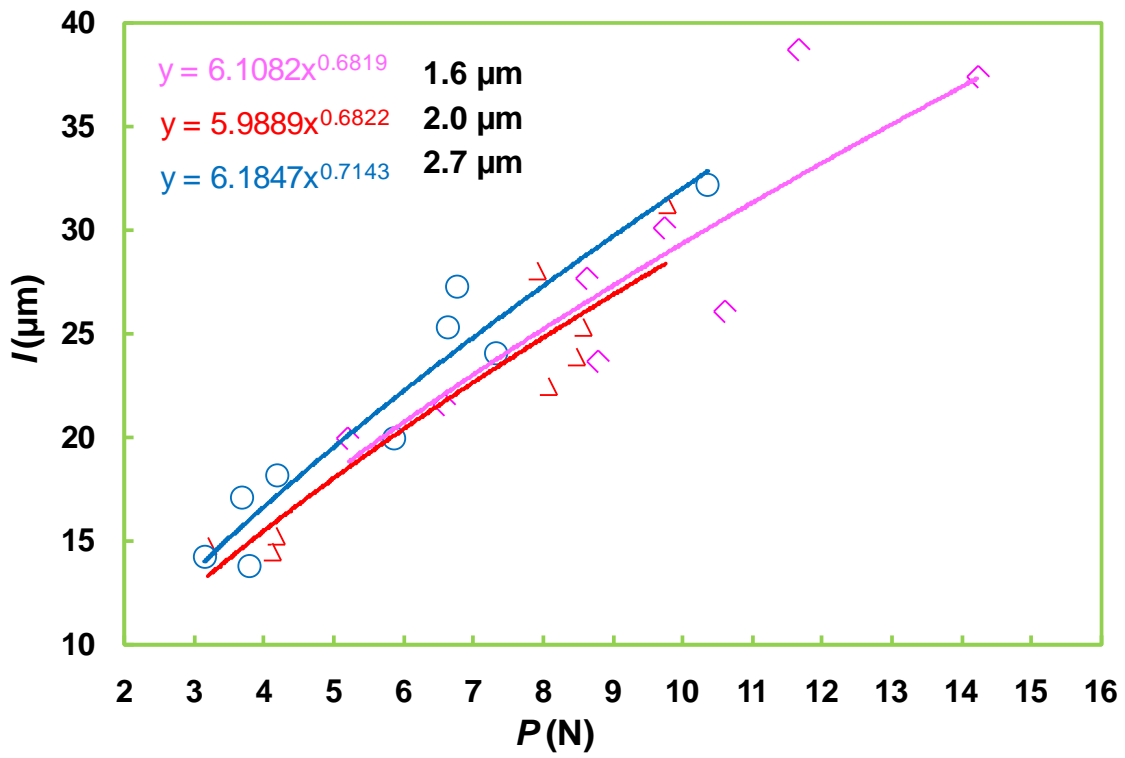


Figure A-2. Variation of I vs. P in B_4C ceramics for dynamic indentations.

LIST OF REFERENCES

- ¹M. J. Normandia, J. C. Lasalvia, W. A. Gooch, J. W. McCauley, and A. M. Rajendran, "Protecting the Future Force: Ceramics Research Leads to Improved Armor Performance," *AMPTIAC Quart.*, **8** [4] 21-7 (2004).
- ²W. G. Fahrenholtz, G. E. Hilmas, I. G. Talmy, and J. A. Zaykoski, "Refractory Diborides of Zirconium and Hafnium," *J. Am. Ceram. Soc.*, **90** [5] 1347-1364 (2007).
- ³W. D. Kingery, H. K. Bowen, and D. R. Uhlmann, *Introduction to Ceramics*, Wiley, New York, 1976.
- ⁴M. W. Barsoum, *Fundamentals of Ceramics*, McGraw Hill, New York, 1997.
- ⁵M. N. Rahaman, *Ceramic Processing and Sintering*, M. Dekker, New York, 2003.
- ⁶B. R. Klotz, K. C. Cho, and R. J. Dowding, "Sintering Aids in the Consolidation of Boron Carbide (B_4C) by the Plasma Pressure Compaction (P^2C) Method," *Mater. Manuf. Process*, **19**, 631-639 (2004).
- ⁷D. P. II. Harvey, R. Kalyanaraman, and T. S. Sudarshan, "Consolidation and Mechanical Behaviour of Nanocrystalline Iron Powder," *Mater. Sci. Tech.*, **18**, 959-63 (2002).
- ⁸T. S. Srivatsan, R. Woods, M. Petraroli, and T. S. Sudarshan, "An Investigation of the Influence of Powder Particle Size on Microstructure and Hardness of Bulk Samples of Tungsten Carbide," *Powder Tech.*, **122** [1] 54-60 (2002).
- ⁹B. G. Ravi, O. A. Omotoye, T. S. Srivatsan, M. Petraroli, and T. S. Sudarshan, "The Microstructure and Hardness of Silicon Carbide Synthesized by Plasma Pressure Compaction," *J. of Alloys Compd.*, **299** [1] 292-6 (2000).
- ¹⁰Thevenot, "Boron Carbide-A Compressive Review," *J. Eur. Ceram. Soc.*, **6**, 205-225 (1990).
- ¹¹H. W. Kim, Y. H. Koh, and H. E. Kim, "Densification and Mechanical Properties of B_4C with Al_2O_3 as a Sintering Aid," *J. Am. Ceram. Soc.*, **83** [11] 2863-2865 (2000).
- ¹²K. A. Schwetz, L. S. Sigl, and L. Pfau, "Mechanical Properties of Injection Molded B_4C -C Ceramics," *J. Solid State Chem.*, **133**, 68-76 (1997).
- ¹³L. S. Sigl, "Processing and Mechanical Properties of Boron Carbide Sintered with TiC," *J. Eur. Ceram. Soc.*, **18**, 1521-1529 (1998).
- ¹⁴Z. Zahariev and D. Radev, "Properties of Polycrystalline Boron Carbide Sintered in the Presence of W_2B_5 without Pressing," *J. Mat. Sci. Lett.*, **7** [7] 695-696 (1988).

- ¹⁵V. Skorokhod JR, M. D. Vlajic, and V. D. Krstic, "Mechanical Properties of Pressureless Sintered Boron Carbide Containing TiB₂ Phase," *J. Mat. Sci. Lett.*, **15** [15] 1337-1339 (1996).
- ¹⁶H. Lee and R. F. Speyer, "Hardness and Fracture Toughness of Pressureless-Sintered Boron Carbide (B₄C)," *J. Am. Ceram. Soc.*, **85** [5] 1291-1293 (2002).
- ¹⁷Kaufmann, D. Cronin, M. Worswick, G. Pageau, and A. Beth, "Influence of Material Properties on the Ballistic Performance of Ceramics for Personal Body Armor," *Shock and Vibration*, **10**, 51-58 (2003).
- ¹⁸M. Chen, J. W. McCauley, and K. J. Hemker, "Shock-induced Localized Amorphization in Boron Carbide," *Science*, **299** [5612] 1563-1566 (2003).
- ¹⁹K. A. Iyer, "Relationships Between Multiaxial Stress States and Internal Fracture Patterns in Sphere-Impacted Silicon Carbide," *Int. J. Frac.*, **146** [1-2] 1-18 (2007).
- ²⁰M. J. Normandia, "Impact Response and Analysis of Several Silicon Carbides," *Int. J. Appl. Ceram. Technol.*, **1** [3] 226-234 (2004).
- ²¹T. J. Holmquist and G. R. Johnson, "Response of Silicon Carbide to High Velocity Impact," *J. Appl. Phys.*, **91** [9] 5858-5866 (2002).
- ²²B. R. Lawn and A. G. Evans, "Elastic-Plastic Indentation Damage in Ceramics: the Median/ Radial Crack System," *J. Am. Ceram. Soc.*, **63** [9-10] 574-581 (1980).
- ²³D. B. Marshall, B. R. Lawn and A. G. Evans, "Elastic-Plastic Indentation Damage in Ceramics: the Lateral Crack System," *J. Am. Ceram. Soc.*, **65** [11] 561-566 (1982).
- ²⁴S. S. Chiang, D. B. Marshall and A. G. Evans, "The Response of Solids to Elastic/Plastic Indentation: (a) Stresses and Residual Stresses and (b) Fracture Initiation," *J. Appl. Phys.*, **53**, 298-317 (1982).
- ²⁵R. F. Cook and G. M. Pharr, "Direct Observation and Analysis of Indentation Cracking in Glasses and Ceramics," *J. Am. Ceram. Soc.*, **73** [4] 787-817 (1990).
- ²⁶J. B. Quinn and G. D. Quinn, "Indentation Brittleness of Ceramics: A Fresh Approach," *J. Mater. Sci.*, **32**, 4331-4346 (1997).
- ²⁷G. Subhash, "Dynamic Indentation Testing," *ASM Handbook on Mechanical Testing and Evaluation*, **8**, 519-529 (2000).
- ²⁸R. J. Anton and G. Subhash, "Dynamic Vickers Indentation of Brittle Materials," *Wear*, **239**, 27-35 (2000).
- ²⁹M. M. Opeka, I. G. Talmy, and J. A. Zaykoski, "Oxidation-based Materials Selection for 2000°C + Hypersonic Aerosurfaces: Theoretical Considerations and Historical Experience," *J. Mater. Sci.*, **39**, 5887-5904 (2004).

- ³⁰D. M. Van Wie, D. G. Drewry JR., D. E. King, and C. M. Hudson, "The Hypersonic Environment: Required Operating Conditions and Design Challenges," *J. Mater. Sci.*, **39**, 5915-5924 (2004).
- ³¹T. A. Jackson, D. R. Eklund, and A. J. Fink, "High Speed Propulsion: Performance Advantage of Advanced Materials," *J. Mater. Sci.*, **39**, 5905-5913 (2004).
- ³²R. Telle, L. S. Sigl, and K. Takagi, "*Boride-Based Hard Materials*," 802–945, Handbook of Ceramic Hard Materials, Edited by R. Riedel. Wiley-VCH, Weinheim, Germany, 2000.
- ³³NSF-AFOSR Joint Workshop on "Future Ultra-High Temperature Materials," Draft Workshop Report, National Science Foundation, April 12 (2004).
- ³⁴R. Loehman, E. Corral, H. P. Dumm, P. Kotula, and R. Tandon, "Ultra-high temperature ceramics for hypersonic vehicle applications," Sandia Report, Sandia national Laboratories (SAND 2006-2925).
- ³⁵G. Subhash, "The Constitutive Behavior of h.c.p. Refractory Metals as a Function of Strain Rate Under Uniaxial Compression," *JOM*, **47** [5] 55-58 (1995).
- ³⁶B. J. Koeppel and G. Subhash, "Influence of Cold Rolling and Strain Rate on Plastic Response of Powder Metallurgy and Chemical Vapor Deposition Rhenium," *Metall. Mater. Transac. A*, **30** [10] 2641-2648 (1999).
- ³⁷J. Han, P. Hu, X. Zhang, and S. Meng, "Oxidation Behavior of Zirconium Diboride-Silicon Carbide at 1800°C," *Scripta Mater.*, **57**, 825-828 (2007).
- ³⁸A. Rezaie, W. G. Fahrenholtz, and G. E. Hilmas, "Evolution of Structure During The Oxidation of Zirconium Diboride-Silicon Carbide in Air up to 1500°C," *J. Eur. Ceram. Soc.*, **27**, 2495-2501 (2007).
- ³⁹W. G. Fahrenholtz, "Thermodynamic Analysis of ZrB₂-SiC Oxidation: Formation of a SiC-Depleted Region," *J. Am. Ceram. Soc.*, **90** [1] 143-148 (2007).
- ⁴⁰A. Rezaie, W. G. Fahrenholtz, and G. E. Hilmas, "Oxidation of Zirconium Diboride-Silicon Carbide at 1500°C at a Low Partial Pressure of Oxygen," *J. Am. Ceram. Soc.*, **89** [10] 3240-3245 (2006).
- ⁴¹T. A. Parthasarathy, R. A. Rapp, M. Opeka, and R. J. Kerans, "A Model for the Oxidation of ZrB₂, HfB₂ and TiB₂," *Acta Mater.*, **55**, 5999-6010 (2007).
- ⁴²A. L. Chamberlain, W. G. Fahrenholtz, and G. E. Hilmas, "Pressureless Sintering of Zirconium Diboride," *J. Am. Ceram. Soc.*, **89** [2] 450-456 (2006).
- ⁴³S. C. Zhang, G. E. Hilmas, and W. G. Fahrenholtz, "Pressureless Densification of Zirconium Diboride with Boron Carbide Additions," *J. Am. Ceram. Soc.*, **89** [5] 1544-1550 (2006).

- ⁴⁴ B. Cech, P. Olivierus, and J. Sejbal, "Sintering of Zirconium Diboride with Activating Additions," *Powder Metall.*, **8** [15] 142-151 (1965).
- ⁴⁵ D. Sciti, M. Brach, and A. Bellosi, "Oxidation Behavior of a Pressureless Sintered ZrB₂-MoSi₂ Ceramic Composite," *J. Mater. Res.*, **20** [4] 922-930 (2005).
- ⁴⁶ A. Rezaie, W. G. Fahrenholtz, and G. E. Hilmas, "Effect of Hot Pressing Time and Temperature on the Microstructure and Mechanical Properties of ZrB₂-SiC," *J. Mater. Sci.*, **42**, 2735-2744 (2007).
- ⁴⁷ F. Monteverde, "Beneficial Effects of an Ultra-Fine α -SiC Incorporation on the Sinterability and Mechanical Properties of ZrB₂," *Appl. Phys. A*, **82**, 329-337 (2006).
- ⁴⁸ H. Wang, C. A. Wang, X. Yao, and D. Fang, "Processing and Mechanical Properties of Zirconium Diboride-Based Ceramics Prepared by Spark Plasma Sintering," *J. Am. Ceram. Soc.*, **90** [7] 1992-1997 (2007).
- ⁴⁹ R. Telle, L. S. Sigl, and K. Takagi, "*Handbook of Ceramic Hard Materials*," Edited by R. Riedel. Wiley-VCH, Weinheim, Germany, 802-945, 2000.
- ⁵⁰ A. L. Chamberlain, W. G. Fahrenholtz, G. E. Hilmas, and D. T. Ellerby, "High Strength ZrB₂-based Ceramics," *J. Am. Ceram. Soc.*, **87** [6] 170-172 (2004).
- ⁵¹ D. E. Wiley, W. R. Manning, and O. Hunter, "Elastic Properties of Polycrystalline TiB₂, ZrB₂ and HfB₂ from Room Temperature to 1300° K," *J. Less-Common Metals*, **18**, 149-57 (1969).
- ⁵² J. J. Melendez-Martinez, A. Dominguez-Rodriguez, F. Monteverde, C. Melandri, and G. de Portu G de, "Characterisation and High Temperature Mechanical Properties of Zirconium Boride-Based Materials," *J. Eur. Ceram. Soc.*, **22**, 2543-2549 (2002).
- ⁵³ S. Zhu, W. G. Fahrenholtz, and G. E. Hilmas, "Influence of Silicon Carbide Particle Size on the Microstructure and Mechanical Properties of Zirconium Diboride-Silicon Carbide Ceramics," *J. Euro. Ceram. Soc.*, **27** [4] 2077-2083 (2007).
- ⁵⁴ A. Chamberlain, W. Fahrenholtz, G. Hilmas, and D. Ellerby, "Oxidation of ZrB₂-SiC Ceramics under Atmospheric and Reentry Conditions," *Refract. Appl. Trans.*, **1** [2] 1-8 (2005).
- ⁵⁵ R. Angers and M. Beauvy, "Hot-Pressing of Boron Carbide," *Ceram. Int.*, **10** [2] 49-55 (1983)
- ⁵⁶ R. Telle and G. Petzow, "Mechanisms in the Liquid-Phase Sintering of Boron Carbide with Silicon Based Melts", *Mater. Sci. Monogr.*, **38A**, 961-973 (1987).
- ⁵⁷ H. T. Larker, L. Hermansson, and J. Adlerborn, "Hot Isostatic Pressing and Its Applicability to Silicon Carbide and Boron Carbide," *Mater. Sci. Monogr.*, **38A**, 795-803 (1987).

- ⁵⁸S. L. Dole, S. Prochazka, and R. H. Doremus, "Microstructural Coarsening During Sintering of Boron Carbide," *J. Am. Ceram. Soc.*, **72** [6] 958-966 (1989).
- ⁵⁹H. Lee and R. F. Speyer, "Pressureless Sintering of Boron Carbide," *J. Am. Ceram. Soc.*, **86** [9] 1468-1473 (2003).
- ⁶⁰H. Lee, R. F. Speyer, and W. S. Hackenberger, "Sintering of Boron Carbide Heat-Treated with Hydrogen," *J. Am. Ceram. Soc.*, **85** [8] 2131-2133 (1989).
- ⁶¹J. D. Katz, R. D. Blake, J. J. Petrovic, and H. Sheinberg, "Microwave Sintering of Boron Carbide," *Met. Powd. Rep.*, **43**, 835-837 (1988).
- ⁶²O. Kida and Y. Segawa. U.S. Patent 4,636,481, January 13, 1987.
- ⁶³O. Kida and Y. Segawa. U.S. Patent 4,678,759, July 7, 1987.
- ⁶⁴D. Kalish, E. V. Clougherty, and K. Kreder, "Strength, Fracture Mode, and Thermal Stress Resistance of HfB₂ and ZrB₂," *J. Am. Ceram. Soc.*, **52** [1] 30-6 (1969).
- ⁶⁵R. A. Andrievskii, L. A. Korolev, V. V. Klimenko, A. G. Lanin, I. I. Spivak, and I. L. Taubin, "Effect of Zirconium Carbide and Carbon Additions on Some Physicomechanical Properties of Zirconium Diboride," *Powder Metall. Metal Ceram.*, **19** [2] 93-4 (1980).
- ⁶⁶D. Kalish and E. V. Clougherty, "Densification Mechanisms in High-Pressure Hot-Pressing of HfB₂," *J. Am. Ceram. Soc.*, **52** [1] 26-30 (1969).
- ⁶⁷R. A. Cutler, "Engineering Properties of Borides," 787-803, *Ceramics and Glasses: Engineered Materials Handbook*, **4**, Edited by S. J. Schneider Jr., ASM International, Materials Park, Ohio, 1991.
- ⁶⁸A. L. Chamberlain, W. G. Fahrenholtz, and G. E. Hilmas, "Reactive Hot Pressing of Zirconium Diboride," *J. Eur. Ceram. Soc.*, In press (2009).
- ⁶⁹X.-J. Zhou, G.-J. Zhang, Y.-G. Li, Y.-M. Kan, and P.-L. Wang, "Hot Pressed ZrB₂-SiC-C Ultra High Temperature Ceramics with Polycarbosilane as a Precursor," *Mater. Lett.*, **61**, 960-963 (2007).
- ⁷⁰G.-J. Zhang, Z.-Y. Deng, N. Kondo, J.-F. Yang, and T. Ohji, "Reactive Hot Pressing of ZrB₂-SiC Composites," *J. Am. Ceram. Soc.*, **83** [9] 2330-32 (2000).
- ⁷¹D. Ghosh, G. Subhash, T. S. Sudarshan, R. Radhakrishnan, and X-L Gao, "Dynamic Indentation Response of Fine-Grained Boron Carbide," *J. Am. Ceram. Soc.*, **90** [6] 1850-1857 (2007).
- ⁷²D. Ghosh, G. Subhash, R. Radhakrishnan, and T. S. Sudarshan, "Scratch-induced Microplasticity and Microcracking in Zirconium Diboride-Silicon Carbide Composite," *Acta Mater.*, **56**, 3011-3022 (2008).

- ⁷³C. E. Inglis, "Stresses in a Plate Due to the Presence of Cracks and sharp corners," *Trans. Inst. Nav. Architects* (London), **55**, 219-241 (1913).
- ⁷⁴A. A. Griffith, "The Phenomena of Rupture and Flow in Solids," *Philos. Trans. R. Soc. London*, **221**, 163-198 (1920).
- ⁷⁵G. R. Irwin, *Fracture Dynamics: In Fracturing of Metals*, American Society of Metals, Cleveland, 1948.
- ⁷⁶E. Orowan, *Fracture Strength of Solids*, In Report on Progress in Physics, Physical Society of London, London, **12**, 185-232 (1949).
- ⁷⁷F. C. Frank and B. R. Lawn, *On the Theory of Hertzian fracture*, Proc. Roy. Soc. Lond., **A299**: 291 (1967).
- ⁷⁸B. R. Lawn, *Fracture of Brittle Solids*, Cambridge University Press, Cambridge, 1995.
- ⁷⁹G. D. Quinn and R. C. Bradt, "On the Vickers Indentation Fracture Toughness Test," *J. Am. Ceram. Soc.*, **90** [3] 673-680 (2007).
- ⁸⁰D. Casellas, J. Caro, S. Molas, J. M. Prado and I. Valls, "Fracture Toughness of Carbides in Tool Steels Evaluated by Nanoindentation," *Acta Mater.*, **55**, 4277-4286 (2007).
- ⁸¹H. Hertz, "On the Contact of Elastic Solids" (in Ger.) *Zeitschrift für die Reine und Angewandte Mathematik*, **92**, 156-171 (1881). English translation in Miscellaneous Papers (translated by D.E. Jones and G. A. Schott); pp. 146-62. Macmillan, London, UK, 1896.
- ⁸²M. A. Meyers, *Dynamic Behavior of Materials*, John Wiley & Sons, Inc., New York, 1994.
- ⁸³J. Lankford, "Mechanisms Responsible for Strain-Rate Dependent Compressive Strength in Ceramic Materials," *J. Am. Ceram. Soc.*, **64**, 33-34 (1981).
- ⁸⁴G. Ravichandran and G. Subhash, "A Micro Mechanical Model for High Strain Rate Behavior of Ceramics," *Int. J. of Solids and Struc.*, **32**, 2627-2650 (1995).
- ⁸⁵G. Subhash and G. Ravichandran, "Mechanical Behavior of Hot-Pressed Aluminum Nitride Under Uniaxial Compression," *J. Mater. Sci.*, **33**, 1933-1939 (1997).
- ⁸⁶H. Wang and K. T. Ramesh, "Dynamic Strength and Fragmentation of Hot-Pressed Silicon Carbide Under Uniaxial Compression," *Acta Mater.*, **52**, 355-367 (2003).
- ⁸⁷G. Ravichandran and G. Subhash, "Critical Appraisal of Limiting Strain Rates for Compression Testing of Ceramics in a Split Hopkinson Pressure Bar," *J. Am. Ceram. Soc.*, **77**, 263-267 (1994).

- ⁸⁸W. Chen and G. Ravichandran, "Static and Dynamic Compressive Behavior of Aluminum Nitride Under Moderate Confinement," *J. Am. Ceram.Soc.*, **79**, 579-584 (1996).
- ⁸⁹W. Chen and G. Ravichandran, "Failure Mode Transition in Ceramics Under Dynamic Multiaxial Compression," *Int. J. Fract.*, **101**, 141-159 (2000).
- ⁹⁰J. Lankford, W. W. Predebon, J. M. Staehler, G. Subhash, B. J. Pletka C. E. Anderson, "The Role of Plasticity as Limiting Factor in the Compressive Failure of High Strength Ceramics," *Mech. Mater.*, **29**, 205-218 (1998).
- ⁹¹S. Suresh, T. Nakamura, Y. Yeshurun, K. H. Yang and J. Duffy, "Tensile Fracture Toughness of Ceramic Materials: Effects of Dynamic Loading and Elevated Temperatures," *J. Am. Ceram. Soc.*, **73**, 2457-2480 (1990).
- ⁹²K. H. Yang and A. S. Kobayashi, "A Hybrid Procedure for Dynamic Characterization of Ceramics at Elevated Temperatures," In *Proc. Conf. Hostile Environments and High Temperature Measurements, SEM.*, 41-44 (1989).
- ⁹³T. Weerasooriya, P. Moy, D. Casem, M. Cheng and W. Chen, "A Four-Point Bend Technique to Determine Dynamic Fracture Toughness of Ceramics," *J. Am. Ceram. Soc.*, **89** [3] 990-995 (2006).
- ⁹⁴W. Böhme and J. F. Kalthoff, "The Behavior of Notched Bend Specimens in Impact Testing," *Int. J. Fract.*, **20**, R139-43 (1982).
- ⁹⁵D. Rittel, H. Mairge and H. D. Bui, "A New Method for Dynamic Fracture Toughness Testing," *Scr. Metall. Material.*, **26** [10] 1593-8 (1992).
- ⁹⁶C. Bacon, J. Faïrm and J. L. Lataillade, "Dynamic Fracture Toughness Determined from Load-Point Displacement," *Exp. Mech.*, **34** [3] 217-23 (1994).
- ⁹⁷W. N. Sharpe and W. Böhme, "Dynamic Fracture Toughness Measurements on Small Charpy Specimens—A Preliminary Study," *J. Test. Eval.*, **22** [1] 14-9 (1994).
- ⁹⁸C. E. Anderson Jr., C. H. Popelar, A. Nagy and J. D. Walker, "A Novel Method for Determining Dynamic Fracture Toughness," 505-508, *Shock Compression of Condensed Matter—1999*, Edited by M. D. Furnish, L. C. Chhabidas, and R. S. Hixson. American Institute of Physics, College Park, MD, 2000.
- ⁹⁹G. Weisbrod and D. Rittel, "A Method for Dynamic Fracture Toughness Determination Using Short Beams," *Int. J. Fract.*, **104** [1] 89-103 (2000).
- ¹⁰⁰C. F. Martins and V. Prakash, "Dynamic Fracture Characteristics of LMDPE Utilizing a Modified Split Hopkinson Bar," *Proceedings of 2002 Society of Experimental Mechanics Annual Conference*, Milwaukee, WI, 2002.

- ¹⁰¹J. Lankford Jr., "The Role of Dynamic Material Properties in the Performance of Ceramic Armor," *Int. J. Appl. Ceram. Tech.*, **1** [3] 205-10 (2004).
- ¹⁰²J.C. LaSalvia, M.J. Normandia, H.T. Miller and D.E. MacKenzie, "Sphere Impact Induced Damage in Ceramics: I. Armor-Grade SiC and TiB₂," *Advances in Ceramic Armor*, edited by J. J. Swab. *Proceedings of the 29th International Conference on Advanced Ceramics and Composites*, Cocoa Beach, Florida, (2005).
- ¹⁰³C. Roberson and P. J. Hazell, "Resistance of Silicon Carbide to Penetration by a Tungsten Carbide-Cored Projectile," in *Ceramic Armor and Armor Systems*, ed. E. Medvedovski, *Ceramics Transactions*, **151**, 165-174 (2003).
- ¹⁰⁴I. M. Pickup, A. K. Barker, R. Chenari, B. J. James, V. Hohler, K. Weber, and R. Tham, "Aspects of Geometry Affecting the Ballistic Performance of Ceramic Targets," *Ceramic Armour Materials by Design*, Edited by J. W. McCauley, A. Crowson, W. A. Gooch, Jr., A. M. Rajendran, S. J. Bless, K. V. Logan, M. Normandia, S. Wax, *Ceramic Transactions*, **134**, 643-650, 2002.
- ¹⁰⁵D. L. Orphal, C. E. Anderson, Jr., D. W. Tempelton, Th. Behner, V. Hohler and S. Chocron, "Using Long Rod Penetration to Detect the Effect of Failure Kinetics in Ceramics," *Proc. 21st. Int. Symp. Ballistics*, **2**, 744-751 (2004).
- ¹⁰⁶A. M. Rajendran, "Modeling the Impact Behavior of a Ceramic under Multiaxial Loading," *Int. J. Impact Eng.*, **15**, 749-768 (1994).
- ¹⁰⁷J. C. LaSalvia, E. J. Horwath, E. J. Rapacki, C. J. Shih and M. A. Meyers, "Microstructural and Micromechanical Aspects of Ceramic/Long-Rod Projectiles Interactions: Dwell/Penetration Transitions," In *Fundamental Issues and Applications of Shock-Wave and High-Strain-Rate Phenomena*, pp.437-446, edited by K. P. Staudhammer, L. E. Murr and M. A. Meyers, Elsevier Science, New York, 2001.
- ¹⁰⁸T. J. Holmquist and G. R. Johnson, "A Detailed Computational Analysis of Interface Defeat, Dwell and Penetration for a Variety of Ceramic Targets," *Proc. 20th. Int. Symp. Ballistics*, **2**, 746-753 (2002).
- ¹⁰⁹T. J. Holmquist and G. R. Johnson, "Modelling Projectile Impact onto Prestressed Ceramic Targets," *J. Phys. IV, France*, **110**, 597-602 (2003).
- ¹¹⁰T. J. Holmquist and G. R. Johnson, "Modelling Pre-Stressed Ceramic and its Effect on Ballistic Performance," *Int. J. Impact Eng.*, **31** [2], 113-127 (2005).
- ¹¹¹R. Renström, P. Lundberg and B. Lundberg, "Stationary Contact between a Cylindrical Metallic Projectile and A Flat Target Under Conditions of Dwell," *Int. J. Impact Eng.*, **30**, 1265-1282 (2004).
- ¹¹²P. Lundberg, R. Renstrom and L. Holmberg, "An Experimental Investigation of Interface Defeat at Extended Interaction Time," *19th International Symposium of Ballistics*, May, Interlaken Switzerland (2001).

- ¹¹³D. A. Shockey, A. H. Marchand, S. R. Skagg, G. E. Cort, M. W. Burkett and R. Parker, "Failure Phenomenological of Confined Ceramic Targets and Impacting Rods," *Int. J. Impact Eng.*, **9** [3], 263-75 (1990).
- ¹¹⁴D. Sherman, "Impact Failure Mechanisms in Alumina Tiles on Finite Thickness Support and the Effect of Confinement," *Int. J. Impact Eng.*, **24**, 312-328 (2000).
- ¹¹⁵T. J. Holmquist, A. M. Rajendran, D. W. Templeton and K. D. Bishnoi, "A Ceramic Armor Material Database," *TARDEC Technical Report #13754* (1999).
- ¹¹⁶G. E. Hauver, E. J. Rapacki, P. H. Netherwood, R. F. Benck, *ARL-TR-3590*, September (2005).
- ¹¹⁷G. E. Hauver, P. H. Netherwood, R. F. Benck and L. J. Kecskes, "Ballistic Performance of Ceramic Targets" *Proceedings of 13th Army Symposium on Solid Mechanics*, Eds. S. C. Chou, F. D. Bartlett Jr., T. W. Wright and K. Iyer, 23-34, 1993.
- ¹¹⁸J. C. LaSalvia, "A Physically Based Model for the Effect of Microstructure and Mechanical Properties on Ballistic Performance," *26th Annual Inter. Conf. Adv. Ceram. & Comp.*, Cocoa Beach, January 13-18, Florida, (2002).
- ¹¹⁹J. C. Lasalvia, E. J. Horwath, E. J. Rapacki, C. J. Shih and M. A. Meyers, "Microstructural and Micromechanical Aspects of Ceramic/Long-Rod Projectile Interactions: Well/Penetration Transition," *Explomet 2000*, Albuquerque, New Mexico June 18-22 (2000).
- ¹²⁰B. J. Koeppel and G. Subhash, "An Experimental Technique to Investigate the Dynamic Indentation Hardness of Materials," *Exp. Tech., USA*, **21** [3], 16-18 (1997).
- ¹²¹B. J. Koeppel and G. Subhash, "Characteristics of Residual Plastic Zone Under Static and Dynamic Indentations" *Wear*, **224**, 56-67 (1999).
- ¹²²G. Subhash, B. J. Koeppel and A. Chandra, "Dynamic Indentation Hardness and Rate Sensitivity in Metals," *J. Eng. Mater. Technol.*, **121**, 1-7 (1999).
- ¹²³S. Nemat-Nasser, J. B. Isaacs, and J. E. Starrett, "Hopkinson Techniques for Dynamic Recovery Experiments," *Proc. R. Soc. (London) A*, **435**, 371-391 (1991).
- ¹²⁴H. W. Zhang, S. Maiti, and G. Subhash, "Evolution of Shear Bands in Bulk Metallic Glasses under Dynamic Loading," *J. Mech. Phys. Solids*, **56** [6] 2171-2187 (2008).
- ¹²⁵G. Subhash and H. W. Zhang, "Dynamic Indentation Response of ZrHf-Based Bulk Metallic Glasses," *J. Mater. Res.*, **22** [2] 478-485 (2007).
- ¹²⁶D. Tabor, *Hardness of Metals*, Clarendon Press, Oxford, 1951.

- ¹²⁷H. Li, G. Subhash, X.-L. Gao, L. J. Kecskes, and R. J. Dowding, "Negative Strain Rate Sensitivity and Compositional Dependence of Fracture Strength in Zr/Hf Based Bulk Metallic Glasses," *Scripta Mater.*, **49** [11] 1087-1092 (2003).
- ¹²⁸C. B. Ponton and R. D. Rawlings, "Vickers Indentation Fracture Toughness Test Part 1 Review of Literature and Formulation of standardized Indentation Toughness equations." *Mater. Sci. and Tech.*, **5**, 865-872 (1989).
- ¹²⁹R. W. Rice, "Hardness-Grain-Size Relations in Ceramics," *J. Am. Ceram. Soc.*, **77** [10] 2539-53 (1994).
- ¹³⁰R. W. Rice, "Mechanical Properties of Ceramics and Composites: Grain and Particle Effects," *CRC* 1st edition May 15 (2000).
- ¹³¹D. Ge, V. Domnich, A. Juliano, E. A. Stach, and Y. Gogotsi, "Structural Damage in Boron Carbide under Contact Loading," *Acta. Mater.*, **52**, 3921-3927 (2004).
- ¹³²X. Q. Yan, W. J. Li, T. Goto, and M.W. Chen, "Raman Spectroscopy of Pressure-Induced Amorphous Boron Carbide," *Appl. Phys. Lett.*, **88**, 131905-1 - 131905-1 (2006).
- ¹³³G. Fanchini, J. W. McCauley, and M. Chhowalla, "Behavior of Disordered Boron Carbide under Stress," *Phys. Rev. Lett.*, **97**, 035502-1- 035502-4 (2006).
- ¹³⁴R. Lazzarari, N. Vast, J. M. Besson, S. Baroni and A. D. Corso, "Atomic Structure and Vibrational Properties of Icosahedral B₄C Boron Carbide," *Phys. Rev. Lett.*, **83**, 3230-3233 (1999).
- ¹³⁵I. Jimenez, D. G. J. Sutherland, T. v. Buuren, J. A. Carlisle, L. J. Terminello, and F. J. Himpsel, "Photoemission and X-ray-absorption Study of Boron Carbide and its Surface Thermal Stability," *Phys. Rev. B.*, **57**, 13167-131174 (1998).
- ¹³⁶E. Smith and G. Dent, *Modern Raman Spectroscopy – A Practical Approach*, John Wiley & Sons, Ltd., Clarendon Press, England, 2005.
- ¹³⁷E. G. Brame Jr. and J. Grasselli, *Infrared and Raman Spectroscopy (Part A)*, Marcel Dekker, Inc, New York, 1976.
- ¹³⁸<http://en.wikipedia.org/wiki/Photoluminescence>.
- ¹³⁹Y. K. Yap, S. Kida, T. Aoyama, Y. Mori and T. Sasaki, "Influence of Negative dc Bias Voltage on Structural Transformation of Carbon Nitride at 600 °C," *Appl. Phys. Lett.*, **73**, 915-917 (1998).
- ¹⁴⁰Y. K. Yap, M. Yoshimura, Y. Mori and T. Sasaki, "Hybridized Boron–Carbon Nitride Fibrous Nanostructures on Ni Substrates," *Appl. Phys. Lett.*, **80**, 2559-2561 (2002).

- ¹⁴¹M. Ramsteiner, and J. Wanger, "Resonant Raman Scattering of Hydrogenated Amorphous Carbon: Evidence for pi-Bonded Carbon Clusters," *Appl. Phys. Lett.*, **51**, 1355 (1987).
- ¹⁴²A. C. Ferrari and J. Robertson, "Resonant Raman Spectroscopy of Disordered, Amorphous, and Diamondlike Carbon," *Phys. Rev. B*, **64**, 075414-1- 075414-13 (2001).
- ¹⁴³A. C. Ferrari and J. Robertson, "Interpretation of Raman Spectra of Disordered and Amorphous Carbon," *Phys. Rev. B*, **61**, 14095 (2000).
- ¹⁴⁴H. Werheit, "On Excitons and Other Gap States in Boron Carbide," *J. Phys. Conds. Mater.*, **18**, 10655-10662 (2006).
- ¹⁴⁵J. Xu, J. Mei, X. Huang, W. Li, Z. Li, X. Li, and K. Chen, "The change of Photoluminescence Characteristics of Amorphous Carbon Films due to Hydrogen Dilution," *J. Non-Cryst. Solids.*, **338-340**, 481-485 (2004).
- ¹⁴⁶H. Werheita, T. Aua, R. Schmechela, S. O. Shalamberidzeb, G. I. Kalandadzeb, and A. M. Eristavib, "IR-Active Phonons and Structure Elements of Isotope-Enriched Boron Carbide," *J. Solid State Chem.*, **154**, 79 (1999).
- ¹⁴⁷C. L. Beckel, M. Yousaf, M. Z. Fuka, S. Y. Raja, and N. Lu, "Lattice Vibrations of the Icosahedral Solid α -Boron," *Phys. Rev. B*, **44**, 2535-2553 (1991).
- ¹⁴⁸K. Shirai, S. Emura, and S-i. Gonda, "Infrared Study of Amorphous $B_{1-x}C_x$ films," *J. Appl. Phys.*, **78**, 3392-3400 (1995).
- ¹⁴⁹H. Ikeda, Y. Qi, T. Cagin, K. Samwer, W. L. Johnson, and W. A. Goddard III, "Strain Rate Induced Amorphization in Metallic Nanowires," *Phys. Rev. Letts.*, **82**, 2900-2903 (1999).
- ¹⁵⁰Y. Ahn, T. N. Farris, and S. Chandrasekar, "Sliding Microindentation Fracture of Brittle Materials: Role of Elastic Stress Fields," *Mech. Mater.*, **29** [11] 143-152 (1998).
- ¹⁵¹X. Jing, G. Subhash, and S. Maiti, "A New Analytical Model for Estimation of Scratch Induced Damage in Brittle Solids" *J. Am. Ceram. Soc.*, **90** [3] 885-892 (2007).
- ¹⁵²H. Wang and G. Subhash, "Mechanics of Mixed-mode Ductile Material Removal with a Conical Tool and the Size Dependence of the Specific Energy," *J. Mech. Phys. Solids.*, 2002;50:1269-1296.
- ¹⁵³G. Subhash and R. Bandyo, "A New Scratch Resistance Measure for Structural Ceramics," *J. Am. Ceram. Soc.*, **88**, 918 (2005).

- ¹⁵⁴G. Subhash, M. A. Marszalek, and S. Maiti, "Sensitivity of Scratch Resistance to Grinding-Induced Damage Anisotropy in Silicon Nitride," *J. Am. Ceram. Soc.* **89**, 2528-2536 (2006).
- ¹⁵⁵G. Subhash and M. Klecka, "Ductile to Brittle Transition Depth during Single-grit Scratching on Alumina Ceramics," *J. Am. Ceram. Soc.*, **90**, 3704-3707 (2007).
- ¹⁵⁶H. Wang, G. Subhash, and A. Chandra, "Characteristics of Single-grit Rotating Scratch with a Conical Tool on Pure Titanium," *Wear*, **249**, 566-581 (2001).
- ¹⁵⁷G. Subhash, J. E. Loukus, and S. M. Pandit, "Applications of Data Dependent Systems Approach for Evaluation of Fracture Modes during a Single-grit Scratching," *Mech. Mater.*, **34**, 25-42 (2002).
- ¹⁵⁸H. Wang and G. Subhash, "Mechanics of Mixed-mode Ductile Material Removal with a Conical Tool and the Size Dependence of the Specific Energy," *J. Mech. Phys. Solids*, **50**, 1269-1296 (2002).
- ¹⁵⁹J. S. Haggerty and D.W. Lee, "Plastic Deformation of ZrB₂ Single Crystals," *J. Am. Ceram. Soc.*, **54**, 572-576 (1971).
- ¹⁶⁰D. Ghosh, G. Subhash, and G. R. Bourne, "Inelastic Deformation under Indentation and Scratch Loads in a ZrB₂-SiC Composite," *J. Eur. Ceram. Soc.*, **29**, 3053-3061 (2009).
- ¹⁶¹J. P. Herth and J. Lothe, *Theory of Dislocations*, Krieger Publishing Company, Florida, 1982.
- ¹⁶²M. H Yoo, J. R. Morris, K. M. Ho, and S. R. Agnew, "Nonbasal Deformation Modes of HCP Metals and Alloys: Role of Dislocation Source and Mobility," *Met. and Mat. Trans A*, **33A**, 813-822 (2002).
- ¹⁶³G. Subhash, G. Ravichandran, and B. J. Pletka, "Plastic Deformation of Hafnium under Uniaxial Compression," *Metall. Trans. A*, **28A**, 1479-1487 (1997).
- ¹⁶⁴R. F. Firestone and A. H. Heuer, "Creep Deformation of 0° sapphire," *J. Am. Ceram. Soc.*, **59** [1-2] 24-29 (1976).
- ¹⁶⁵J. D. O Barceinss-sanchez and W. M. Rainforth, "On the Role of Plastic Deformation during the Mild Wear of Alumina," *Acta Mater.*, **46** [18] 6475-6483 (1998).
- ¹⁶⁶S. Rohmfeld, M. Hundhausen, and L. Ley, "Raman Scattering in Polycrystalline 3C-SiC: Influence of Stacking Faults," *Phys. Rev. B*, **88** [15] 9858-9862 (1998).
- ¹⁶⁷K. L. Johnson, *Contact Mechanics*. Cambridge University Press, Cambridge, 1985.
- ¹⁶⁸E. H. Yoffe, "Elastic Stress Fields Caused by Indenting Brittle Materials," *Phil. Mag. A*, **46** [4] 617-628 (1982).

- ¹⁶⁹J. Lankford, W. W. Predebon, J. M. Staehler, G. Subhash, B. J. Pletka, and C. E. Anderson, "The Role of Plasticity as a Limiting Factor in the Compressive Failure of High Strength Ceramics," *Mech. Mater.*, **29**, 205-218 (1998).
- ¹⁷⁰T. L. Johnston, R. S. Stokes, and C. H. Li, "Crack Nucleation in Magnesium Oxide Bicrystals under Compression," *Phil. Mag.*, **7**, 23 (1962).
- ¹⁷¹R. W. Rice, *Mechanical Properties of Ceramics and Composites*. Marcel Dekker Inc., New York, 2000.
- ¹⁷²F. P. Bowden and D. T. Tabor, *Friction and Lubrication of Solids*, Clarendon Press, Oxford, 1950.
- ¹⁷³S. V. Prasad and K. R. Mecklenburg, "Friction Behavior of Ceramic Fiber-reinforced Aluminum Metal-matrix Composites Against a 440C Steel Counterface," *Wear*, **162-164**, 47-56 (1993).
- ¹⁷⁴J.-A. Ruan and B. Bhushan, "Atomic-scale and Microscale Friction Studies of Graphite and Diamond using Friction Force Microscopy," *J. Appl. Phys.*, **76**, 5022-5035 (1994).
- ¹⁷⁵F. Varnik, L. Bocquet, J.-L. Barrat, and L. Berthier, "Shear Localization in a Model Glass," *Phys. Rev. Lett.*, **90**, 095702-1 - 095702-4 (2003).
- ¹⁷⁶K. Li, Y. Shapiro, and J. C. M. Li, "Scratch Test of Soda-lime Glass," *Acta Mater.*, **46**, 5569-5578 (1998).
- ¹⁷⁷R. Smith, D. Mulliah, S. D. Kenny, E. McGee, A. Richter, and M. Gruner, "Stick Slip and Wear on Metal Surfaces," *Wear*, **259**, 459-466 (2005).
- ¹⁷⁸C. Gao, D. Kuhlmann-Wilsdorf, and D. D. Makel, "Fundamentals of Stick-slip," *Wear*, **162-164**, 1139-1149 (1993).
- ¹⁷⁹D. Mulliah, S. D. Kenny, and R. Smith, "Modeling of Stick-slip Phenomena using Molecular Dynamics," *Phys. Rev. B*, **69**, 205407-1 - 205407-8 (2004).
- ¹⁸⁰D. Mulliah, S. D. Kenny, R. Smith, and C. F. Sanz-Navarro, "Molecular Dynamic Simulations of Nanoscratching of Silver (100)," *Nanotechnology*, **15**, 243-249 (2004).
- ¹⁸¹D. Mulliah, S. D. Kenny, E. McGee, R. Smith, A. Richter, and B. Wolf, "Atomistic Modelling of Ploughing Friction in Silver, Iron and Silicon," *Nanotechnology*, **17**, 1807-1818 (2006).
- ¹⁸²E. Anastassakis, A. Pinczuk, E. Burstein, F. H. Pollak, and M. Cardona, "Effect of Static Uniaxial Stress on the Raman Spectrum of Silicon," *Solid State Commun.*, **8**, 133-138 (1970).

- ¹⁸³Y. Kang, Y. Qiu, Z. Lei, and M. Hu, "An Application of Raman Spectroscopy on the Measurement of Residual stress in Porous Silicon," *Optics. Laser Eng.*, **43**, 847-855 (2005).
- ¹⁸⁴N. Orlovskaya, D. Steinmetz, S. Yarmolenko, D. Pai, J. Sankar, and J. Goodenough, "Detection of Temperature- and Stress-induced Modifications of LaCoO₃ by micro-Raman Spectroscopy," *Phys. Rev. B*, **72**, 014122-1 - 014122-7 (2005).
- ¹⁸⁵J. K. Shin, C. S. Lee, K. R. Lee, and K. Y. Eun, "Effect of Residual Stress on the Raman-Spectrum Analysis of Tetrahedral Amorphous Carbon Films," *Appl. Phys. Lett.*, **78**, 631-633 (2001).
- ¹⁸⁶N. Orlovskaya, J. Kuebler, V. Subbotin, and M. Lugovy, "Design of Si₃N₄-based Ceramic Laminates by the Residual Stresses," *J. Mater. Sci.*, **40**, 5443-5450 (2005).
- ¹⁸⁷Y. Gogotsi, G. Zhou, S. S. Ku, and S. Cetinkunt, "Raman Microspectroscopy Analysis of Pressure-induced Metallization in Scratching of Silicon," *Semicond. Sci. Technol.*, **16**, 345-352 (2001).
- ¹⁸⁸I. De Wolf, "Micro-Raman Spectroscopy to Study Local Mechanical Stress in Silicon Integrated Circuits," *Semicond. Sci. Technol.*, **11**, 139-154 (1996).
- ¹⁸⁹J. Chen and I. De Wolf, "Theoretical and Experimental Raman Spectroscopy Study of Mechanical Stress Induced by Electronic Packaging," *IEEE Transac. Compon. Pack. Tech.*, **28**, 484-492 (2005).
- ¹⁹⁰H. Mukaida, H. Okumura, J. H. Lee, H. Diamon, E. Sakuma, S. Misawa, K. Endo, and S. Yoshida, "Raman scattering of SiC: Estimation of the Internal Stress in 3C-SiC on Si," *J. Appl. Phys.*, **62**, 254-256 (1987).
- ¹⁹¹S. Rohmfeld, M. Hundhausen, and L. Ley, "Raman Scattering in Polycrystalline 3C-SiC: Influence of Stacking Faults," *Phys. Rev. B.*, **88**, 9858-9862 (1998).
- ¹⁹²Z. C. Feng, W. J. Choyke, and J. A. Powell, "Raman Determination of Layer Stresses and Strains for Heterostructures and its Application to the Cubic SiC/Si System," *J. Appl. Phys.*, **64**, 6827-6835 (1988).
- ¹⁹³C. M. Su, M. Wuttiga, A. Fekade, and M. Spencer, Elastic and Anelastic Properties of Chemical Vapor Deposited Epitaxial 3C-SiC, *J. Appl. Phys.*, **77**, 5611-5615 (1995).
- ¹⁹⁴D. N. Talwar and J. C. Sherbondy, Thermal Expansion Coefficient of 3C-SiC, *Appl. Phys. Lett.*, **67**, 3301-3303 (1995).
- ¹⁹⁵H. J. Choi and J. G. Lee, Stacking Faults in Silicon Carbide Whiskers, *Ceram. Inter.*, **26** [1] 7-12 (2000).
- ¹⁹⁶C. J. Shih, M. A. Meyers, V. F. Nesterenko, and S. J. Chen, "Damage Evolution in Dynamic Deformation of Silicon Carbide," *Acta Mater.*, **48**, 2399-2420 (2000).

- ¹⁹⁷K. K. Chawla, *Ceramic Matrix Composites*, Kluwer Academic Publishers, Massachusetts.
- ¹⁹⁸F. Cerdeira, C. J. Buchenauer, F. H. Pollak, and M. Cardona, "Stress-Induced Shifts of First-Order Raman Frequencies of Diamond- and Zinc-Blende-Type Semiconductors," *Phys. Rev. B*, **5**, 580-593 (1972).
- ¹⁹⁹J. S. Mitchell, C. A. Zorman, T. Kicher, S. Roy, and M. Mehregany, "Examination of Bulge Test for Determining Residual Stress, Young's Modulus, and Poisson's Ratio of 3C-SiC Thin Films," *J. Aero. Eng.*, **16**, 46-54 (2003).
- ²⁰⁰M. Miura, H. Murata, Y. Shiro, and K. Lishi, Ionicity Scale and Piezoelectricity of Crystals with Zincblende- and Wurtzite-type Structure, *J. Phys. Chem. Solids.*, **42** [10] 931-936 (1981).
- ²⁰¹D. S. Knight and W. B. White, Characterization of Diamond Films by Raman Spectroscopy, *J. Mater. Res.*, **4**, 385-393 (1989).
- ²⁰²J. G. Kim and J. Yu, "Measurement of Residual Stress in Diamond Films Obtained Using Chemical Vapor Deposition," *Jpn. J. Appl. Phys.*, **37**, L890-L893 (1998).
- ²⁰³C. A. Taylor, M. F. Wayne, and W. K. S. Chiu, "Residual Stress Measurement in Thin Carbon Films by Raman Spectroscopy and Nanoindentation," *Thin Solid Films*, **429**, 190-200 (2003).
- ²⁰⁴G. D. Zhan, R. J. Xie, and M. Mitomo, "Effect of beta-to-alpha Phase Transformation on the Microstructural Development and Mechanical Properties of Fine-Grained Silicon Carbide Ceramics," *J. Am. Ceram. Soc.*, **84** [5] 945-950 (2001).
- ²⁰⁵Y. Zhou, K. Hirao, M. Toriyama, Y. Yamauchi, and S. Kanzaki, "Effects of Intergranular Phase Chemistry on the Microstructure and Mechanical Properties of Silicon Carbide Ceramics Densified with Rare-Earth Oxide and Alumina Additions," *J. Am. Ceram. Soc.*, **84** [7] 1642-1644 (2001).
- ²⁰⁶Y. W. Kim, M. Mitomo, H. Emoto, and J. G. Lee, "Effect of Initial alpha-Phase Content on Microstructure and Mechanical Properties of Sintered Silicon Carbide," *J. Am. Ceram. Soc.*, **81** [12] 3136-3140 (1998).
- ²⁰⁷H. D. Espinosa, B. Peng, N. Moldovan, T. A. Friedmann, X. Xiao, D. C. Mancini, O. Auciello, J. Carlisle, C. A. Zorman, and M. Merhegany, "Elasticity, Strength, and Toughness of Single Crystal Silicon Carbide, Ultrananocrystalline Diamond, and Hydrogen-free Tetrahedral Amorphous Carbon," *Appl. Phys. Letts.*, **89**, 073111-1 - 073111-3 (2006).
- ²⁰⁸J. W. III Ager and M. D. Drory, "Quantitative Measurement of Residual Biaxial Stress by Raman Spectroscopy in Diamond Grown on a Ti Alloy by Chemical Vapor Deposition," *Phys. Rev. B*, **48**, 2601-2607 (1993).

- ²⁰⁹E. Anastassakis, A. Cantarero, and M. Cardona, "Piezo-Raman Measurements and Anharmonic Parameters in Silicon and Diamond," *Phys. Rev. B*, **41**, 7529-7535 (1990).
- ²¹⁰R. C. Teixeira, I. Doi, M. B. P. Zakia, J. A. Diniz, and J. W. Swart, "Micro-Raman Stress Characterization of Polycrystalline Silicon Films Grown at High Temperature," *Mater. Sci. Eng. B*, **112** [2-3] 160-164 (2004).
- ²¹¹D. Ghosh, G. Subhash and G. R. Bourne, "Room-temperature Dislocation Activity during Mechanical Deformation of Polycrystalline Ultra High-temperature Ceramics," *Scripta Mater.*, In press (2009).
- ²¹²D. Grabco, B. Pushcash, M. Dyntu and O. Shikimaka, Thermal Evolution of Deformation Zones around Microindentations in Different Types of Crystal, *Phil. Mag. A.*, **82**, 2207-2215 (2002).
- ²¹³L. A. Giannuzzi and F. A. Stevie, *Introduction to Focused Ion Beams: Instrumentation, Theory, Techniques and Practice*, Springer, New York, 2005, pp. 201–212.
- ²¹⁴Y. Xuan, C.-H. Chen, and S. Otani, "High Temperature Microhardness of ZrB₂ Single Crystals," *J. Phys. D: Appl. Phys.*, **35**, L98-L100 (2002).
- ²¹⁵K. Nakano, T. Imura, and S. Takeuchi, "Hardness Anisotropy of Single Crystals of IVa-Diborides," *Jap. J. Appl. Phys.*, **12**, 186-189 (1973).
- ²¹⁶W. D. Kingery, H. K. Bowen, and D. R. Uhlmann, *Introduction to Ceramics*, 2nd ed., John Wiley & Sons, New York.
- ²¹⁷C. C. Wang, S. A. Akbar, W. Chen, and V. D. Patton, Electrical Properties of High-temperature Oxides, Borides, Carbides, and Nitrides, *J. Mater. Sci.*, **30**, 1627-1641 (1995).
- ²¹⁸M. A. Meyers and K. K. Chawla, *Mechanical Behavior of Materials*, Prentice-Hall, Inc, New Jersey.
- ²¹⁹R. G. Munro, Material Properties of Titanium Diboride, *J. Res. Nat. Ins. Std. Tech.*, **105**, 709-720 (2000).
- ²²⁰F. Thevenot, "Boron Carbide - A Comprehensive Review," *J. Eur. Ceram. Soc.*, **6**, 205-225 (1990).
- ²²¹M. W. Barsoum, *Fundamentals of Ceramics*, McGraw-Hill.
- ²²²M. M. R. Howlader, C. Kinoshita, T. Izu, K. Shiiyama, and M. Kutsuwada, "In Situ Measurement of Electrical Conductivity of Alumina under Electron Irradiation in a High Voltage Electron Microscope," *J. Nuclear Mater.*, **239**, 245-252 (1996).

- ²²³G. Subhash, G. Ravichandran, and B. J. Pletka, "Plastic Deformation of Hafnium under Uniaxial Compression," *Metall. Mater. Trans., A*, **28A**, 1479-1487 (1997).
- ²²⁴R.-G. Duan, J.D. Kuntz, J.E. Garay, and A.K. Mukherjee, "Metal-like Electrical Conductivity in Ceramic Nano-composite," *Scripta Mater.*, **50**, 1309-1313 (2004).
- ²²⁵W. D. Callister, *Materials Science and Engineering An Introduction*, 5th edition, John Wiley & Sons, Inc, New York.
- ²²⁶P. Vajeeston, P. Ravindran, C. Ravi, and R. Asokamani, "Electronic Structure, Bonding, and Ground-state Properties of AlB₂-type Transition-metal Diborides," *Phy. Rev. B*, **63**, 045115-1 - 045115-12 (2001).
- ²²⁷X. Zhang, X. Luo, J. Han, J. Li, and W. Han, "Electronic Structure, Elasticity and Hardness of Diborides of Zirconium and Hafnium: First Principles Calculations," *Comp. Mater. Sci.*, **44**, 411-421 (2008).
- ²²⁸J.J. Gilman, "Why Si Is Hard," *Science*, **261**, 1436-1439 (1993).
- ²²⁹J.J. Gilman, "Chemical Theory of Dislocation Mobility," *Mater. Sci. Eng. A*, **409**, 7-12 (2005).
- ²³⁰R. W. Davidge, *Mechanical Behaviour of Ceramics*, Cambridge University Press; 1st Ed., 1979.
- ²³¹A. H. Heuer and L. W. Hobbs, *Science and Technology of Zirconia, Advances in Ceramics*, 3, The American Ceramics Society, Westerville, Ohio, 1981.
- ²³²A. Taylo and D. S. Laidler, "The Formation and Crystal Structure of Silicon Carbide," *British J. App. Phys.*, **1**, 174-181 (1950).
- ²³³S. N. Ruddlesden and P. Popper, "On the Crystal Structure of the Nitrides of Silicon and Germanium," *Acta Cryst.*, **11**, 465-468 (1958).
- ²³⁴D. Ghosh, G. Subhash, C. H. Lee, and Y. K. Yap, "Strain-induced Formation of Carbon and Boron Clusters in Boron Carbide during Dynamic Indentation," *Appl. Phys. Lett.*, **91**, 061910-1 - 061910-3 (2007).
- ²³⁵G. Subhash, S. Maiti, P. H. Geubelle, and D. Ghosh, "Recent Advances in Dynamic Indentation Fracture, Impact Damage and Fragmentation of Ceramics," *J. Am. Ceram. Soc.*, **91** [9] 2777-2791 (2008).
- ²³⁶D. Ghosh, G. Subhash, and N. Orlovskaya, Measurement of Scratch-induced Residual Stress within SiC Grains in ZrB₂-SiC Composite using Micro-Raman spectroscopy," *Acta Mater.*, **56**, 5345-5354 (2008).

BIOGRAPHICAL SKETCH

Dipankar Ghosh was born in Kolkata, West Bengal, India. He completed his high school education in 1996 from Sodepur High School in India. He earned his B.S. in Chemistry in 1999 and B.Tech. in Chemical Technology (with specialization in Ceramic Engineering) in 2002 from the University of Calcutta in India. Then, for higher education, he joined Indian Institute of Technology (IIT), Kharagpur (India) where he received M.Tech. in Materials Science and Engineering in 2004. During this period, apart from learning basics of Materials Science and Advanced Ceramics, he also conducted research on Colloidal processing of dense and porous ceramics.

Upon graduating from IIT, to pursue further higher education, Mr. Ghosh came to United States and started his PhD at Michigan Technological University (MTU), Houghton, in 2004 under the supervision of Prof. Ghatu Subhash. At MTU, he spent few years as a graduate student in Materials Science and Engineering Department and then he joined the University of Florida, Gainesville, in 2007 where he continued his PhD research under the supervision of Prof. Ghatu Subhash in the Department of Mechanical and Aerospace Engineering. Mr. Ghosh successfully completed his PhD dissertation in 2009.

His PhD dissertation has been focused on processing and mechanical characterization of advanced structural ceramics. He conducted research on processing of high-temperature ceramics, and characterized the processed ceramics using several mechanical and spectroscopic techniques to understand the fundamental deformation mechanisms. He has published 10 peer-reviewed papers in prestigious international journals and 4 conference proceedings. Based on his PhD research, he received Second Prize - Best Paper Awards at 32nd International Conference on Advanced

Ceramics & Composites, American Ceramic Society, Daytona Beach, FL (2008). Mr. Ghosh along with five other graduate engineer students from the School of Engineering, UF, were acknowledged in the Fall, 2009 issue of “The Florida Engineer” for their significant contributions in the respective research areas. He also received an “International Student Outstanding Achievement” award at 15th Annual International Student Academic Awards Ceremony at UF in Fall, 2009.